Title

Synthesis and Design Cationic Metal-Organic Frameworks for Perchlorate Remediation and Bactericidal Applications

Permalink

https://escholarship.org/uc/item/4862f6c6

Author

Colinas, Ian Rodrigo

Publication Date

2018

UNIVERSITY CALIFORNIA
SANTA CRUZ

SYNTHESIS AND DESIGN CATIONIC METAL-ORGANIC FRAMEWORKS FOR PERCHLORATE REMEDIATION AND BACTERICIDAL APPLICATIONS

A dissertation submitted in partial satisfaction
of the requirements for the degree of

DOCTOR OF PHILOSOPHY

in

CHEMISTRY

by

Ian R. Colinas

September 2018

The dissertation of Ian R. Colinas
is approved:

Professor Yat Li, Chair

Professor Scott Oliver, Advisor

Professor Shaowei Chen

Lori Kletzer,
Vice Provost and Dean of Graduate Studies

Table of Contents

Chapter 1. Cationic Metal-Organic Frameworks for Applications in Wastewater Treatment by Anion Exchange

Chapter 2. Reversible, Selective Trapping of Perchlorate from Water by a Cationic Metal-Organic Framework

Chapter 3. Anion Exchange Dynamics in the Capture of Perchlorate from Water by a Cationic Ag-based MOF

Chapter 4. Synthesis and characterization of two structurally diverse Zn-based coordination polymers with excellent antibacterial activity

Chapter 5. Conclusions and Future Work

Appendix

List of Figures

List of Tables

Abstract

Synthesis and Design of Cationic Metal-Organic Frameworks for Perchlorate Remediation and Bactericidal Applications

by

Ian R. Colinas

The issue of perchlorate (ClO_4^-) as an emerging pollutant has gained significant attention globally as it has been detected in groundwater, surface water, soils, and crops of many countries including the United States, Japan, China, India, Korea, and Germany. The toxic effects of this anionic pollutant result from the disruption of the thyroid gland, which is blocked and inhibited from iodide uptake due to the slightly larger ionic radii of perchlorate. Such impairment of the thyroid gland can occur upon exposure to parts per billion (ppb) perchlorate levels, and it has been associated with detrimental development effects in fetuses and children. Most perchlorate is manufactured for its use as a primary ingredient in solid rocket propellants in both military and aerospace technology, and its widespread occurrence in the environment has resulted from its improper disposal and high mobility in aqueous environments.

Currently, anion exchange resins are the standard material used for perchlorate remediation. These consist of inexpensive polymeric matrices with limited chemical and thermal stability due to their organic nature. In addition, their

performance is severely affected by their poor selectivity towards perchlorate and lack of recyclability. Therefore, high performance anion exchangers that can efficiently capture perchlorate are sought. Extended inorganic crystalline materials are promising candidates for the replacement of organic resins due to their higher stability but these materials are often neutral or anionic, thus extended cationic structures are of special interest in the field of anion separation. Layered double hydroxides (LDHs) are cationic isostructural clay-like materials that have been widely studied for their anion exchanging properties. However, LDHs are known to have a high affinity towards ubiquitous carbonate ions, as well as tendency to re-intercalate water molecules immediately after calcination. This drastically decreases their overall uptake capacity and selectivity for the capture of anionic pollutants from wastewater.

Metal-organic frameworks are promising materials in the field of separation due to the tunability in their structure and function. Cationic metal-organic frameworks are a subclass of these crystalline extended materials, which can be easily prepared by introducing neutral organic ligands for cationic metals and weakly coordinating anions that balance the overall cationic charge of the framework. These cationic materials offer a viable alternative to conventional anion exchangers due to their robust tunable frameworks that can exchange anions reversibly at high adsorption capacities.

A detailed methodology for the efficient separation of perchlorate from water was demonstrated by utilizing a cationic MOF consisting of three-dimensional [Ag-bipy]$^+$ chains arranged in a T-shaped pattern with nitrate anions counter-balancing the framework. Ambient conditions were used for both the synthesis of this cationic material, silver 4,4'-bipyridine nitrate (SBN), as well as the exchange resulting in the formation silver 4,4'-bipyridine perchlorate (SBP). The exchange was complete within 90 minutes and the capacity was 354 mg of ClO_4^-/g of SBN, representing 99% ClO_4^- removal. SBN exhibited superior performance compared to that of current anion exchangers such as the resins Amberlite IRA-400 (249 mg/g) and Purolite A530E (104 mg/g), as well as layered double hydroxides (28 mg/g). Unlike resins and layered double hydroxides, SBN could be successfully regenerated in nitrate solution at 70 °C with new crystal formation, allowing indefinite cycling for perchlorate capture.

An in-depth investigation of the host-guest interaction of cationic [Ag-bipy]$^+$ MOFs with perchlorate was carefully performed. The structural transformation and flexibility of SBN upon formation of SBP was evaluated by monitoring the anion exchange dynamics using a combination of powder X-ray diffraction (PXRD) with multinuclear ^{13}C, ^{15}N and ^{109}Ag solid-state nuclear magnetic resonance (NMR) spectra at different time intervals of the anion exchange. The structural transformation from SBN to SBP is complete within 70 minutes and was determined to take place by a solvent-mediated process. This pathway is confirmed by the morphological changes of the two crystalline materials observed by scanning electron microscopy (SEM).

The understanding of such structural dynamics highlighted in this study provides crucial insights for the rational design of related MOFs toward the selective capture of environmental pollutant oxo-anions

Increasing antibiotic resistance of pathogens has become a serious threat to public health. An effective approach to control the spread of antibiotic resistant bacteria is to consider a material that exhibits this broad-spectrum biocidal activity both in liquid environments, and on solid surfaces. Recently, the field of nanotechnology has incorporated these metals into nanostructured systems for improved dosage forms and therapeutic effects. Unlike conventional antibiotics, the antibacterial activity of nanomaterials is broad-spectrum, and includes physical damage to bacterial cells. Recently, MOFs and coordination polymers (CPs) have gained significant attention for their potential use as bactericidal materials. Their antibacterial properties typically originate from the metals in their cationic form, with the structures acting as metal ion reservoirs. We successfully performed a study highlighting the synthesis, antibacterial properties and mechanism of two Zn-based coordination polymers. The first, $[Zn(bipy)(OH_2)_4{}^{2+}]_{1.5}[ClO_4{}^{-}]_3 \bullet (bipy)_3(H_2O)$, consists of a one-dimensional (1D) structure with two crystallographically independent octahedral zinc centers trans-coordinated by two 4,4'-bipy units and water groups. The second, $[Zn_{1.5}(CH_3CO_2)_2(bipy)_2{}^{+}][ClO_4{}^{-}] \bullet H_2O$, is a two-dimensional (2D) layered structure with the same polymers but bridged together into a layer by acetate and 4,4'-bipy. Both compounds exhibit sustained release of Zn^{2+} ions upon their gradual degradation in aqueous solution, which results in highly

effective antibacterial activity towards *Escherichia coli* and particularly towards *Staphylococcus epidermidis* cells. This activity was evaluated in solution by broth dilution assays to determine minimal inhibition concentrations (MICs) as well as in the solid phase by agar diffusion tests to quantify the zones of inhibition (ZOI), and were in close agreement. Further, the biocidal mechanisms of the coordination polymers were investigated *in vivo* by fluorescence microscopy utilizing CellRox Green and propidium iodide as reactive oxygen species (ROS) and membrane disruption indicators, respectively. Both CPs show superior antibacterial activity compared to two standards, zinc acetate and zinc oxide. This superior activity is attributed to the gradual and localized release of Zn^{2+} ions, as well as the electrostatic attraction to the bacterial cell surface afforded by their unique structures.

Dedication

This work is dedicated to my parents
Rebeca Magaña and Enrique Colinas,
and my brothers Diego and Fernando Colinas.
In the immensity of your love and never-ending support
I find the courage to be a better man,
and the inspiration to be a better scientist.

Acknowledgements

I would like to first and foremost thank my advisor, Professor Scott Oliver, for believing in me and giving me the freedom to explore my passion for chemistry, while providing the guidance and support I needed to reach my full potential as a scientist. I'm grateful for the support of my committee members, Professor Yat Li, Shaowei Chen, and Dr. Stacey Zones for their valuable insight and support that allowed me to become a more critical scientist.

I would like to acknowledge my dear colleagues in the Oliver research group for providing a nurturing and intellectual environment based on support and collaboration: Dr. Honghan Fei, Dr. Jessica Palomino, Dr. Yashar Abdollahian, Jesse Hauser, Susan Citrak, Ana Kareh, Eaindar Soe, Beatriz Ehlke, Derek Popple, Rachel Silva, Kat Tabler, Kareem Bdeir, Kevin Delgado-Cunningham. In addition, I would like to thank my collaborators starting with Professor Frédéric Blanc and his research group at the University of Liverpool for kindly hosting me during the Summer of 2015 in England, and for his work and efforts that resulted in a fruitful collaboration. Rob Franks for all his patience and support when assisting with IC and ICP analysis, Dr. Tom Yuzvinsky for his expertise and assistance in the acquisition of SEM images, and Professor Chad Saltikov for his assistance and facilities used for bacterial cell viability studies.

Finally, I want to express my sincere gratitude to Yulianna Ortega for believing in me since I was an undergraduate student, and always offering her honest advice and support through IMSD. Your work and compassion has made a difference in the professional careers of many underrepresented scientists, I am fortunate to be one of them.

Financial support was provided by the National Science Foundation under Grant No. 1603754 from the CBET Environmental Engineering Program, and by a graduate fellowship from the Initiative for Maximizing Student Development (IMSD) program funded by the National Institutes of Health under Grant No. 2R25GM058903-17.

Chapter 1

Cationic Metal-Organic Frameworks for Applications in Wastewater Treatment by Anion Exchange

Abstract

The freshwater supplies are in risk of not meeting the increasing global demands of this essential resource as a result of the rapid growing population and detrimental pollution. A considerable amount of EPA priority water pollutants consist of inorganic oxyanion species that are persistent due to their high mobility in aqueous environments, making them resistant to traditional wastewater technologies. An example of these anionic pollutants is perchlorate, an emerging groundwater contaminant released into the environment by the improper dismantling of military weaponry and rockets, which is known to induce thyroid disruption. These oxyanion pollutants can be separated from freshwater sources via anion exchange using organic resins, activated charcoal, and layered double hydroxides. Currently, organic resins are the conventional material for the perchlorate remediation, but their performance is severely affected by their poor selectivity and lack of recyclability. Metal-organic frameworks are promising materials due to the tunability in their structure and function. Cationic metal-organic frameworks are a subclass of these crystalline extended materials, which can be easily prepared by introducing neutral organic ligands for cationic metals and weakly coordinating anions that balance the overall

cationic charge of the framework. These cationic materials offer a viable alternative to conventional anion exchangers due to their robust tunable frameworks that can exchange anions reversibly at high adsorption capacities.

1.1 The issue of Wastewater Pollution

Water is one of the world's most abundant resources, but only 2.5% of the global supply is freshwater, from which roughly 0.5% is available and safe for human consumption due to the rest being inaccessible.[1] These limited resources of available freshwater are mainly comprised of groundwater, lakes and rivers; and they are becoming increasingly scarce due to the rapid growth of global population, increasing development of industrialization as well as greater energy demands.[2] The United Nations (UN) Water Organization has estimated that about 1.8 million people will be living in regions with absolute water scarcity, and two-thirds of the world could live under water stress conditions by 2025.[3] These water stress conditions will not only result as a consequence of the increasing demand for freshwater, but also due to the detrimental pollution of both surface and groundwater by the release of wastewater into the environment. The environmental protection agency (EPA) defines wastewater as the flow of used water discharged from industrial, agricultural and residential areas; which may contain a wide range of pollutants including toxic inorganic and organic chemicals.[4] Among the listed priority inorganic pollutants are metals and metalloids that may be released in the environment from industrial wastewater, combustion of fossil fuels, and radioactive waste produced from nuclear power generation.[5] In the case of organic pollutants, these include anionic pharmaceuticals or metabolites, organophosphate pesticides, dyes and industrial solvents.[6] Inorganic contaminants are generally more persistent in the environment than organic contaminants, as these metals and metalloid species readily oxidize to form oxyanions due to the high temperatures and varying pH conditions used in industrial processes.[7] Many water and wastewater treatment methods do not effectively remove these emerging pollutants, or are not capable of meeting the increasingly stringent water standards. Hence, novel alternative pollutant remediation methods to complement or replace the existing methods with better efficiency and sustainability are urgently required.[8]

1.2 Oxyanion Pollutants

Oxyanions are contaminants present in water sources and treated drinking water as a result from the oxidation of metals and metalloids released from anthropogenic sources. These species consist of a central atom bonded to oxygen atoms, and can be mononuclear or polynuclear depending on the pH and metal concentration. Several of these oxyanions can be toxic to human and wildlife even at parts per billion (ppb) level concentrations; examples include chromate (CrO_4^{2-}), arsenate (AsO_4^{3-}), molybdate (MoO_4^{2-}), pertechnetate (TcO_4^-), and perchlorate (ClO_4^-).[9] Given that these inorganic pollutants are charged species, they tend to be highly soluble in water making them a very bioavailable form of pollution that is resistant to traditional wastewater treatment technologies such as adsorption, filtration, reverse osmosis, and bioremediation.[10] Therefore, the release of oxyanion pollutants into the environment poses a serious threat to the water supply. The occurrence and toxicity of some of these oxyanions will be discussed in this section with special emphasis on perchlorate as it pertains to the work presented in this thesis.

1.2.1 Chromate

Chromium is an abundant transition metal that has been used since the early civilizations for various applications including metallurgy, leather tanning, wood preservation, chemical catalysis, etc. The improper disposal and leeching of chromium from various materials has made this metal a priority pollutant. According to the toxic release inventory, in the year 1997 the estimated release of chromium to water was 111,384 lbs. from 3,391 large processing facilities in the metallurgy industry.[11] Although chromium exhibits a wide range of oxidation states, it is most commonly found as Cr(III) and Cr(VI) in nature with Cr(III) being the most stable oxidation state. While trivalent chromium is an essential micronutrient, hexavalent chromium is known to be carcinogenic. The latter forms a tetrahedral chromate ion in neutral aqueous conditions, and it is readily taken up by cells by non-selective channels due to its similarity to phosphate (PO_4^{3-}) and sulfate (SO_4^{2-}), which are used extensively in humans for many biochemical processes. In contrast to hexavalent chromium, trivalent chromium forms a polymeric hydroxo species that lack resemblance to biological nutrients and has lower solubility. Hence, trivalent chromium has much lesser cellular uptake, and is therefore 500 times less toxic to a human cell than hexavalent chromium.[12] Once in the cell, hexavalent chromium is rapidly reduced to pentavalent chromium species by the action of , giving rise to highly reactive oxygen species that may cause DNA cleavage and adduct formation.[13]

1.2.2 Arsenate and Arsenite

Arsenic is a metalloid that is naturally occurring in many mineral forms predominantly associated with zinc, lead and copper ores, and it's commonly found in low levels in most soils. It exists in inorganic and organic forms and in different oxidation states (-3, 0, +3, +5). The occurrence of arsenic in freshwater supplies originates primarily due to wide its industrial use as major component in semiconductor electronic devices, car battery alloys, and former use in pesticides. Another source of arsenic exposure can be through naturally occurring deposits that may leech into wells, as in the case of Bangladesh where deep tube wells were contaminated with levels of arsenic up to 1000 µg/L; which exceeded the limit set for drinking water in the region (50 µg/L) or that recommended by the World Health Organization (10 µg/L).[14] It was estimated that the number of people exposed to arsenic concentrations above 50 µg/L was about 21 million in 1998 with a death toll of approximately 40,000. The lethal dose of arsenic for humans is estimated to be of only 3 mg/kg due to the ability of the tetrahedral arsenate anion to replace phosphate once it enters the body. It was demonstrated by an *in vitro* experiment that arsenate can uncouple the formation of adenosine-5'-triphosphate (ATP) by a mechanism termed arsenolysis. This observation was further verified in an experiment conducted with rabbit and human erythrocytes which revealed depletion of ATP after *in-vitro* exposure to arsenate.[15]

1.2.3 Pertechnetate

Technetium is the lightest element whose isotopes are all radioactive. This metal is produced synthetically for its application in nuclear medicine as a radioactive tracer in medical imaging equipment. Specifically, technetium-99m is used as a medical diagnosing tool because of its detectable gamma rays of 140 keV and its relatively short half-life of 6.006 hours. A minute amount of technetium occurs naturally in the Earth's crust as a spontaneous fission product in uranium ores, but the its occurrence in the environment prevails from the improper discharge from nuclear processing plants. Over the past 20 years it has become an increasingly important public concern because Tc-99 is a long-lived radionuclide (β-emitter) with a half-life of $2.13\text{x}10^5$ years.[16] The current method of containment for this radionuclide requires its vitrification, but this method has proven to be ineffective as a significant amount is known to have leeched into nearby water supplies. Upon contact with aqueous environments this radionuclide is found in the form a tetrahedral pertechnetate anion (TcO_4^-), which is highly mobile and persistent accounting for bioaccumulation in plants and animals.[17]

1.3 Perchlorate as an Environmental Contaminant

The issue of perchlorate as an emerging trace pollutant has gained significant attention as it has become widespread in many countries including the United States, Japan, Korea, India, Germany, and China.[18] This oxyanion is composed of one chlorine atom surrounded by four oxygen atoms arranged in tetrahedral geometry. It has been used for decades in the United States national defense and space programs predominantly in the form of ammonium perchlorate as an oxidizer of choice for solid propellants because of its performance, ease of handle, and safety. Ammonium perchlorate is a major component in most solid rocket propellants due to its high oxygen content, and the fact that it decomposes into the gaseous phases of water, O_2, N_2, and HCl, leaving no residue.[19] However, perchlorate salts are significantly hygroscopic and do not function well in solid-fueled rockets upon adsorption of water, which requires replacing such solid oxidant periodically. The presence of perchlorate in freshwater, mainly groundwater, originates from the improper disposal of solid salts of ammonium, potassium or sodium perchlorate upon dismantling of military weaponry and discharge of rocket fuel manufacturing plants. In addition to these salts being highly soluble in water, perchlorate is kinetically inert to reduction and has little tendency to adsorb to mineral or organic surfaces. Hence, this oxyanion is highly mobile and persistent in groundwater which makes its fate largely influenced by the hydrology of the environment.[19]

Early analytical methods of perchlorate determination were based on gravimetry with organic dyes, such as “nitron”, that relied on the anion’s ability to form insoluble complexes. The main limitation of this methodology originates from the significant interference caused by competing anions due to perchlorate’s weak ligating ability.[20] The true extent of perchlorate contamination was not validated until the late 1990s when more sensitive methods such as ion chromatography (IC) allowed to detect perchlorate in drinking water, groundwater, soil, plants, fertilizer, and foodstuffs. The US EPA published Method 314.0 for the detection of perchlorate utilizing an ion chromatography system consisting of an ion-exchanging resin as well as electrolytic conductivity suppression and conductivity detection. The detection limit of this method is 0.53 parts per billion (ppb) with a widely achievable minimum reporting limit (MRL) of 4 ppb.[21]

In a report on the occurrence of perchlorate by the American Water Works Association it was indicated that perchlorate contamination is a national problem with significant concentrations found in 26 states. California, Utah, and Nevada are the three most affected states, with perchlorate concentrations ranging from 8 ppb to 3.7 parts per thousand (ppt) since they the draw water from the Colorado river, which was heavily affected by two perchlorate-manufacture companies that released approximately 1000 pounds of perchlorate per day from the late 1950s up to the late 1990s.[22] Exposure to perchlorate is known to disrupt the function of the thyroid by inhibiting the cellular uptake of iodide. The perchlorate ion, due to its similarity to iodide in ionic size and charge, competes with iodide for uptake into the thyroid gland by the sodium-iodide symporter. At significant doses of perchlorate, competitive inhibition will inhibit iodide from entering in the thyroid resulting in a reduced production of the thyroid hormones, triiodothyronine (T_3) and thyroxin (T_4), and an associated compensatory increase in thyroid stimulating hormone (TSH).[23] Thyroid hormones T_3 and T_4 are essential to the regulation of oxygen consumption and metabolism throughout the body, and reduction of such hormones may lead to altered neurodevelopment in fetuses as well as hypothyroidism.

1.4 Separation of Oxyanions via Anion Exchange

Ion-exchange technology has been used for drinking water and wastewater treatment for over a half century. Ion exchange is the process by which ions of interest in the solution phase are selectively removed by exchange with ions associated with a synthetic solid phase corresponding to the ion-exchanging material, which generally exhibits a surface with active sites where the exchange of ions takes place.[24] Ion exchangers are of two kinds i.e. cation and anion exchangers which have the capacity to exchange cations and anions, respectively. Due to the anionic nature of many other EPA priority pollutant species, efficient anion-exchanging materials that can perform selective separation are sought. The most commonly used anion exchangers are synthetic organic resins, functionalized activated charcoal, and inorganic extended structures such as sodium silicates, zeolites, layered double hydroxides (LDHs), and various metal oxides. These ion-exchanging materials exhibit different structural properties that makes them suitable for different conditions including the nature and concentration of the ion of interest, the presence of competing ions, temperature and pH of the water source, etc. Two of the main criteria that makes an ion exchanging material efficient is the ability to perform high capacity, reversible and selective anion separation. A reversible anion exchange reaction will allow for the anion exchanger to be used for multiple cycles, and thus increasing the cost efficiency of such material. Conversely, an anion exchanging material that exhibits selectivity towards a pollutant of interest will result in an efficient separation due to the presence of various competing anions in both surface water and groundwater.

1.4.1 Ion-exchange Resins

Ion exchange resins are considered to be the most viable method for anion exchange, and are currently the most widely used materials for separation of pollutant anions including perchlorate. These matrices generally consist of a divinylbenzene-cross-linker polystyrene backbone with terminal quaternary ammonium cationic side groups that possess an exchangeable counter-anion i.e. chloride.[25] Most of the manufactured resins are prepared as macroporous beads of 0.5-1 mm in diameter with an open structure that allows for the sorbed chloride ions to be readily exchanged by the ion of interest, i.e. perchlorate (Figure 1).[26]

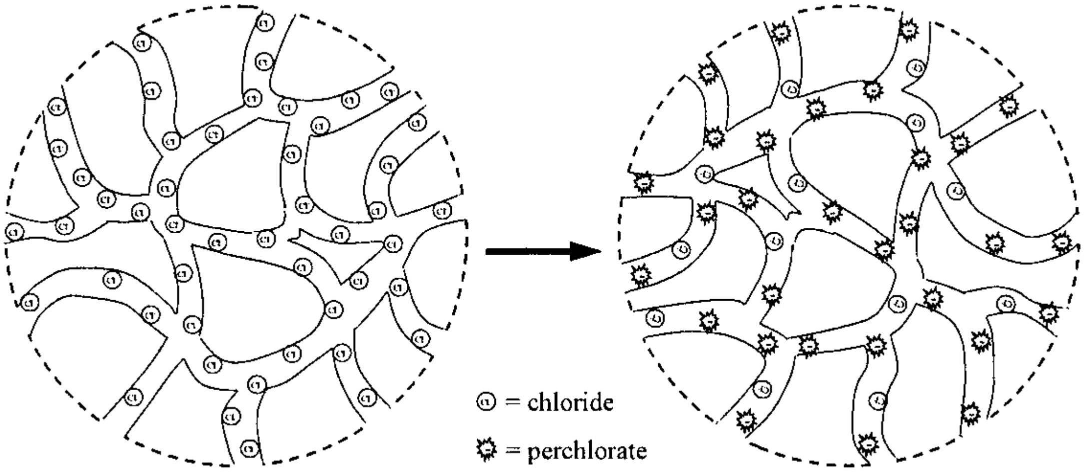

Figure 1.1 Schematic of the binary ion exchange between perchlorate and chloride ions on a synthetic resin bead.

In the case of perchlorate separation shown in Figure 1.1, the resin beads are exposed to a solution containing perchlorate anions which will enter the resin bead in exchange for the chloride ions. At equilibrium, the exchange bead and solution will contain both anions at a different ratio that will be indicative of the selectivity of such resin. Several structural modifications have been performed in effort to enhance the selectivity of the resins by changing the quaternary ammonium functional groups. In the case of perchlorate separation, it was found that the selectivity increased with increasing hydrophobicity and size of quaternary ammonium group, from which tributyl ammonium groups were determined to be good candidates for perchlorate selective resins.[27]

Although these anion exchange resins can be functionalized to increase their selectivity making them more cost efficient, an even more cost-effective approach would require the regeneration of these resins to further reduce the capital cost. The higher affinity for perchlorate exerted by the functionalized resins has made the regeneration a significant challenge even by washing with concentrated brine solution which generates large amounts of secondary waste. Several attempts of regenerating both selective and non-selective resins were made using various NaCl concentrations and even heat, but both methods were found to remove only a small portion of the loaded perchlorate anions from the resins.[28,29] In addition to the lack of reusability, these resins are known to exhibit poor chemical and thermal stability due to their organic polymeric nature. For example, approximately 15% of their ion exchange capability is lost upon contact with water at 90 °C, and 64% and 57% their ion exchange capacity in the presence of hypochlorite and hydrogen peroxide, respectively.[30]

In summary, anion exchange resins are the conventional material for the separation of perchlorate and other oxyanions due to their ease of use and production. However, these polymeric resins require further optimization in order to increase their cost efficiency and performance which will allow to meet the requirements set by the EPA and WHO at various plume site water treatment facilities. Hence, innovation of novel materials with superior stability and performance is of crucial importance.

1.4.2 Functionalized Activated Charcoal

Activated Carbon (AC) has been used as the conventional adsorbent for the removal of pollutants due to its low cost and unique adsorption properties resulting from its high surface area, micropores, and broad range of surface functional groups.[31] However, its small particle size, and poor selectivity are known to hinder the performance of this porous carbon material. In effort to improve the selectivity of AC for the removal of perchlorate and other oxyanions, several modifications have been performed in order to obtain a cationic surface that would result in a greater affinity for anionic pollutants. A successful attempt at making AC more effective for perchlorate separation was done by preloading the AC with iron, which was grafted onto the surface of AC by an initial treatment with oxalic acid solution.[31] The cationic charge originating from the iron grafted on the AC surface improved the perchlorate adsorptive capacity by 42%. However, in addition of the secondary waste generated from the treatment with oxalic acid and iron, only 65% of the original adsorption capacity could be restored upon treatment with sodium borohydride. Further, another strategy to increase the positive surface charge density and consequently the adsorption of perchlorate by AC consisted in tailoring the porous carbon material with ammonia at high temperatures. This was done by utilizing gaseous ammonia at temperatures between 500-800 °C, which not only increased the cationic charge density but also the micropore volume resulting in a four-fold increase of perchlorate adsorption compared to the virgin AC.[32] Although modified AC is presumably a more stable material with the ability of being tailored for a more selective separation of anionic pollutants and potentially regenerable, the cost efficiency of this technology remains low due to the high temperatures and secondary waste generated in order to develop an efficient method of separation.

1.4.3 Surfactant Modified Zeolites

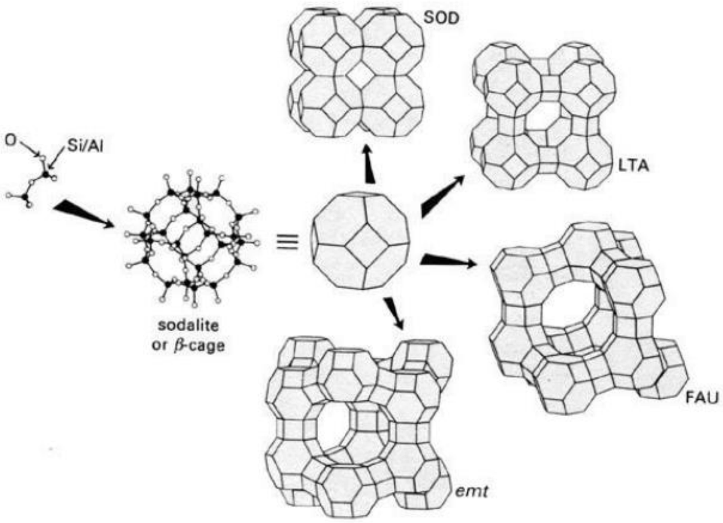

Figure 1.2 SiO_4 tetrahedra forming sodalite cage to give rise to different zeolitic structures.

Zeolites are naturally occurring hydrated aluminosilicate minerals characterized by their robustness and high internal and external surface areas, which allows for their wide industrial use as catalysts, sorbents, molecular sieves and ion exchangers.[33] They are built up from corner-sharing SiO_4 and AlO_4-tetrahedra to give rise to three-dimensional microporous structures (Figure 1.2). The ion exchanging properties of these materials originate from the inherent anionic charge of their porous silica or aluminosilicate framework that renders the possibility of cation exchange. The ability of these materials to perform cation exchange has been traditionally applied for water softening applications as they readily exchange the sodium ions that are counterbalancing the framework by both magnesium and calcium.[34]

These cation exchange properties of zeolites have been exploited to modify their surface chemistry such that other classes of compounds, such as anions or non-polar organics, could be also be exchanged or captured.[35] The use of cationic surfactants has been one of the most widely used strategies to modify the surface of zeolites, which can be easily achieved by exchanging with the inorganic cation on the external surface. The use of quaternary amine surfactants, such as hexadecyltrimethylammonium (HDTMA), is preferred due to their long chain and permanent cationic charge that can form a surfactant monolayer with anion exchange properties. This strategy was demonstrated by comparing two natural zeolites to a surfactant-modified zeolite with HDTMA for the sorption of chromate, selenate, and sulfate.[36] As shown in Figure 1.3, the surfactant modified zeolites displayed a significantly superior sorption due to the favorable interaction with the cationic bilayer from the surface modified frameworks that resulted in a surface precipitation of a surfactant-oxyanion complex. The main drawbacks of this strategy lie in the waste generated in the process of exchanging the surfactant in the surface of the zeolites, as well as the decreased thermal and chemical stability due to the organic functionalization.

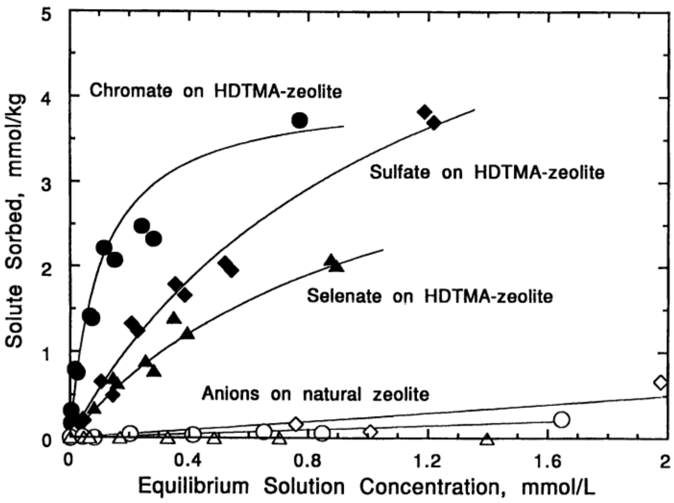

Figure 1.3 Sorption of oxyanions by HDTMA-treated zeolite.

1.4.4 Layered Double Hydroxides (LDHs)

Layered double hydroxides (LDHs) are a widely studied class of two-dimensional extended structured clay minerals, which are also known as hydrotalcite like materials. Their structures are made up of brucite-like ($Mg(OH)_2$) layers where a fraction of the divalent cations coordinated by hydroxyl groups have been isomorphously replaced by trivalent cations giving rise to their inherent cationic charge.[37] These infinite cationic brucite-like sheets consist of edge-sharing $M(OH)_6$ octahedral units, and are stacked on top of each other, held together by hydrogen bonding interactions. As shown in Figure 1.4, the net positive charge of the layers is counterbalanced by exchangeable anions intercalated into the interlayer space along with water groups, and the total thickness of the brucite-like sheets and the interlayer space is denominated the basal spacing (c').[38]

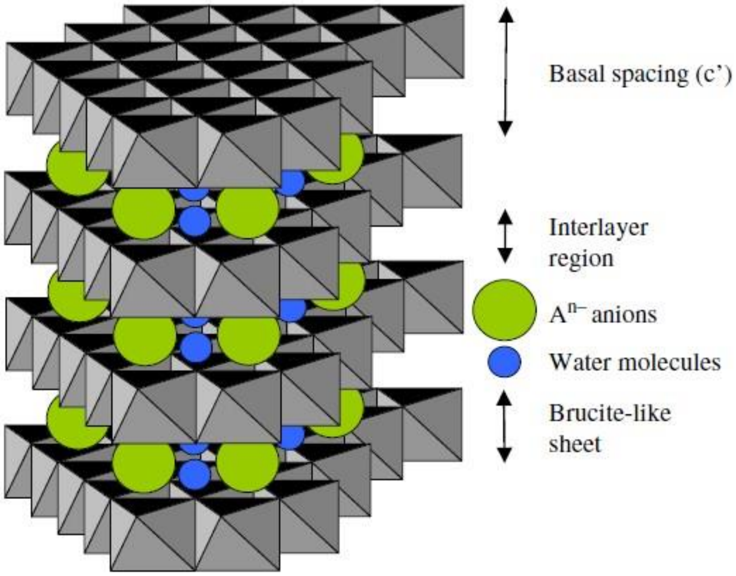

Figure 1.4 Schematic of a general LDH structure.

In general, LDHs can be represented by the formula $[M_{1-x}{}^{2+}M_x{}^{3+}(OH)_2]^{x+}(A^{n-})_{x/n} \cdot H_2O$, where M^{2+} and M^{3+} are divalent and trivalent cations, respectively; the value of x is equal to the molar ratio of $M^{3+}/(M^{2+}+M^{3+})$, whereas A is the interlayer anion of valence n. The most common example of these layered clay materials is the naturally occurring mineral hydrotalcite which has the formula $Mg_6Al_2(OH)_{16}CO_3 \cdot 4H_2O$. However, a wide variety of isostructural materials with diverse physicochemical properties exist due to the plethora of identities for M^{2+}, M^{3+}, x and A^{n-}.

The preparation of LDH materials is commonly done by the coprecipitation method, in which aqueous solutions of M^{2+} and M^{3+} containing the anion that is to be intercalated into the LDH are used as precursors. The synthesis is carried out under supersaturation conditions to ensure simultaneous precipitation of the two cations, and generally there are two conditions for this method involving low and high supersaturation. Coprecipitation reactions at low supersaturation are known to yield better quality crystals and is performed by slow addition of mixed solutions of the metal salts at the selected ratio into the reactor containing the desired anion followed by a second solution containing an alkali to maintain the desired pH that allows for the coprecipitation of the two metallic salts to occur. In contrast, coprecipitation at high supersaturation involves the addition of the mixed salt solution to an alkaline solution containing the anion, which gives rise a to a large number of crystallization nuclei. After precipitation, a thermal treatment is performed to increase the crystallinity of the product followed by an aging process at 500 – 600 °C for several hours.[39] LDHs can also be prepared by the ion exchange method, which is useful when the coprecipitation method is inapplicable, e.g. when metal cations are unstable in high pH solutions. The ion exchange method allows the guests to be exchanged with the anions present in the interlayer region to produce specific anion-pillared LDHs.[40] The hydrothermal method can also be employed when guest species with low affinities are required to be intercalated into the interlayers, and when the ion exchange and coprecipitation methods are not applicable. This method has been shown to be effective at obtaining higher crystallinity products, and is often employed using urea as a pH modifier and source of carbonate anions.[41]

Powder X-ray diffraction (PXRD) is the most common technique for the characterization of LDHs since it allows one to identify the phases of these layered materials. The typical X-ray patterns of LDHs contain sharp basal (0 0 l) reflections at low 2θ corresponding to successive orders of basal spacing (c'), whereas weak non-basal reflections are observed at higher values of 2θ. The interlayer spacing can be determined from the difference of the basal spacing and the brucite-like sheet thickness of about 4.8 Å, and such value will be dependent on the size and orientation of the counterbalancing anion. Further, the ratio of M^{2+}/M^{3+} can be estimated from the parameter "α" which can be determined using the d-spacing of the (110) as indicated by the following formula:[42]

$$\alpha = 2d_{110}$$

Table 1.1 Adsorption capacities of oxyanion pollutants by LDHs[38]

Oxyanion	Type of LDH	Adsorption Capacity (mg/g)
Arsenite	Uncalcined Mg-Al-chloride-LDH	0.086
Arsenite	Calcined Mg-Fe LDH	87.5
Arsenate	Uncalcined Mg-Al LDH	32.6
Arsenate	Calcined Mg-Al LDH	202
Chromate	Uncalcined Mg-Al LDH	5-40
Chromate	Calcined Mg-Al LDH	120
Phosphate	Uncalcined Mg-Al LDH	28.8
Phosphate	Calcined Mg-Al LDH	81.6
Borate	Uncalcined Mg-Al LDH	14
Selenite	Uncalcined Mg-Al LDH	270
Selenite	Calcined Mg-Al-Zr LDH	29

Fourier Transform Infrared (FTIR) spectroscopy is also widely used for the characterization of LDHs as it allows one to investigate the vibrations in the octahedral lattice corresponding to the hydroxyl groups. In addition, FTIR can be used to identify the presence of the intercalated anions by providing information about the vibrations of the bonds formed by these anions.[43] Another technique widely used to characterize LDH materials is thermogravimetric analysis (TGA), which is used determine the thermal stability and the fraction of volatile components by monitoring the weight loss as the sample is heated. The thermal profile is generated in the form of a plot indicating the weight loss as a function of temperature, from which the identity of the anions can be stoichiometrically identified.

LDHs have been considered a plausible alternative to anion exchange resins due to their inherently cationic host framework that affords the ability to exchange a wide variety of anions upon intercalation. In addition to the greater stability endowed by their robust framework, these layered materials can also exert reversible anion exchange which increases their cost efficiency significantly.[44] The anion exchange intercalation reactions are typically carried out via batch test experiments, in which the LDH material is exposed to a solution with the anion of interest; and upon stirring, the guest anion in the interlayer space will exchange with the anion present in solution. This anion exchange intercalation process has been used for the removal of several oxyanion pollutants reported in Table 1.1 above.

One of the main drawbacks that limits the industrial use of LDH for separation of pollutants is that these materials exhibit a peculiar feature known as the "memory effect" which severely limits their adsorption capacity. This occurs upon calcination of the LDH material to remove interlayer water molecules, which causes the material to enter a metastable state of high basicity. The memory effect takes place upon exposure of the calcined LDH to moisture, as it will re-intercalate water molecules in the interlayer space to reform the original LDH structure with great fidelity.[45] Nonetheless, in some circumstances this property can have positive outcomes by increasing the adsorption capacity of calcined layered double hydroxides (CLDH) materials. In effort to apply the memory effect to increase the perchlorate uptake of a Mg/Al LDH, an in-depth study was done comparing the anion exchange of the CLDH to that of the LDH materials.[46] It was determined that the CLDH material exhibited a superior adsorption capacity driven by the memory effect of the LDH with perchlorate as interlayer re-intercalated anion compared to the non-calcined LDH which displayed limited binding sites due the presence of carbonate (Figure 1.5). In effort to investigate the efficiency of CLDHs capturing perchlorate, a separate study was done on the influence of the metal cations and M^{2+}/M^{3+} molar ratios. The results summarized in Table 1.2 show that the CLDH with the highest adsorption capacity for perchlorate consisted in Zn/Al at a molar ratio of 2.[47]

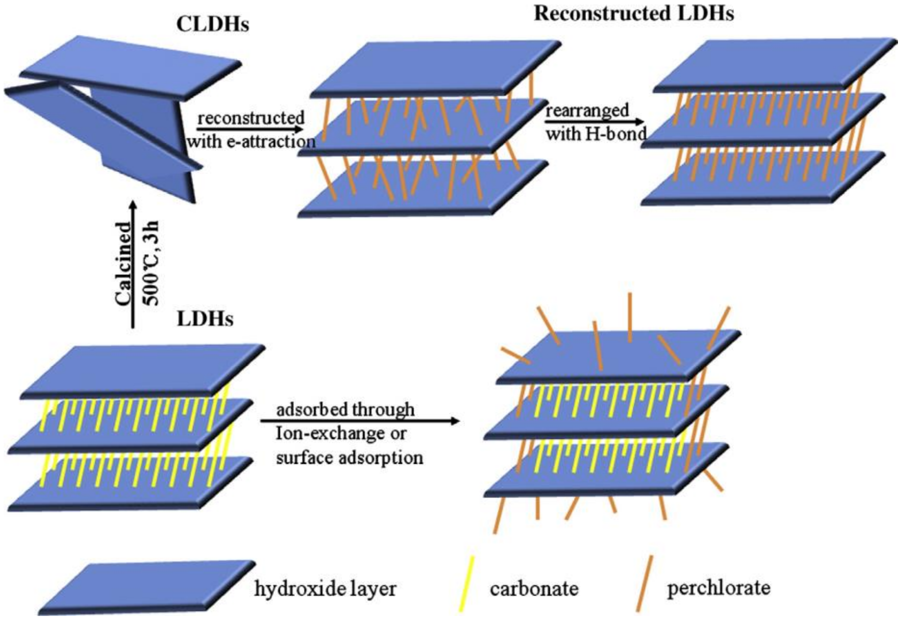

Figure 1.5 Scheme of perchlorate uptake mechanism by LDHs and CLDHs. Adsorption of perchlorate to LDH was limited to the outer surfaced of hydroxide layer.

Table 1.2 Effect of chemical composition calcined LDH layers on removal of perchlorate[47]

Type of LDH	Dosage of LDH	Adsorption Capacity (mg/g)
Mg/Al_2	0.0500	96.70
Mg/Al_3	0.0500	88.55
Mg/Al_4	0.0500	58.70
Zn/Al_2	0.0500	99.85
Zn/Al_3	0.0500	93.89
Chromate	0.0500	83.59
Phosphate	0.0500	2.90
Phosphate	0.0500	7.92
Borate	0.0500	48.23

In addition to the memory effect, selectivity has been an issue which has limited the industrial application of LDH materials. The limited selectivity of LDH materials has been attributed to their strong affinity for carbonate and/or bicarbonate that enables the re-intercalation of carbonate species versus other anions present in solution. The anion affinity of LDHs obeys the following order:[48]

$$CO_3^{2-}>SO_4^{2-}>OH^->F^->Cl^->Br^->NO_3^->I^-$$

The limited selectivity of LDHs drastically reduces the adsorption capacities due to the ubiquitous nature of CO_2 in the atmosphere. In addition to the poor selectivity and the pre-calcination treatment required to evacuate the interlayer water, these materials also display difficulty in recovery and reusability after anion exchange. LDHs often form a gel and require approximately 30 min of centrifuging for total separation from solution.

1.5 Metal-Organic Framework (MOFs)

1.5.1 Structural Properties

Metal-organic frameworks (MOFs), or coordination polymers as they are also known, have been intensively studied over the past decade because they represent a new category of hybrid inorganic-organic materials with extensive surface areas, high porosities, and an extraordinary tunability of their structure, dimensions, and shape. Their structural versatility comes from the fact that these hybrid materials are composed of isolated metal atoms or clusters that are linked by polyfunctional organic ligands to create open crystalline frameworks with permanent porosity (Figure 1.6). The tunable porosity and vast topologies that can be attained with these extended crystalline materials have made them widely studied for the utilization in the fields of gas storage, size-selective catalysis, sensing, and drug delivery.[49–52]

As in the case of inorganic frameworks such as zeolites, where the repeating tetrahedral SiO_4 units are referred to as a secondary building unit (SBU), the metal cluster in MOFs can be also defined as an SBU. The flexibility with which the SBUs and organic linkers can be varied has led to thousands of new structures with vast structural diversity. An example of this reticular synthetic strategy can be visualized by comparing the structures of the two prototypical coordination polymers, MOF-5 and MIL-101, which both have benzene dicarboxylate (BDC) linking the Zn_4O and Cr_3O SBUs, respectively. The resulting structure of MOF-5 consists of a three-dimensional cubic network with interconnected pores of 12 Å in diameter, while MIL-101 results in a drastically different mesoporous structure consisting of large cages of approximately 3 nm in diameter with pentagonal and hexagonal windows (Figure 1.7).

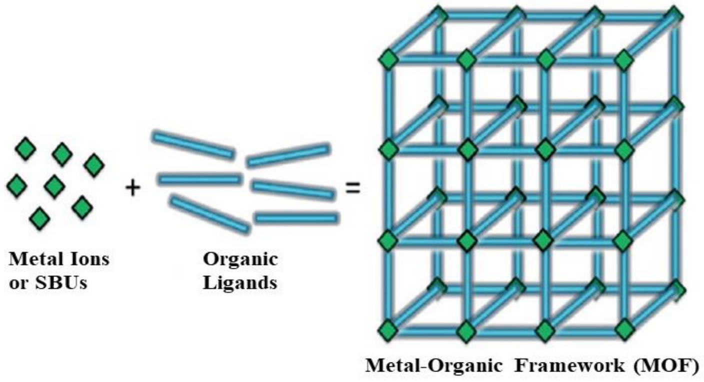

Figure 1.6 Simplified representation of a MOF where SBUs are connected by organic ligands to give a three-dimensional framework.[53]

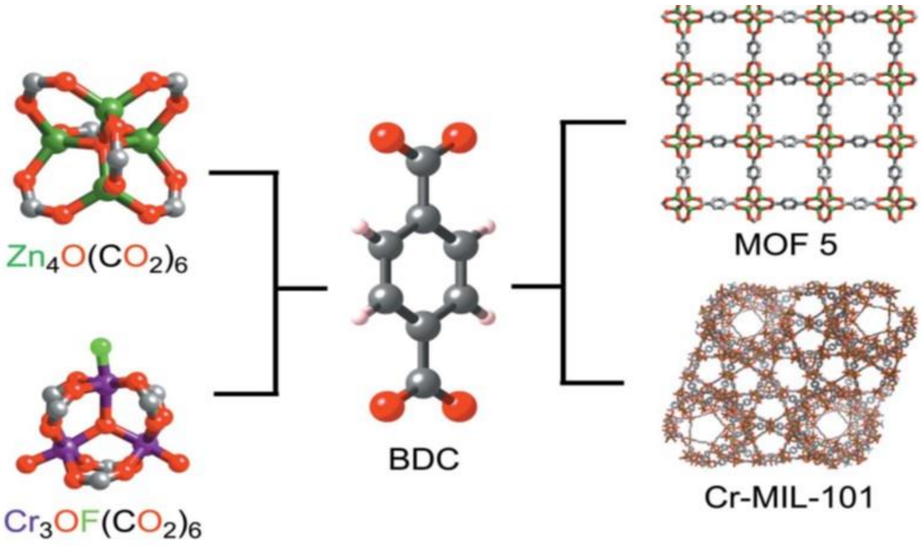

Figure 1.7 Examples of SBUs and resulting topologies reported in MOFs.[53]

The structural connectivity of these extended crystalline materials may consist of 1-D chains, 2-D layers, or 3-D frameworks depending on the geometry of the SBU as well the size and shape of the ligand. In addition to the strong coordination bonds that connect the SBUs with the organic linkers, the structures of MOFs are often comprised of hydrogen bonding, π-π interactions, as well as electrostatic attractions. In general, the overall charge of these structures tends to be neutral or anionic due to the coordination of positive metal centers with anionic oxygen-donor ligands. However, the formation of a cationic framework can be attained by using neutral nitrogen-donor ligands, allowing for the positive charge of the metal to be counterbalanced electrostatically by guest anions residing in the channels or pockets of the framework. The synthesis of cationic MOFs is of particular interest in the field of separation as these materials can be tailored for the selective capture of anionic pollutants by performing anion exchange with benign guest anions.

1.5.2 Synthesis of Cationic MOFs

The general strategy for the synthesis of MOFs involves the understanding of metal coordination environments, the functionality of organic linker molecules, as well as the knowledge of possible topologies that could result in a framework with a suitable topology for an application of interest. There is some lack of control over the character of solid crystalline structures, however, which is related to the fact that the precursors often do not maintain their structure during the reaction leading to poor correlation between reactants and products. The essence of MOF synthesis lies in the ability to establish the synthetic conditions that lead to defined inorganic building blocks without the decomposition of the organic ligand, while satisfying the kinetics of crystallization to allow for nucleation and growth of the desired phase. The coined term for a synthetic strategy that meets the above requirement is known as "reticular synthesis", which is defined as the process of assembling judiciously designed rigid molecular building blocks into predetermined ordered structures held together by strong bonding.[54]

The preparation of MOFs is generally carried out by liquid-phase syntheses in which a solution containing the metal salt and ligand is added to a reaction vessel. The choice of solvent can be based on reactivity, solubility, redox potential, stability constant, etc. The reaction temperature is one of the main parameters in the preparation of MOFs, and the two temperature ranges that will determine the reaction set up and instrumentation are known as solvothermal and non-solvothermal. The latter method involves reactions that take place below or at the boiling point of the solvent under ambient pressure, simplifying the synthetic requirements. This method is known to be very practical as it allows for simple room-temperature reactions, but generally the crystallinity of the product is affected. Solvothermal reactions are carried out in Teflon-lined steel autoclaves under autogenous pressure above the boiling point of the solvent, which allows for unexpected chemical changes that give rise to formation unique nanoscale morphologies and SBUs that are not achievable by other methods.[53] This method is considered to be the most advantageous due the formation larger crystals suitable for X-ray diffraction analysis. The most commonly used organic solvents are dimethylformamide, acetonitrile, ethanol, and methanol. The hydrothermal method utilizes water as a solvent and in addition of favoring the crystallization due to the lower viscosity of the solvent system, this method affords structures with greater water stabilities suitable for separation of pollutants from water.

1.5.2.1 Metals

The type of metal used in the synthesis of MOFs will significantly influence their structural properties based on the coordination preferences, charge, and radius of the metal species. The dimensionality of a framework will typically increase with increasing coordination number since this will directly affect the connectivity, allowing for more organic linkers to coordinate each metal atom or cluster. Although the type of ligand is mainly responsible for the preparation of a cationic framework, metals selection is vital for the tailored application of the resulting framework. MOFs have been successfully prepared using a variety of metals including alkaline-earth metals, alkali metals, transition metals, and rare-earth metals.

1.5.2.2 Ligands

The choice of ligands in the design of MOFs is crucial as it will influence the surface area, porosity, dimensionality and overall charge of the structure. An extensive number of materials have been made using carboxylate ligands due to the multiple binding geometries and their strong metal coordination that affords highly stable structures. However, these ligands are not preferred for the synthesis of cationic frameworks as the carboxylate groups tend to generate neutral and anionic structures when their negative charge outnumber the cationic charge of the metal center. An exception to this trend is witnessed in the structure of MOF-235, an iron(III)-based cationic framework prepared by Yaghi and coworkers, in which $[Fe_3O]^{7+}$ SBUs are connected by 1,4-benzenedicarboxylate (BDC) ligands to give rise to a $[Fe_3O(1,4\text{-BDC})_3(DMF)_3]^+$ framework with $[FeCl_4]^-$ located in the hexagonal pores counterbalancing the charge.[55]

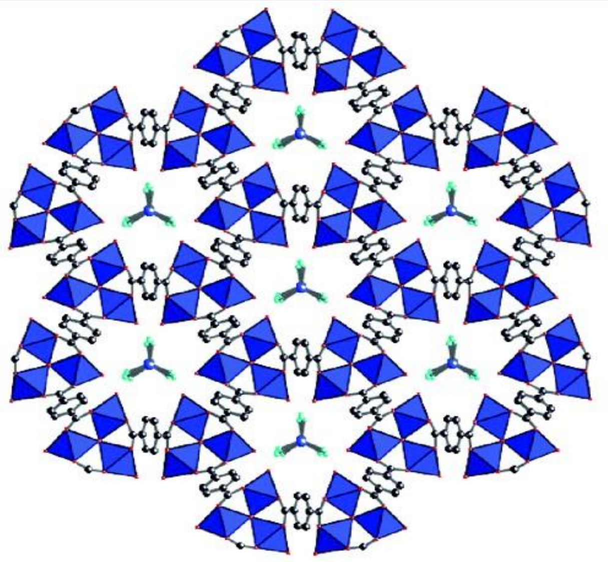

Figure 1.8 Single crystal X-ray structure of cationic MOF-235 composed of oxo-centered iron trimers connected by BDC ligands (Fe, blue; O, red; Cl, teal; C, gray).[55]

The use of N-donor ligands renders an effective strategy for the preparation of cationic MOFs as they typically do not contribute to the overall charge of the structure, thus allowing for the cationic charge from the metal center or SBU to prevail. An overall cationic structure in the MOF can be counterbalanced by weakly coordinating anions residing in the channels that can be exchanged for pollutant anionic species. Pyridine-based ligands are excellent candidates due to their structural rigidity that allows for the linker to remain intact throughout the synthesis, and thus facilitating the reticular design of a framework. Further, pyridine-based ligands can introduce various topologies to the framework based on their geometry and denticity or number of N-donor groups (Figure 1.9). The use of 4,4'-bipy (a) has been widely explored due its rod-like rigidity and length, typically forming 1-D polymeric chain structures even in the presence of water.[56] The trigonal geometry of tpt (b) can form 2-D polymers, and is known to give rise to unique topologies including nanocages, chambers and channels;[57] while hexamethylenetetramine (c) renders 3-D honeycomb structures due its tetrahedral arrangement of the N-donor sites.[58]

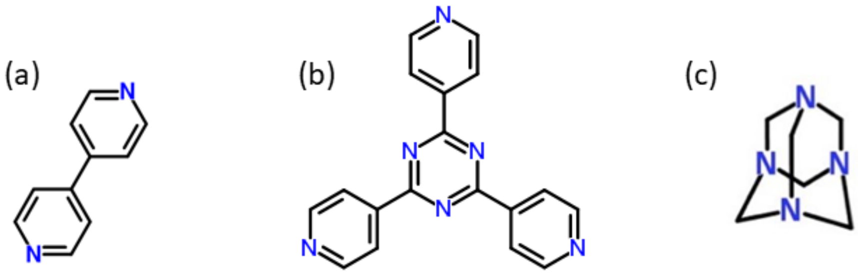

Figure 1.9 Examples of N-donor ligands widely used for the synthesis of MOFs: (a) 4,4'-bipyridine (bipy); (b) 2,4,5-tri(pyridyl)-1,3,5-triazine (tpt); (c) hexamethylenetetramine (hmt).

1.5.2.3 Anions

In order to design a cationic MOF, the role of the anions present in the structure must be carefully taken into account. In addition to counterbalancing the framework, the anions present in a crystal structure can have several structural roles as outlined in the work of Custelcean (Figure 1.10a):[59] (1) Anions can simply be spectators when these are only weakly interacting by Coulombic interactions, which is ideal in order to perform anion exchange without compromising the framework. (2) In the case where anions play a decisive role templating the formation of a particular structure without necessarily participating directly in the framework to as structure-directing agents (SDA). (3) Anions can also directly participate as structural components of the framework through the formation of well-defined interactions such as Lewis acid-base interactions. (4) Lastly, the anion can form part of the secondary building unit when it is a central component of a larger aggregate that plays the role of building block in the framework. It is worth noticing that anions can play more than one role when present in a framework, as in the case of a cationic Ag(I)-bipy coordination polymer designed by our group in which the anion, ethanedisulfonate (EDS), it is not only counterbalancing the 1D polymeric chains, but it is also serving as a structure directing agent. As seen in Figure 1.10b, an oxygen at each end of the EDS anion is interacting electrostatically with the Ag(I) as confirmed by the long Ag-O distances of 2.711(7) and 2.759(9) Angstroms, which exceed the covalent range.[60]

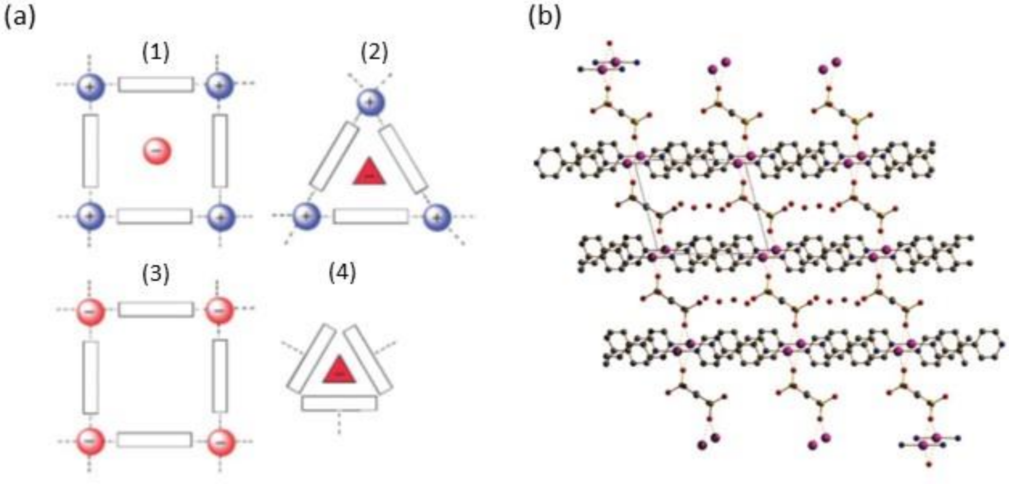

Figure 1.10. (a) Different structural roles of anions in crystals: (1) spectator; (2) structure directing agent; (3) building unit; (4) SBU component. (b) Crystallographic *a*-projection of cationic coordination polymer SLUG-21.[59,60]

1.5.3 Anion separation

As mentioned above, cationic MOFs tend to have spectator anions that interact weakly with their framework, making these excellent candidates for anion separation due to their ability to exchange these anions from their pores and/or channels with anions from solution without destruction of the framework. The ion exchanging capability of these crystalline materials has led to an extensive list of potential applications including reversible solvent inclusion, molecular sieving, catalysis, drug delivery, and chemical sensing technologies.[61] In particular, the application of cationic MOFs to remediate toxic anions in water is very attractive due to the tunability of their structures and high stability in various chemical environments. However, in order to understand how can these extended crystalline structures can be implemented as pollutant trapping agents, the anion exchange mechanisms and selectivity principles need to be addressed.

The mechanisms by which MOFs can exchange host anions from those found in solution has been proposed to occur by two main hypotheses.[62] The first hypothesis suggest that the anion exchange is a solid state process in which the host anions of a MOF migrate out of the crystalline solid through the channels between the layers followed by the concurrent inclusion of the anions from solution in the crystalline framework. On the other hand, an alternative hypothesis suggests that the anion exchange process may occur by a solvent-mediated process requiring the initial dissolution of one crystalline phase and subsequent precipitation of another. In both cases, the principle of selectivity is fundamental as it will govern any chemical separation due the presence of multiple competing anions in a given matrix, such as polluted wastewater where a vast amount of competing anions are present at higher concentrations than that of the pollutant of interest. In addition to the interference caused by the presence of competing anions, another complication in the selective separation of ions lies in the solvation effects from the polarity of water molecules that often prevents or complicates the separation of a target anion. These solvation effects have been determined to follow a general trend proposed by Franz Hofmeister, which was based on the ability of different anions to precipitate egg-white globulin.[63] This trend was determined to be dictated by the anion’s Gibbs free energy of hydration (Table 1.3), which would later be referred to as the “Hofmeister series” based on the degree of extraction of a specific anion from water:

$$PO_4^{3-} < CO_3^{2-} < SO_4^{2-} < CrO_4^{2-} < F^- < Cl^- < NO_3^- < CF_3SO_3^- < TcO_4^- < ClO_4^- < Ph_4B^-$$

This trend suggests that as the hydration energy of the anion increases, the difficulty to separate this anion via exchange will increase accordingly due to the increasing hydration energy barrier. The Hofmeister series has been used as a reference from which anion exchanging materials can be compared and designed for the selective exchange of an anion of interest. For instance, LDHs have a high affinity for intercalating carbonate anions, which follows the reverse order of decreasing hydration energy; thus, showing anti-Hofmeister bias. On the other hand, materials such as coordination polymers or MOFs are known to exhibit normal Hofmeister bias since they possess the uptake strength of anions that follow the Hofmeister series in decreasing hydration energy. This is an advantageous property for the use of MOFs as pollutant trapping materials since several pollutant anions including perchlorate and pertechnetate are known to have lower hydration energies (Table 1.3). In addition to the hydration energy of the incoming anion, the stability of the resulting MOF can also influence the selectivity of the anion exchange, which is particularly relevant for anion exchange processes that occur via solvent-mediated recrystallizations.

Table 1.3 List of anions and their respective Gibbs free energy of hydration

Anion	$\Delta G_{Hyd}°$, kJ/mol
Ph_4B^-	42
ClO_4^-	-214
TcO_4^-	-251
I^-	-275
ClO_3^-	-287
CN^-	-305
NO_3^-	-306
OAc^-	-373
F^-	-472
CrO_4^{2-}	-958
SO_4^{2-}	-1090
CO_3^{2-}	-1315
PO_4^{3-}	-2773

1.5.4 Cationic MOFs as Pollutant Trapping Materials

Cationic MOFs offer a viable alternative platform for use as materials in wastewater remediation applications due to their structural versatility, robustness, and their ability to exchange host spectator anions for pollutant oxyanions. Although research on the use of MOFs in oxyanion wastewater remediation is still in its infancy, this area of research is quickly expanding as well as the need for high performance adsorbent materials. Indeed, the potential of MOFs as adsorbent materials has been investigated beyond their use as anion exchangers due to their ability to perform separation of organic contaminants by surface adsorption, sulfate encapsulation, complexation and extraction.[64] Nonetheless, the scope of the work presented in this thesis will mainly consist in perchlorate remediation by utilizing the anion exchanging properties of cationic MOFs.

Previously, our group has paved the way into the design of cationic MOFs that exhibit excellent uptake of toxic oxyanions with outstanding selectivity. As one of the most recent examples these materials consists of $[Zn_xCo_{1-x}(H_2O)_4(4,4'\text{-bipy})_2]^+$ clusters that π-π stack in 2D cationic layers, and exhibit a high chromate (CrO_4^{2-}) adsorption of 68.5 mg/g that can be exerted selectively in the presence 50-fold excess nitrate and sulfate as competing anions.[65] Recently, other groups have successfully designed cationic MOFs that can capture hydrogen chromate ion ($HCrO_4^-$) reversibly up to one cycle by exchanging for nitrate found the hydrophobic cages of a silver-triazolato framework $[Ag_8(tz)_6](NO_3)_2$ in accordance to the Hofmeister bias (Figure 1.11).[66] Although much effort has been tailored towards remediation of chromate, arsenate, and pertechnetate, similar methodologies can be employed using cationic MOFs for the sustainable remediation of emerging perchlorate pollution.

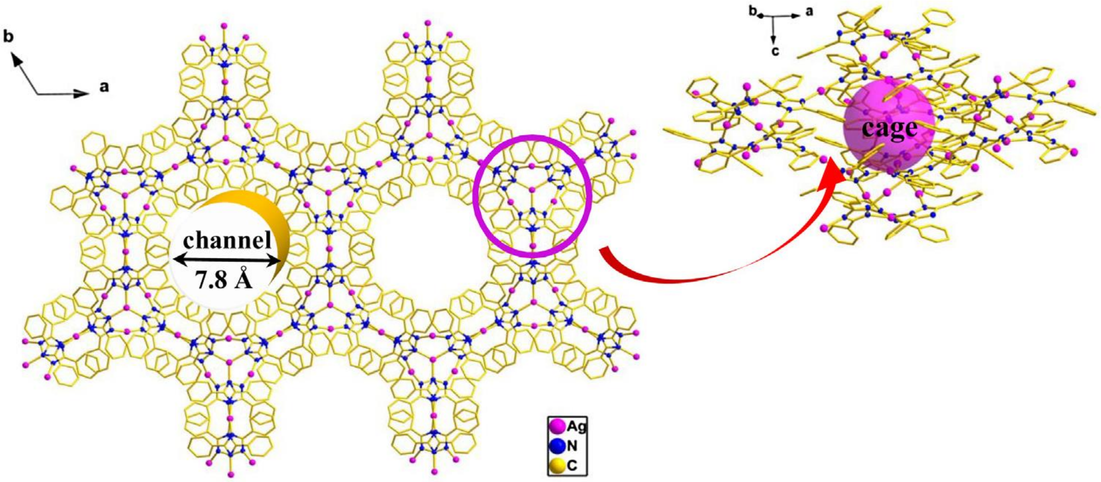

Figure 1.11. Hydrophobic cages (shown as lavender spheres) and cationic 1D channels suitable for anion exchange found in $[Ag_8(tz)_6](NO_3)_2$.[66]

1.6 Concluding Remarks

Cationic MOFs are a class of positively charged materials with great potential for environmental remediation applications. These crystalline materials exhibit a wide variety of topologies and dimensionalities that can be tailored for the capture of specific oxyanion pollutants as they undergo equilibrium-driven anion exchange processes, which can be engineered by accounting for the hydration energies of the respective anions. Unlike conventional ion exchanging materials (layered double hydroxides, ion exchange resins, zeolites), MOFs retain heterogeneity while performing selective and reversible anion exchange. Although their application in the selective capture of pollutants remains in an early stage, these upcoming materials have been widely investigated for their potential industrial use in gas storage, heterogeneous catalysis, sensing, and drug delivery. Insight on the strategy to design new cationic MOFs that can exchange host spectator anions by toxic anions found in solution has been highlighted in this chapter, along with the hypotheses of a potential solid-state *versus* solvent-mediated anion exchange process. The following chapters will describe the methodologies that have been developed for the capture of perchlorate from water by considering factors such as hydration energies of respective anions, stability of resulting frameworks, recyclability of material, and thorough characterization methods to assess the performance of anion-exchanging MOF materials.

1.7 References

(1) Water for the world: Water facts http://waterfortheworld.net/index.php?id=12 (accessed Sep 22, 2017).

(2) Grey, D.; Garrick, D.; Blackmore, D.; Kelman, J.; Muller, M.; Sadoff, C. Water Security in One Blue Planet: Twenty-First Century Policy Challenges for Science. *Philos. Trans. R. Soc. Math. Phys. Eng. Sci.* **2013**, *371* (2002), 20120406–20120406.

(3) Ying, Y.; Ying, W.; Li, Q.; Meng, D.; Ren, G.; Yan, R.; Peng, X. Recent Advances of Nanomaterial-Based Membrane for Water Purification. *Appl. Mater. Today* **2017**, *7*, 144–158.

(4) US EPA, O. Industrial Wastewater https://www.epa.gov/npdes/industrial-wastewater (accessed Sep 22, 2017).

(5) Ahmed, M. J. K.; Ahmaruzzaman, M. A Review on Potential Usage of Industrial Waste Materials for Binding Heavy Metal Ions from Aqueous Solutions. *J. Water Process Eng.* **2016**, *10*, 39–47.

(6) Varshney, G.; Kanel, S. R.; Kempisty, D. M.; Varshney, V.; Agrawal, A.; Sahle-Demessie, E.; Varma, R. S.; Nadagouda, M. N. Nanoscale TiO2 Films and Their Application in Remediation of Organic Pollutants. *Coord. Chem. Rev.* **2016**, *306*, 43–64.

(7) Montes-Hernandez, G.; Concha-Lozano, N.; Renard, F.; Quirico, E. Removal of Oxyanions from Synthetic Wastewater via Carbonation Process of Calcium Hydroxide: Applied and Fundamental Aspects. *J. Hazard. Mater.* **2009**, *166* (2–3), 788–795.

(8) Adeleye, A. S.; Conway, J. R.; Garner, K.; Huang, Y.; Su, Y.; Keller, A. A. Engineered Nanomaterials for Water Treatment and Remediation: Costs, Benefits, and Applicability. *Chem. Eng. J.* **2016**, *286*, 640–662.

(9) Srinivasan, A.; Viraraghavan, T. Perchlorate: Health Effects and Technologies for Its Removal from Water Resources. *Int. J. Environ. Res. Public. Health* **2009**, *6* (4), 1418–1442.

(10) Rüdel, H.; Díaz Muñiz, C.; Garelick, H.; Kandile, N. G.; Miller, B. W.; Pantoja Munoz, L.; Peijnenburg, W. J. G. M.; Purchase, D.; Shevah, Y.; van Sprang, P.; Vijver, M.; Vink, J. P. M. Consideration of the Bioavailability of Metal/Metalloid Species in Freshwaters: Experiences Regarding the Implementation of Biotic Ligand Model-Based Approaches in Risk Assessment Frameworks. *Environ. Sci. Pollut. Res.* **2015**, *22* (10), 7405–7421.

(11) ATSDR - Toxicological Profile: Chromium https://www.atsdr.cdc.gov/toxprofiles/TP.asp?id=62&tid=17 (accessed Nov 10, 2017).

(12) Costa, M. Potential Hazards of Hexavalent Chromate in Our Drinking Water. *Toxicol. Appl. Pharmacol.* **2003**, *188* (1), 1–5.

(13) Bagchi, D. Cytotoxicity and Oxidative Mechanisms of Different Forms of Chromium.

(14) Argos, M.; Kalra, T.; Rathouz, P. J.; Chen, Y.; Pierce, B.; Parvez, F.; Islam, T.; Ahmed, A.; Rakibuz-Zaman, M.; Hasan, R.; Sarwar, G.; Slavkovich, V.; van Geen, A.; Graziano, J.; Ahsan, H. Arsenic Exposure from Drinking Water, and All-Cause and Chronic-Disease Mortalities in Bangladesh (HEALS): A Prospective Cohort Study. *The Lancet* **2010**, *376* (9737), 252–258.

(15) Hughes, M. F. Arsenic Toxicity and Potential Mechanisms of Action. *Toxicol. Lett.* **2002**, *133* (1), 1–16.

(16) Gu, B.; Brown, G. M.; Bonnesen, P. V.; Liang, L.; Moyer, B. A.; Ober, R.; Alexandratos, S. D. Development of Novel Bifunctional Anion-Exchange Resins with Improved Selectivity for Pertechnetate Sorption from Contaminated Groundwater. *Environ. Sci. Technol.* **2000**, *34* (6), 1075–1080.

(17) Garten, C. T. Technetium-99 Cycling in Deciduous Forests: Review and Ecosystem Model Development. *Environ. Int.* **1987**, *13* (4–5), 311–321.

(18) Yang, Y.; Gao, N.; Chu, W.; Zhang, Y.; Ma, Y. Adsorption of Perchlorate from Aqueous Solution by the Calcination Product of Mg/(Al–Fe) Hydrotalcite-like Compounds. *J. Hazard. Mater.* **2012**, *209–210*, 318–325.

(19) Urbansky, E. T. Perchlorate as an Environmental Contaminant. *Environ. Sci. Pollut. Res.* **2002**, *9* (3), 187–192.

(20) Urbansky, E. T. Perchlorate Chemistry: Implications for Analysis and Remediation. *Bioremediation J.* **1998**, *2* (2), 81–95.

(21) Hautman, D. P.; Munch, D. J. *Determination of Perchlorate in Drinking Water Using Ion Chromatography.*; 1999.

(22) Motzer, W. Perchlorate: Problems, Detection, and Solutions. *Environ. Forensics* **2001**, *2* (4), 301–311.

(23) Capen, C. C. Mechanistic Data and Risk Assessment of Selected Toxic End Points of the Thyroid Gland. *Toxicol. Pathol.* **1997**, *25* (1), 39–48.

(24) Helfferich, F. G. *Ion Exchange*; Courier Corporation, 1962.

(25) Mark, R.; Findley, W. N. Thermal Expansion Instability and Creep in Amine-Cured Epoxy Resins. *Polym. Eng. Sci.* **1978**, *18* (1), 6–15.

(26) Gu, B.; Coates, J. D. *Perchlorate: Environmental Occurrence, Interactions and Treatment*; Springer Science & Business Media, 2006.

(27) Gu, B.; Brown, G. M.; Chiang, C.-C. Treatment of Perchlorate-Contaminated Groundwater Using Highly Selective, Regenerable Ion-Exchange Technologies. *Environ. Sci. Technol.* **2007**, *41* (17), 6277–6282.

(28) Batista, J. R.; Gingras, T. M.; Vieira, A. R. Combining Ion-exchange (IX) Technology and Biological Reduction for Perchlorate Removal. *Remediat. J.* **2002**, *13* (1), 21–38.

(29) Gu, B.; Brown, G. M. Recent Advances in Ion Exchange for Perchlorate Treatment, Recovery and Destruction. *Perchlorate* **2006**, 209–251.

(30) Neagu, V.; Bunia, I.; Plesca, I. Ionic Polymers VI. Chemical Stability of Strong Base Anion Exchangers in Aggressive Media. *Polym. Degrad. Stab.* **2000**, *70* (3), 463–468.

(31) Na, C.; Cannon, F. S.; Hagerup, B. Perchlorate Removal via Iron-Preloaded GAC and Borohydride Regeneration. *Am. Water Works Assoc. J.* **2002**, *94* (11), 90.

(32) Chen, W.; Cannon, F. S.; Rangel-Mendez, J. R. Ammonia-Tailoring of GAC to Enhance Perchlorate Removal. I: Characterization of NH 3 Thermally Tailored GACs. *Carbon* **2005**, *43* (3), 573–580.

(33) Ma, Y.; Tong, W.; Zhou, H.; Suib, S. L. A Review of Zeolite-like Porous Materials. *Microporous Mesoporous Mater.* **2000**, *37* (1), 243–252

(34) Caputo, D.; Pepe, F. Experiments and Data Processing of Ion Exchange Equilibria Involving Italian Natural Zeolites: A Review. *Microporous Mesoporous Mater.* **2007**, *105* (3), 222–231.

(35) Bowman, R. S. Applications of Surfactant-Modified Zeolites to Environmental Remediation. *Microporous Mesoporous Mater.* **2003**, *61* (1), 43–56.

(36) Bowman, R. S.; Haggerty, G. M.; Huddleston, R. G.; Neel, D.; Flynn, M. M. Sorption of Nonpolar Organic Compounds, Inorganic Cations, and Inorganic Oxyanions by Surfactant-Modified Zeolites; ACS Publications, 1995.

(37) Wang, Q.; O'Hare, D. Recent Advances in the Synthesis and Application of Layered Double Hydroxide (LDH) Nanosheets. *Chem. Rev.* **2012**, *112* (7), 4124–4155.

(38) Goh, K.-H.; Lim, T.-T.; Dong, Z. Application of Layered Double Hydroxides for Removal of Oxyanions: A Review. *Water Res.* **2008**, *42* (6–7), 1343–1368.

(39) He, J.; Wei, M.; Li, B.; Kang, Y.; Evans, D. G.; Duan, X. Preparation of Layered Double Hydroxides. In *Layered double hydroxides*; Springer, 2006; pp 89–119.

(40) Morel-Desrosiers, N.; Pisson, J.; Israëli, Y.; Taviot-Guého, C.; Besse, J.-P.; Morel, J.-P. Intercalation of Dicarboxylate Anions into a Zn–Al–Cl Layered Double Hydroxide: Microcalorimetric Determination of the Enthalpies of Anion Exchange. *J. Mater. Chem.* **2003**, *13* (10), 2582–2585.

(41) Arai, Y.; Ogawa, M. Preparation of Co–Al Layered Double Hydroxides by the Hydrothermal Urea Method for Controlled Particle Size. *Appl. Clay Sci.* **2009**, *42* (3), 601–604.

(42) Newman, S. P.; Jones, W. Synthesis, Characterization and Applications of Layered Double Hydroxides Containing Organic Guests. *New J. Chem.* **1998**, *22* (2), 105–115.

(43) Cavani, F.; Trifirò, F.; Vaccari, A. Hydrotalcite-Type Anionic Clays: Preparation, Properties and Applications. *Catal. Today* **1991**, *11* (2), 173–301.

(44) Liu, Z.; Ma, R.; Osada, M.; Iyi, N.; Ebina, Y.; Takada, K.; Sasaki, T. Synthesis, Anion Exchange, and Delamination of Co− Al Layered Double Hydroxide: Assembly of the Exfoliated Nanosheet/Polyanion Composite Films and Magneto-Optical Studies. *J. Am. Chem. Soc.* **2006**, *128* (14), 4872–4880.

(45) Wong, F.; Buchheit, R. G. Utilizing the Structural Memory Effect of Layered Double Hydroxides for Sensing Water Uptake in Organic Coatings. *Prog. Org. Coat.* **2004**, *51* (2), 91–102.

(46) Lin, Y.; Fang, Q.; Chen, B. Perchlorate Uptake and Molecular Mechanisms by Magnesium/Aluminum Carbonate Layered Double Hydroxides and the Calcined Layered Double Hydroxides. *Chem. Eng. J.* **2014**, *237*, 38–46.

(47) Wu, X.; Wang, Y.; Xu, L.; Lv, L. Removal of Perchlorate Contaminants by Calcined Zn/Al Layered Double Hydroxides: Equilibrium, Kinetics, and Column Studies. *Desalination* **2010**, *256* (1), 136–140.

(48) Miyata, S. Anion-Exchange Properties of Hydrotalcite-like Compounds. *Clays Clay Min.* **1983**, *31* (4), 305–311.

(49) Sumida, K.; Rogow, D. L.; Mason, J. A.; McDonald, T. M.; Bloch, E. D.; Herm, Z. R.; Bae, T.-H.; Long, J. R. Carbon Dioxide Capture in Metal–Organic Frameworks. *Chem. Rev.* **2012**, *112* (2), 724–781.

(50) Lee, J.; Farha, O. K.; Roberts, J.; Scheidt, K. A.; Nguyen, S. T.; Hupp, J. T. Metal–organic Framework Materials as Catalysts. *Chem. Soc. Rev.* **2009**, *38* (5), 1450–1459.

(51) Kreno, L. E.; Leong, K.; Farha, O. K.; Allendorf, M.; Van Duyne, R. P.; Hupp, J. T. Metal–organic Framework Materials as Chemical Sensors. *Chem Rev* **2012**, *112* (2), 1105–1125.

(52) Long, J. R.; Yaghi, O. M. The Pervasive Chemistry of Metal–organic Frameworks. *Chem. Soc. Rev.* **2009**, *38* (5), 1213.

(53) Dey, C.; Kundu, T.; Biswal, B. P.; Mallick, A.; Banerjee, R. Crystalline Metal-Organic Frameworks (MOFs): Synthesis, Structure and Function. *Acta Crystallogr. Sect. B Struct. Sci. Cryst. Eng. Mater.* **2014**, *70* (1), 3–10.

(54) Yaghi, O. M.; O'keeffe, M.; Ockwig, N. W.; Chae, H. K.; Eddaoudi, M.; Kim, J. Reticular Synthesis and the Design of New Materials. *Nature* **2003**, *423* (6941), 705–714.

(55) Sudik, A. C.; Côté, A. P.; Yaghi, O. M. Metal-Organic Frameworks Based on Trigonal Prismatic Building Blocks and the New “Acs” Topology. *Inorg. Chem.* **2005**, *44* (9), 2998–3000.

(56) Lu, J.; Paliwala, T.; Lim, S. C.; Yu, C.; Niu, T.; Jacobson, A. J. Coordination Polymers of Co(NCS) 2 with Pyrazine and 4,4‘-Bipyridine: Syntheses and Structures. *Inorg. Chem.* **1997**, *36* (5), 923–929.

(57) Li, M.-X.; Miao, Z.-X.; Shao, M.; Liang, S.-W.; Zhu, S.-R. Metal-Organic Frameworks Constructed from 2, 4, 6-Tris (4-Pyridyl)-1, 3, 5-Triazine. *Inorg. Chem.* **2008**, *47* (11), 4481–4489.

(58) Liu, C.-S.; Chang, Z.; Wang, J.-J.; Yan, L.-F.; Bu, X.-H.; Batten, S. R. A Photoluminescent 3D Silver (I) Coordination Polymer with Mixed Ligands Anthracene-9, 10-Dicarboxylate and Hexamethylenetetramine, Showing Binodal 4-Connected (4 3· 6 3) 2 (4 2· 6 2· 8 2) 3 Topology. *Inorg. Chem. Commun.* **2008**, *11* (8), 889–892.

(59) Custelcean, R. Anions in Crystal Engineering. *Chem. Soc. Rev.* **2010**, *39* (10), 3675.

(60) Fei, H.; Bresler, M. R.; Oliver, S. R. J. A New Paradigm for Anion Trapping in High Capacity and Selectivity: Crystal-to-Crystal Transformation of Cationic Materials. *J. Am. Chem. Soc.* **2011**, *133* (29), 11110–11113.

(61) Thompson, C.; Champness, N. R.; Khlobystov, A. N.; Roberts, C. J.; Schroder, M.; Tendler, S. J. B.; Wilkinson, M. J. Using Microscopic Techniques to Reveal the Mechanism of Anion Exchange in Crystalline Co-Ordination Polymers. *J. Microsc.* **2004**, *214* (3), 261–271.

(62) Khlobystov, A. N.; Champness, N. R.; Roberts, C. J.; Tendler, S. J.; Thompson, C.; Schröder, M. Anion Exchange in Co-Ordination Polymers: A Solid-State or a Solvent-Mediated Process? *CrystEngComm* **2002**, *4* (71), 426–431.

(63) Custelcean, R.; Moyer, B. A. Anion Separation with Metal–Organic Frameworks. *Eur. J. Inorg. Chem.* **2007**, *2007* (10), 1321–1340.

(64) Howarth, A. J.; Liu, Y.; Hupp, J. T.; Farha, O. K. Metal–organic Frameworks for Applications in Remediation of Oxyanion/Cation-Contaminated Water. *CrystEngComm* **2015**, *17* (38), 7245–7253.

(65) Fei, H.; Han, C. S.; Robins, J. C.; Oliver, S. R. J. A Cationic Metal–Organic Solid Solution Based on Co(II) and Zn(II) for Chromate Trapping. *Chem. Mater.* **2013**, *25* (5), 647–652.

(66) Li, L.-L.; Feng, X.-Q.; Han, R.-P.; Zang, S.-Q.; Yang, G. Cr (VI) Removal via Anion Exchange on a Silver-Triazolate MOF. *J. Hazard. Mater.* **2017**, *321*, 622–628.

Chapter 2

Reversible, Selective Trapping of Perchlorate from Water by a Cationic Metal-Organic Framework

Abstract

The capture of ppm level aqueous perchlorate in high capacity and fast kinetics *via* the complete anion exchange of a cationic metal–organic framework is reported. Ambient conditions were used for both the synthesis of silver 4,4’-bipyridine nitrate (SBN) and the exchange, forming silver 4,4’-bipyridine perchlorate (SBP). The exchange was complete within 90 minutes and the capacity was 354 mg/g, representing 99% removal. These values are greater than current anion exchangers such as the resins Amberlite IRA-400 (249 mg/g) and Purolite A530E (104 mg/g), as well as layered double hydroxides (28 mg/g). Moreover, unlike resins and layered double hydroxides, SBN is fully reusable and displays 96% regeneration to SBN in nitrate solution, with new crystal formation allowing indefinite cycling for perchlorate. We show seven cycles as proof of concept. Perchlorate contamination of water represents a serious health threat because it is a thyroid endocrine disruptor. This non-complexing anionic pollutant is significantly mobile and environmentally persistent. Removal of other anionic pollutants from water such as chromate, pertechnetate or arsenate may be possible by this methodology.

2.1 Introduction

Perchlorate (ClO_4^-) is an emerging trace contaminant in ground water and has gained significant attention as it has become widespread in many countries including the United States, Japan, Korea, India, Germany and China.[1] Even at 1 ppb level, this anionic pollutant can block the uptake of iodide by the thyroid due to their equivalent charge and similar ionic radii. This blockage can disrupt the production of thyroid hormones and affect metabolism, possibly leading to hypothyroidism or mental retardation in fetuses and infants.[2] Perchlorate salt is used as the conventional solid oxidant in the industrial manufacture of rocket fuel, explosives, flares and fireworks. Bleach and nitrate fertilizers can also contain perchlorate, and the anion also occurs naturally in arid environments.[3]

Because of the high solubility and non-complexing nature of perchlorate, it is highly mobile in aqueous environments and strongly resistant to traditional wastewater treatment technologies.[4] The latter include adsorption, ion exchange, membrane filtration, catalytic reduction and biological remediation. Among these techniques, ion exchange resins are considered the most viable and efficient method.[5] These matrices consist of a divinylbenzene crosslinked polystyrene backbone with terminal quaternary ammonium cationic side groups that possess an exchangeable counter-anion.[6] These resins have been widely studied and optimized for the selective capture of perchlorate from groundwater, and significant effort has been directed towards increasing their regenerability.[7-8] They also have been used in the attempt of separating pollutant anions such as arsenate (AsO_4^{3-}).[9] These resins, however, are of limited thermal and chemical stability due to their organic polymeric nature. For example, approximately 15% of their ion exchange capacity is lost upon contact with water at 90 °C, and 64% and 57% of their ion exchange capacity in the presence of sodium hypochlorite and hydrogen peroxide, respectively.[10] A recent attempt to separate perchlorate from water using an organic resin was reported by Song *et al*.[11] It was observed that such resins are significantly sensitive to pH. A perchlorate adsorption capacity of 170.4 mg/g (1.713 meq/g) could only be obtained upon treatment with a resin bed depth of 3.4 cm in a solution with an adjusted pH of 7, and the resin could only be effectively regenerated *via* concentrated hydrochloric acid treatment.

Layered double hydroxides (LDHs) are an isostructural set of materials consisting of cationic brucite-type layers that are charge balanced by interlayer anions with the general formula $[M^{2+}_{1-x}M^{3+}_{x}(OH)_2]A^{n-}_{x/n}\cdot mH_2O$. They have been studied extensively as a possible alternative to anion exchange resins.[12] This group of cationic materials, however, has limited capacity as evidenced by adsorption titrations and isotherms. In a recent study, the nitrate form of Mg:Al LDH had a perchlorate adsorption capacity of only 1.959 mg/g (0.0197 meq/g).[13] In addition, selectivity of LDHs is low toward target anions due to the interfering effect of competing anions. Common anions such as carbonate, sulfate and chloride tend to de-intercalate some or all of the trapped anions.[14]

Metal-organic frameworks (MOFs, also known as coordination polymers) are an emerging class of materials with a now vast array of topologies and properties of interest including gas storage,[15] gas separation,[16] drug delivery[17] and ion exchange.[18] Cationic MOFs are a subgroup of these compounds, where positive metal centers are connected by neutral organic linkers and anions reside in the pores. If the host-guest interaction is weak, anion exchange may occur if the framework does not collapse in the process.[19] Feng *et al.* recently demonstrated a selective anion exchange separation process using a cationic indium-based MOF [$In_3O(COO)_6^+$]. The material reversibly captures organic dye anions of varying charge from a dimethylformamide (DMF) solution.[20] Custelcean and coworkers have developed an anion separation approach in aqueous systems by the selective crystallization of chloride, bromide or iodide into one-dimensional cationic MOFs, even in the presence of competing oxo-anions such as nitrate and sulfate. The anion selectivity is governed by the anion size, coordinating ability and the overall packing efficiency of the MOF.[21,22]

Ag(I) is an ideal metallic node for cationic MOF construction due to its high affinity for N- and O-donors and flexible coordination number and geometry of two to eight.[23] In fact, silver coordination polymers have been previously studied for their ability to selectively trap anions via single-crystal-to-single- crystal (SC-SC) transition.[24,25] Our group reported a cationic framework referred to as SLUG-21, which consists of chains of alternating Ag(I) and 4,4'-bipyridine that π-π stack into cationic layers. The layers are charge balanced by ethanedisulfonate (EDS) anions and selectively exchange for permanganate and perrhenate, with a significantly high adsorption capacity of 292 and 602 mg/g, respectively.[26] Nonetheless, reversibility in the uptake of oxyanions including perchlorate remained a challenge due to the lower affinity for alkylsulfonates.

Herein, we report the perchlorate trapping profile of the cationic MOF [Ag-bipy$^+$][NO_3^-] (silver 4,4'-bipyridine nitrate, SBN).[27] The material releases nitrate, an essential component of fertilizers whose maximum concentration level (MCL) in water is 10 ppm, in exchange for perchlorate: a highly toxic anion present in polluted groundwater at concentrations up to 5 ppm.[28] Hence, the exchange of nitrate for perchlorate would result in a concentration below the regulatory level, and such treated water could potentially be incorporated into irrigation systems. Unlike urea or ammonium, nitrate is immediately available as a nutrient that can be readily absorbed by plants in high rates and concentrations up to 100 mM, storing excess nitrate in the vacuole.[29] In addition, SBN traps perchlorate quantitatively in far greater capacity, selectivity, speed and reversibility compared to existing resins and LDHs, offering an alternative solution to the ongoing issue of perchlorate pollution.

2.2 Experimental Section

2.2.1 Reagents

Silver nitrate ($AgNO_3$, Fisher, 99%), 4,4'-bipyridine [$(C_5H_4N)_2$, Acros Organics, 98%], and 1,2-ethanedisulfonic acid ($HO_3SCH_2CH_2SO_3H$, TCI Inc. 95%) were used as-received for the synthesis. Sodium nitrate ($NaNO_3$, Fisher, 99%), sodium perchlorate monohydrate ($NaClO_4 \cdot H_2O$, Fluka Analytical, 98%), Purolite A530E (Purolite), Amberlite IRA-400 resin (Sigma-Aldrich) and hydrotalcite

[$Mg_6Al_2(CO_3)(OH)_{16}\cdot 4H_2O$, Aldrich Chemistry] were used as-purchased for the anion exchange reactions.

2.2.2 Synthesis

[Ag(4,4'-bipy)(NO$_3$)] (SBN)

Pale gray parallelepiped crystals of SBN 400 to 600 µm in length were synthesized hydrothermally (HT-SBN, Figure 2.1a). Alternatively, room temperature conditions (RT-SBN) yielded a microcrystalline powdered material consisting of 4 to 10 µm average sized blocks (Figure 2.1b). For HT-SBN, a mixture of $AgNO_3$ (0.1 g, 0.59 mmol), 4,4'-bipyridine (0.1 g, 0.64 mmol) and deionized water (10 mL) was stirred at room temperature for 10 min and then transferred to a 15 mL Teflon lined autoclave to 2/3 filling. The autoclave was placed in a programmable oven and heated at 140 °C for 10 h, then cooled to 110 °C for 8 h, followed by further cooling to 90 °C for 6 h and finally cooling to room temperature at a rate of 0.1 °C/min. Pale gray crystals were isolated after filtration and rinsed with water and acetone (yield: 0.181 g, 94.3% based on silver nitrate). The synthesis of RT-SBN crystals was carried out by simply stirring the reactants in the same ratio for 3 days in a sealed beaker and filtered in the same manner (yield: 0.187 g, 97.6% based on silver nitrate).

[Ag$_2$(4,4'-bipy)$_2$(O$_3$SCH$_2$CH$_2$SO$_3$)] (SLUG-21)

Colorless crystals of SLUG-21 were synthesized under hydrothermal conditions.[30] A reactant solution with a molar ratio of 1:1:1:400 for $AgNO_3$: EDSA : 4,4'-bipy : H_2O was stirred at room temperature for 10 min and then transferred to a

15 ml Teflon lined autoclave to 2/3 filling. The autoclaves were heated at 150 °C for 5 days under autogenous pressure.

2.2.3 Perchlorate Exchange

Batch experiments were carried out under ambient conditions by simply placing 80 mg (0.25 mmol) of as-synthesized SBN or 100 mg (0.125 mmol) of SLUG-21 material previously ground using a mortar and pestle into a beaker containing 50 mL deionized water and $NaClO_4$ (35 mg, 0.25 mmol). The anion exchange solution was sealed and stirred mildly. The exchange solution was analyzed by taking liquid aliquots at various time intervals to quantify the residual perchlorate concentration by IC. The post-exchange crystalline SBP product was recovered by vacuum filtration and rinsed with water and acetone prior analysis by powder X-ray diffraction (PXRD).

2.2.4 Selectivity Tests

Selectivity batch tests were performed by introducing 65.2 mg (0.2 mmol) of SBN material into a sealed beaker containing 50 ml H_2O and 42 mg (0.3 mmol) $NaClO_4$. The beaker also contained either 0.84 g (10 mmol) $NaHCO_3$ or 1.42 g (10 mmol) $NaSO_4$ (fifty-fold molar excess). The selectivity reactions were mildly stirred for 2 h under ambient conditions and the filtrate was analyzed quantitatively by ion chromatography (IC) to quantify the residual perchlorate concentration.

2.2.5 SBN Regeneration

Upon completion of ion exchange, the solid crystalline SBP material was placed into a 0.1 M $NaNO_3$ solution and mechanically stirred in an oil bath at 70 °C. The percent regeneration was evaluated by measuring the increase of perchlorate concentration in the regeneration solution *via* IC and by the PXRD peak area of the main (002) and (100) peak for SBN and SBP, respectively.

2.2.6 Characterization

PXRD was measured on a Rigaku Americas Miniflex Plus diffractometer, scanning from 2 to 40 ° (2θ) at a rate of 2 $°\cdot min^{-1}$ with a 0.04 ° step size under Cu Kα radiation ($\lambda = 1.5418$ Å). IC analysis was performed to assess perchlorate concentration using a Dionex ICS-3000 with an IonPac AS20 column and a detection limit of 3 µg/L (ppb). Scanning electron microscopy (SEM) data were collected with a FEI Quanta 3D Dualbeam microscope.

2.3 Results and Discussion

2.3.1 Synthesis and Structural Characterization of SBN

Crystals of SBN can be synthesized hydrothermally or at room temperatures. Hydrothermal conditions produced pale gray crystals of uniform size ranging from 400-600 µm with a parallelepiped morphology (Figure 2.1a). Room temperature synthesis of SBN resulted in a fine colorless microcrystalline powder (Figure 2.1b). Both synthetic methods result in highly crystalline materials stable in deionized water with yields of 94.3% and 97.6% for the hydrothermal and room temperature routes, respectively. PXRD confirms that both methods yield the identical phase and match the theoretical pattern based on the single crystal solution (Figure 2.2a,b).[27,31]

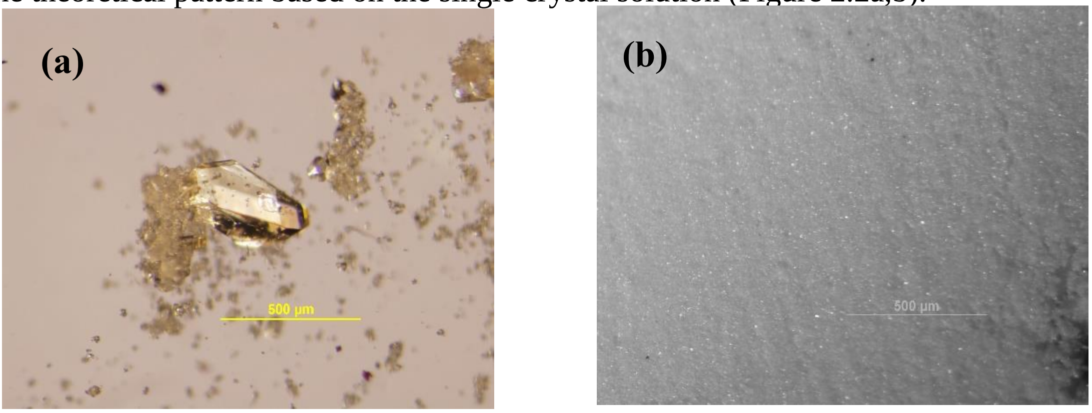

Figure 2.1 Optical micrographs: (a) hydrothermal SBN and (b) room temperature SBN.

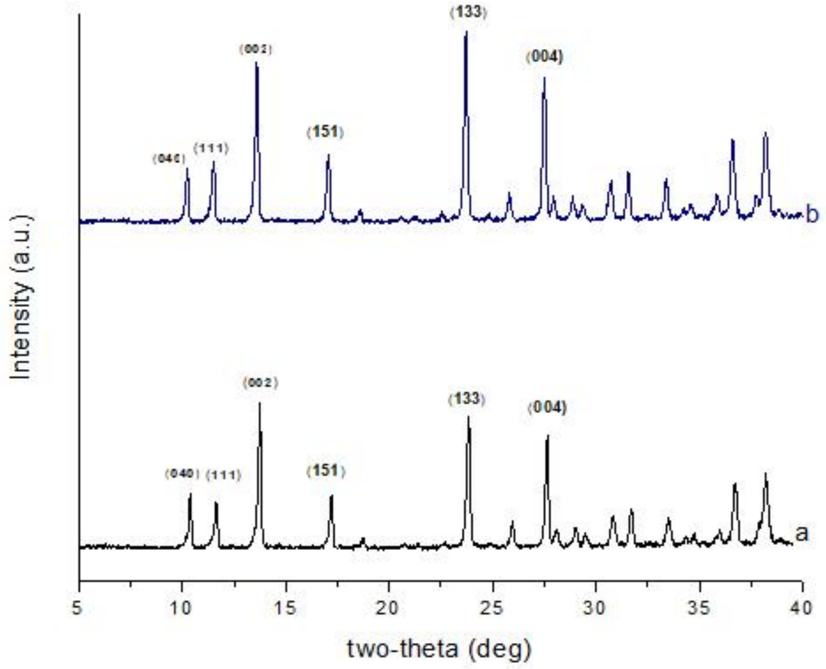

Figure 2.2 PXRD patterns: (a) room temperature SBN; (b) hydrothermal SBN.

The tendency of Ag(I) to form linear coordination polymers is demonstrated in the synthesis of SBN consisting in reaction of $AgNO_3$ with the rod-like 4,4'-bipy ligand, which affords a 3-D extended cationic framework with nitrate anions residing in the channels. Each Ag(I) is chelated to two nitrogens of different but symmetry equivalent 4,4'-bipy units resulting in extended polymeric chains that stagger by 90° to subsequent layers forming a criss-cross or T-shaped pattern (Figure 2.3). The thermal stability of the aforementioned framework was investigated by performing thermogravimetric analysis on a 11.25 mg sample (Figure 2.4). An abrupt weight loss of 67% corresponding to one 4,4'-bipy unit and one nitrate per formula unit (theoretical 67%) was observed at 302 °C, leaving behind metallic silver.

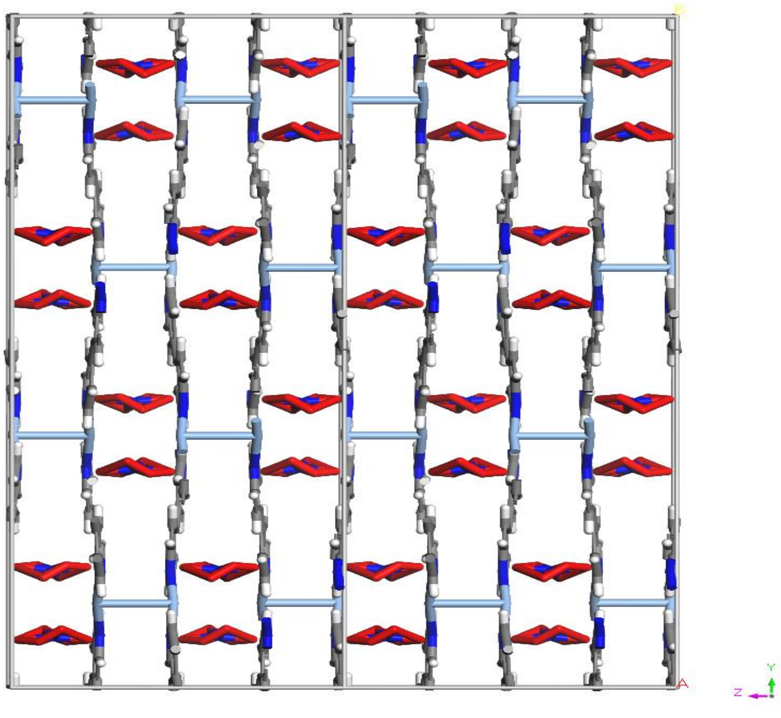

Figure 2.3 Crystallographic view of SBN with partially disordered nitrates included.

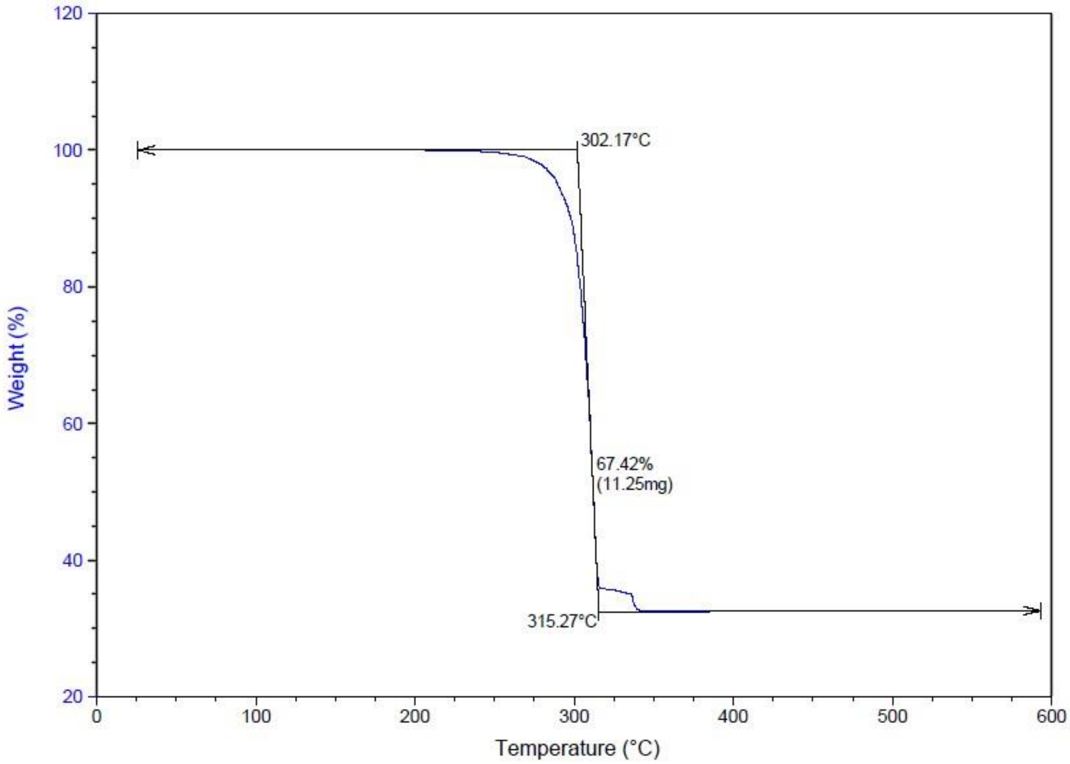

Figure 2.4 Thermogravimetric analysis of SBN in the range of 30 to 600 °C.

2.3.2 SLUG-21 Perchlorate Uptake

Preliminary investigations of perchlorate uptake were carried out utilizing a material previously designed by our group consisting of a cationic silver-based one-dimensional coordination polymer designated SLUG-21, which was studied for its ability to capture permanganate and perrhenate at high adsorption capacities.[26] As in the case of SBN, SLUG-21 is composed of cationic Ag(I)-bipy chains π-stacked between adjacent chains, but with ethanedisulfonate (EDS) anions residing in the interlamellar space (Figure 2.5).

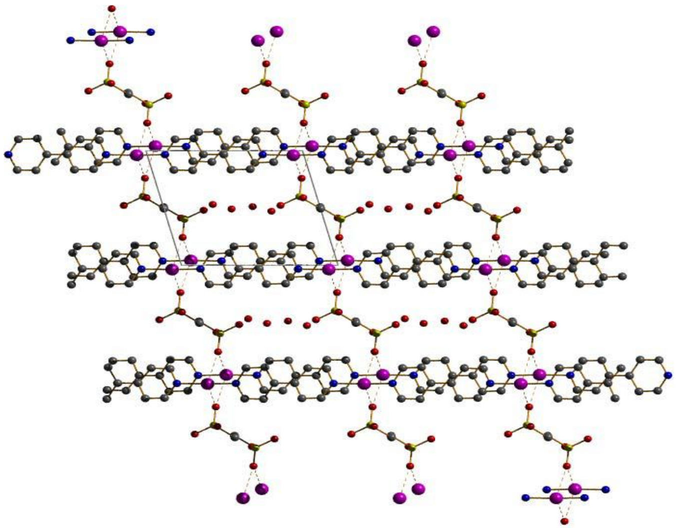

Figure 2.5 Crystallographic *a*-projection of SLUG-21 structure.[30]

As shown in Figure 2.5, only one oxygen atom from the EDS anions is weakly interacting with Ag(I) atom allowing for the exchange of this sulfonate anions for perchlorate. A series of batch tests were performed to evaluate the ability of this coordination polymer to exchange out its EDS for perchlorate in aqueous environments. The batch tests were carried out at various molar ratios with 1:2 of material to perchlorate being the most successful, suggesting that two perchlorate molecules are exchanged per each EDS anion. The as-synthesized SLUG-21 material was monitored by PXRD before and after anion exchange from which a new crystal phase was obtained upon 1 day of exposure to aqueous perchlorate (Figure 2.6). The anion exchange was quantified by measuring the residual perchlorate concentration utilizing ion chromatography, from which the adsorption capacity of SLUG-21 was determined to be 92 mg of ClO_4^- / gram of SLUG-21, representing a 68% perchlorate uptake.

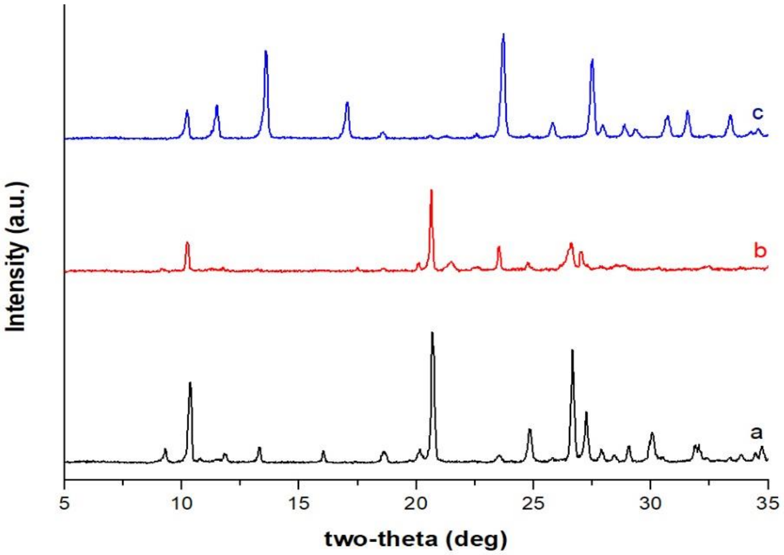

Figure 2.6 PXRD patterns: (a) as-synthesized SLUG-21; (b) SLUG-21[ClO_4^-]: solid product after 1 day of exposure to perchlorate; (c) SBN: product after treatment of SLUG-21[ClO_4^-] with 0.1 M $NaNO_3$ for 1 day.

In effort to regenerate the SLUG-21 material after anion exchange with perchlorate, the SLUG-21[ClO_4^-] solid was treated with a 0.1 M EDS solution at various time intervals. Unfortunately, the anion exchange between SLUG-21 and perchlorate was not reversible as a result of the higher stability of SLUG-21[ClO_4^-], as well as the lower hydration energy of perchlorate relative to that of EDS. Since the anion exchange between SLUG-21 and perchlorate could not be reversed, other anions including carbonate, nitrate, and sulfate were used to cycle between SLUG-21[ClO_4^-] and SLUG-21. It was found that SLUG-21[ClO_4^-] could slowly anion exchange with nitrate resulting in the formation of the SBN material discussed in section 2.3.1 (Figure 2.6c). SBN was found to be a better candidate due its higher perchlorate uptake, faster kinetics and ability to exchange anions reversibly with perchlorate (*vide infra*).

2.3.3 SBN Perchlorate Exchange

Considering that SBN has weakly bound nitrate anions between the cationic Ag(I)-bipy$^+$ that allow to reversibly exchange anions with perchlorate, this material was systematically studied by performing a series of batch tests to understand the kinetics of the exchange that would allow us to design a methodology for the sustainable capture of perchlorate from water. Initially, the perchlorate uptake of the as-synthesized SBN material was characterized by PXRD analysis of the solid product after exchange, which matched the theoretical pattern of SBP (Figure 2.7).[31] In addition, Figure 2.8 shows the FTIR of the as-synthesized SBN material and the solid product after exchanged corresponding to SBP. The four singlets bands at 1600 cm^{-1}, 1540 cm^{-1}, 1490 cm^{-1}, and 1420 cm^{-1} are aromatic C=C and C=N bending, confirming the presence of 4,4'-bipyridine in both structures. Upon completion of the anion exchange the sharp stretch corresponding to the NO_3^- group of SBN observed around 1330 cm^{-1} has disappeared, with a new strong broad band at 1100 cm^{-1} corresponding to the ClO_4^- in SBP.[32] This anion exchange reaction had been proposed to occur through a solvent-mediated recrystallization process as described by Schröder *et al.* for related metal bipyridine and pyrazine coordination polymers, which favors the capture of perchlorate as the solubility of SBN in water (0.80 mmol• L^{-1}) is much greater than that of SBP (0.19 mmol•L^{-1}).[33]

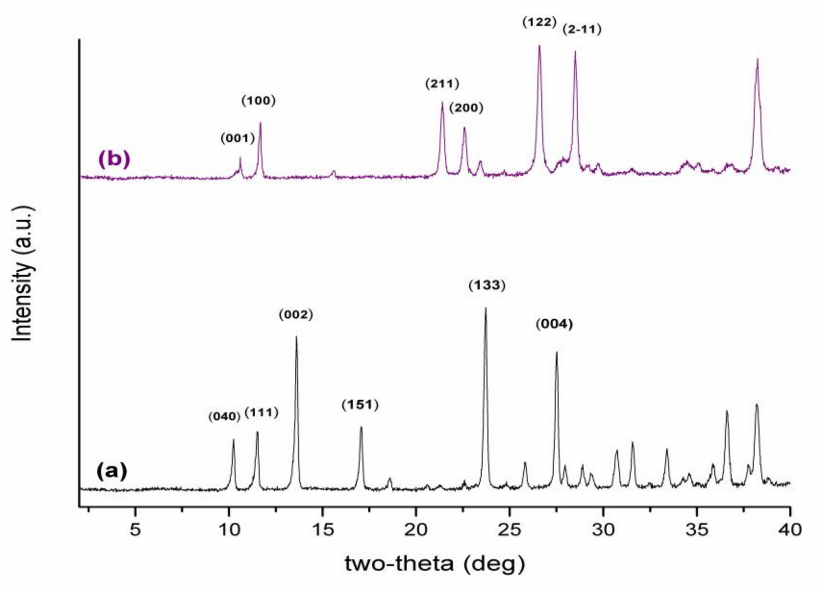

Figure 2.7 PXRD patterns of: (a) SBN; (b) SBP.

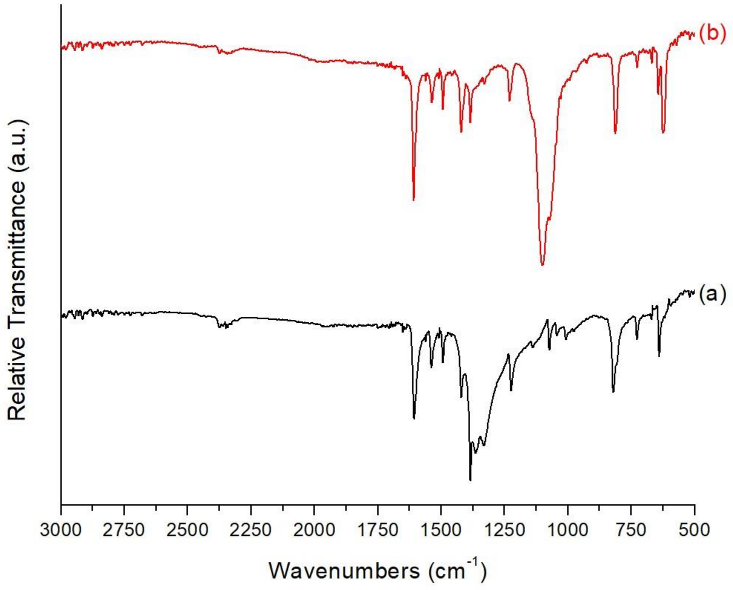

Figure 2.8 FTIR spectrum of: (a) SBN; (b) SBP.

The perchlorate uptake capacity of SBN was quantified by measuring the residual concentration of perchlorate after performing a 4h equimolar batch test using ion chromatography. The adsorption capacity of SBN was determined to be 354 mg of ClO_4^- / gram of SBN, representing a 99% perchlorate uptake. Once the adsorption capacity was determined, the anion exchange kinetics of both the hydrothermal and room temperature SBN were investigated by taking liquid aliquots at various time intervals. The results from this kinetic experiment shown in Figure 2.9 reveal that the SBN material prepared at room temperature exhibits faster kinetics than the hydrothermal product, possibly as a result of the higher surface area of the microcrystalline material compared to that of the larger crystals prepared under hydrothermal conditions.

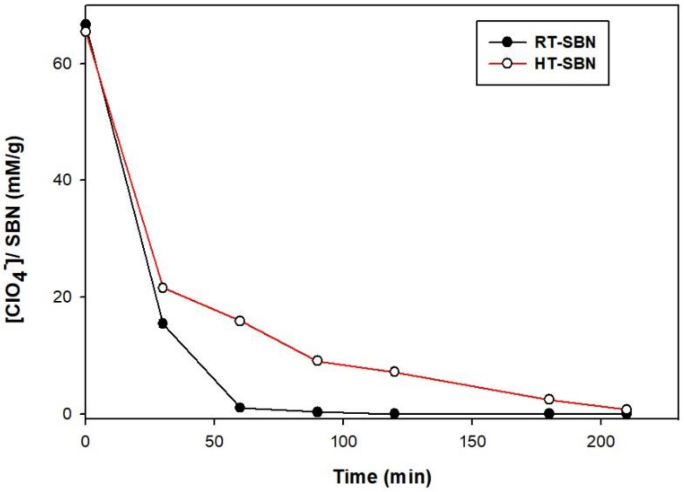

Figure 2.9 Perchlorate uptake kinetics of RT-SBN (black) and HT-SBN (red).

The uptake kinetics of SBN were compared to the performance of the commercially available anion exchange resin Amberlite IRA-400, as well as the calcined and uncalcined forms of hydrotalcite [$Mg_6Al_2(CO_3)(OH)_{16}\cdot4H_2O$] and Ni_3Al-LDH. The latter was tested because it adsorbs in higher capacity than hydrotalcite for some oxyanions including pertechnetate.[34] All batch experiments were performed under the same conditions using equivalent stoichiometric amounts of the anion exchanger. The kinetic plots underscore the superior performance of SBN (Figure 2.10). A rapid decrease of approximately 98% of the perchlorate concentration was observed within 60 min for SBN. This rapid perchlorate trapping can be further understood by considering the kinetics of the nitrate released by SBN (Figure 2.11), which reaches a plateau after 90 min corresponding to the stoichiometric amount of exchanged perchlorate into SBP. In the case of the other anion exchangers, only Amberlite showed a significant perchlorate uptake in 60 min, with 76% removed. After 90 min, the values were 100% for SBN and 78% for Amberlite. Both calcined hydrotalcite and Ni_3Al-LDH display a low perchlorate uptake of only 4 to 12%. This lower affinity for the LDHs is in part due to the fact that we did not exclude carbonate from the exchange solutions (always present from atmospheric CO_2). Carbonate is known to lower anion capacity for LDHs and is in fact used to regenerate exchanged LDH.[13] The meq/g adsorption capacities for each of the anion exchangers are summarized in Table 2.1.

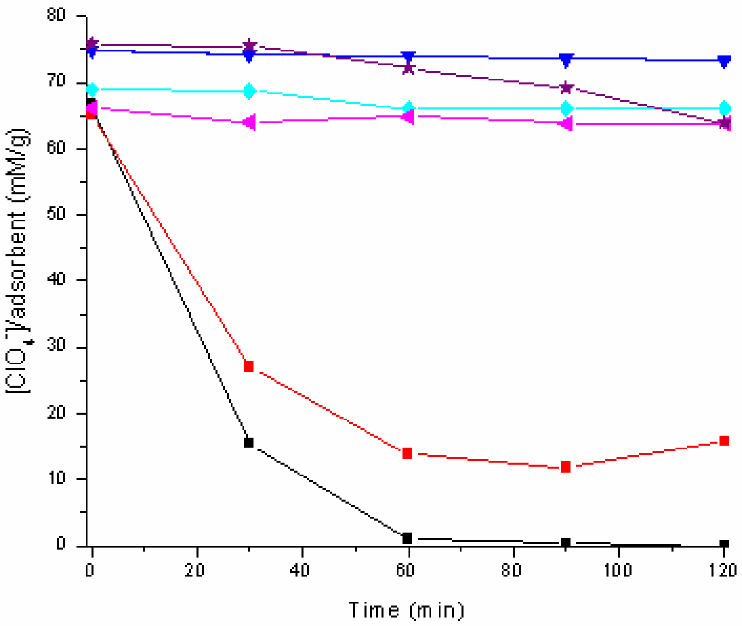

Figure 2.10 Perchlorate uptake per gram of solid versus time: SBN (black squares), Amberlite (red squares), uncalcined hydrotalcite (magenta triangles), calcined hydrotalcite (purple stars), uncalcined Ni_3Al-LDH (blue triangles) and calcined Ni_3Al-LDH (cyan diamonds).

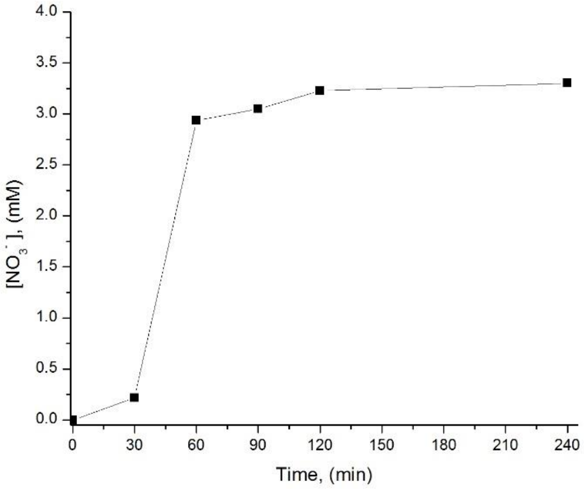

Figure 2.11 SBN nitrate release during stoichiometric anion exchange with perchlorate.

Table 2.1 Perchlorate exchange capacities of the various cationic host materials tested

Anion Exchanger	mg ClO_4^-/g	mol ClO_4^-/mol	meq/g	% ClO_4^- removal[a]
SBN	353.97	1.062	3.569	99%
Uncalcined Hydrotalcite-LDH	10.62	0.065	0.107	3.2%
Calcined Hydrotalcite-LDH	47.51	0.289	0.478	11%
Uncalcined Ni_3Al-LDH	5.85	0.048	0.059	1.6%
Calcined Ni_3Al-LDH	24.0	0.195	0.241	5.1%
Amberlite IRA-400 Resin	248.87	N/A	2.502	78%

[a] Based on the theoretical capacity of the starting solid.

In addition to the high adsorption capacity and ambient conditions for both the synthesis and exchange, SBN exhibits highly selective perchlorate capture in the presence of multiple-fold excess of potentially competing common anions. The issue of selectivity is an ongoing problem for LDHs due to the high affinity of the cationic layers for carbonate as well as other anions including sulfate, hydroxide and chloride.[15] The selectivity of SBN for perchlorate uptake over carbonate and sulfate was demonstrated by performing two separate batch tests containing 50-fold molar excess of each anion. In both tests it was found that the competing anions did not interfere with the uptake of perchlorate, likely due to both its lower relative hydration energy and lower solubility of the complex. The adsorption capacities remained at the high levels of 337 and 342 mg ClO_4^-/g SBN for the carbonate and sulfate batch tests, representing 95% and 97% perchlorate uptake, respectively.

2.3.4 SBN Regeneration Studies

For any industrial application, the recyclability of the anion exchanger is a critical issue. The material after anion exchange must be easily recoverable and retain its structure and particle size after multiple regeneration cycles. LDHs often form a gel and require *ca.* 30 min of centrifuging for total separation from solution, while resins require strong acid or brine and form a slurry. In contrast, SBP is highly crystalline after anion exchange and is easily separated from solution by vacuum filtration. In order for the MOF to reversibly exchange its anions by a solvent mediated process, it must have similar solubility for its original and exchanged forms.[33] The lower solubility of SBP must be overcome by increasing the nitrate to perchlorate concentration ratio as well increasing the temperature to shift the equilibrium and allow SBP to dissolve into its individual components and recrystallize back to SBN.

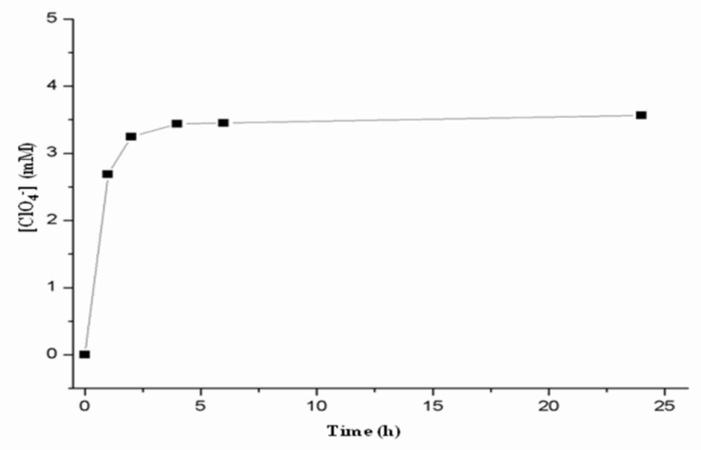

Figure 2.12 SBN regeneration: plot of perchlorate release from SBP versus time in 20-fold molar excess sodium nitrate solution.

Indeed, the solid can be quantitatively regenerated to phase-pure SBN simply by stirring in a 20-fold molar excess 0.1 M sodium nitrate salt solution at 70 °C for 24 h. The heat allowed for the coordination polymer to come apart, while the excess nitrate shifts the dynamic equilibrium allowing for the re-intercalation of such anion. The evolved perchlorate as determined by IC showed that the SBN material regenerated an average of 96% based on the stoichiometric amount of perchlorate initially exchanged by nitrate (Figure 2.12). This perchlorate-nitrate cycling shows continued excellent reversibility up to seven cycles shown as proof of concept (Figure 2.13) and IC data confirms complete exchange (Table 2.2). Although the regeneration kinetics of the subsequent cycles are slower due to a loss of crystallinity (Figure 2.14), new SBN crystals are formed upon regeneration, meaning fresh crystals are formed on each cycle for continued recyclability.

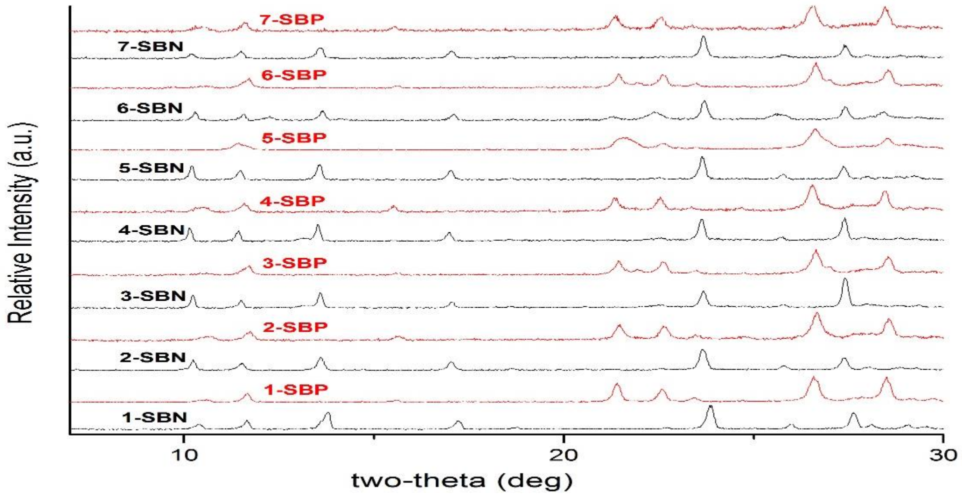

Figure 2.13 PXRD showing cyclability of [Ag-bipy$^+$] over seven cycles for proof of concept.

Table 2.2. Adsorption capacities of perchlorate trapping cycles by SBN

Cycle No.	**1st**	**2nd**	**3rd**	**4th**	**5th**	**6th**	**7th**
mol/mol	1.129	0.868	0.815	0.796	1.081	0.709	0.641
mg/g	344.36	264.93	248.63	243.05	329.86	216.35	195.59
meq/g	3.463	2.664	2.500	2.444	3.316	2.175	1.966

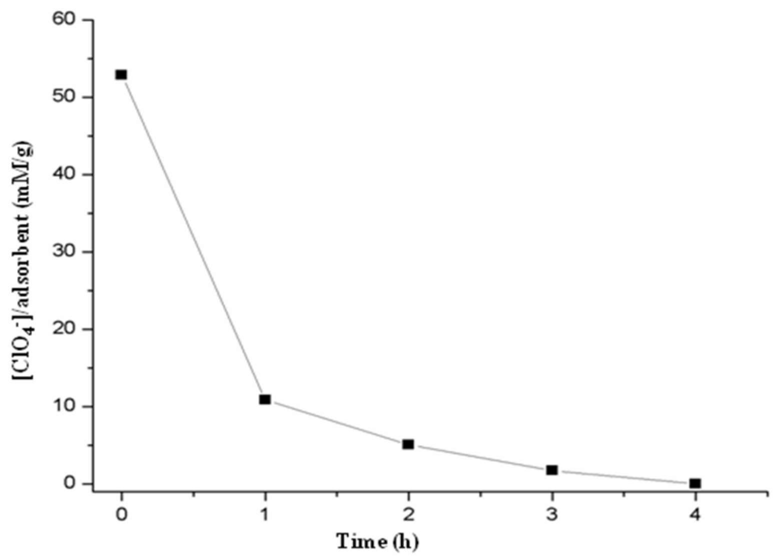

Figure 2.14 Second cycle perchlorate uptake per gram of SBN solid versus time.

The theoretical capacity per gram of material per cycle is 0.354 g of perchlorate, which would correspond to the ability to treat (for example) 17,700 L of 20 ppb perchlorate contaminated water. In the case of the Amberlite resin, its theoretical capacity per cycle of 0.249 g of perchlorate would treat only 12,400 L of 20 ppb contaminated water and require concentrated brine solutions or mineral acid treatment for each regeneration cycle. The superior performance and recyclability of SBN/SBP can be seen in a plot of the uptake capacity versus cycle number (Figure 2.15).

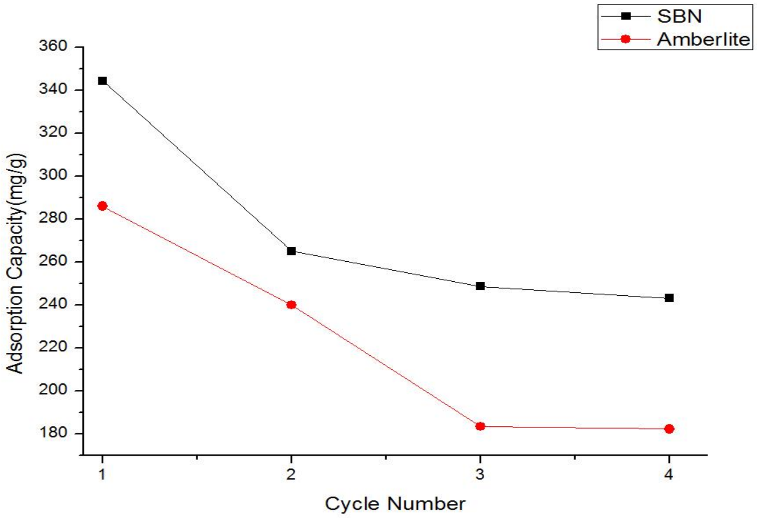

Figure 2.15 Plot of perchlorate uptake capacity versus cycle number.

In addition to these highly desirable exchange properties, the material must be able to capture the dilute perchlorate of wastewater. As an initial test of lower concentration, a 5 ppm perchlorate exchange was carried out using 60 mg of SBN, and the material exhibited a 100% perchlorate removal over 5 days (Figure 2.16). The perchlorate uptake is much faster rate and at a deeper level for our material compared to resins and LDHs. These features make it possible to use the material in a large stationary container, the common method for perchlorate treatment. Regeneration can then occur offline at room temperature in excess nitrate solution at 70 °C condition over the longer required time frame.

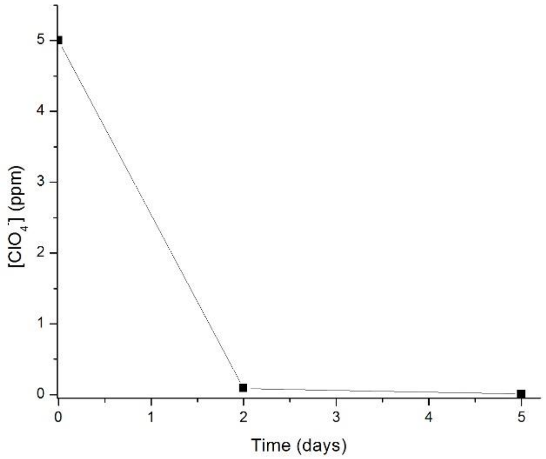

Figure 2.16 5 ppm perchlorate removal by SBN.

2.3.5 Structural Considerations of SBN/SBP Anion Exchange

The $[Ag\text{-}bipy^+]$ polymeric chains display greater preference for perchlorate than nitrate, allowing for the rapid trapping of ppm level perchlorate from contaminated water. The anion preference can be understood on the basis of the hydration energy of both anions, with perchlorate having a lower hydration energy (-214 kJ/mol) than nitrate (-306 kJ/mol) following the Hofmeister series.[19] Concurrently, such anion exchange reaction can be further elucidated by considering the SBN and SBP crystal structures (Figures 2.3, 2.17).

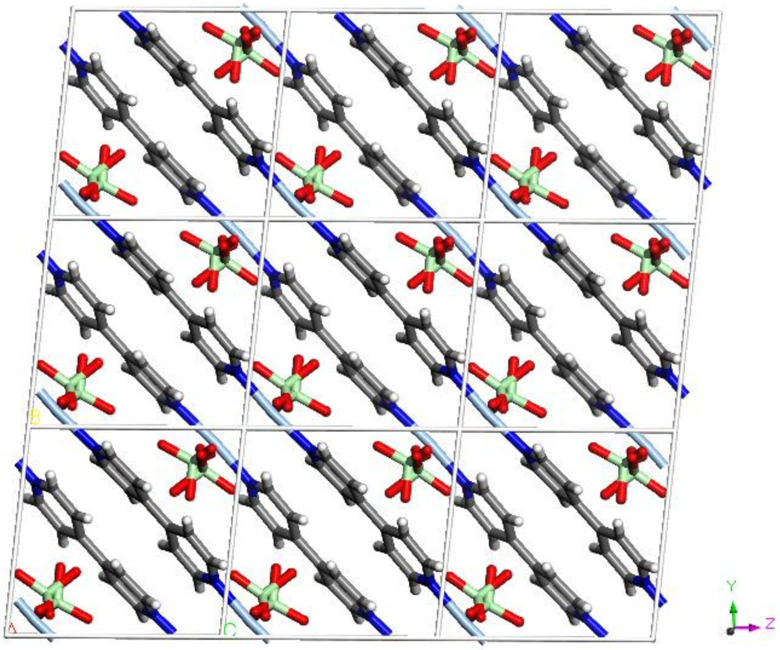

Figure 2.17 Crystallographic view of SBP with disordered perchlorates included.

For both SBN and SBP, each Ag(I) is chelated by the nitrogens of two different (μ-2)-4,4'-bipyridine units, forming extended polymeric chains. These chains align parallel into a non π-stacked "layer" where the rings are all co-planar with the plane of the page (red atoms, Figure 2.18). The two structures differ in the arrangement of the next "layer" (green atoms, Figure 2.18). For SBN, the next layer is rotated by 90° (Figure 2.18a) whereas for SBP the layers are eclipsed (Figure 2.18b). For SBN, only half of the pyridine rings π-stack in a staggered manner to the adjacent layer (Figure 2.18a, average distance 3.55 Å) whereas all pyridine rings π-stack and are eclipsed for SBP (Figure 2.18b, average distance 3.47 Å). For SBN, half of the silver centers dimerize [Ag-Ag distance 2.97(1) Å][25] and cross-link to the next layer to define a 3-D MOF (Figure 2.18a, top). For SBP, the silvers have a long contact of 3.60(1) Å, which is well outside the median covalent bond length of 3.047±0.193 Å by a search of Conquest/Vista in the Cambridge Crystal Structure Database (CSSD).[35]

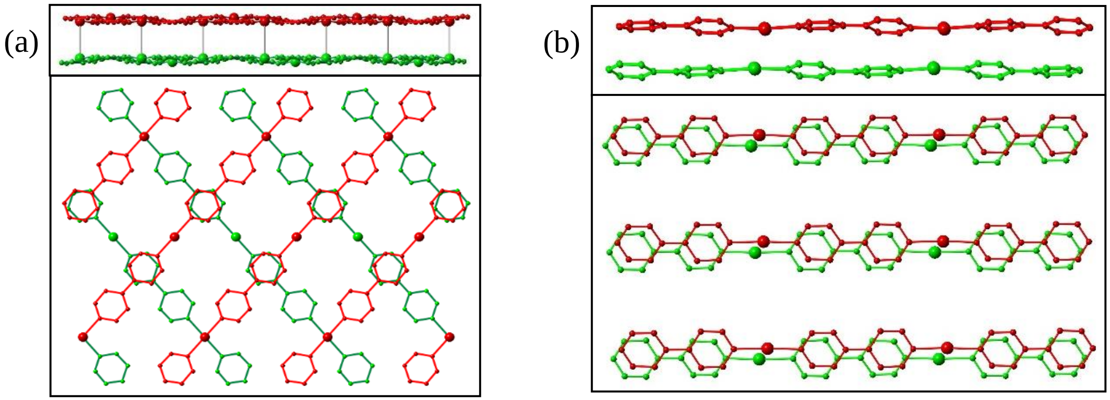

Figure 2.18 Crystallographic views of two $[\text{Ag-bipy}]^+$ "layers" (top in red, bottom in green; corresponding side views shown at top; anions and hydrogens omitted for clarity). (a) SBN, $[\text{Ag-bipy}^+][\text{NO}_3^-]$, where the layers are oriented ~ 90° to each other and only half the pyridine rings π-stack to the adjacent layer; (b) SBP, $[\text{Ag-bipy}^+][\text{ClO}_4^-]$, with the viewing angle offset slightly to emphasize the π–stacking of all pyridine rings.

These two structures transform reversibly and are a consequence of the shape of the incoming anion that must pack between the cationic polymers (Figure 2.17 side view of "layers" without anions). Nitrate is flat while perchlorate is tetrahedral (spheroidal). Both structures are stoichiometrically equivalent, with one mole of the monomeric anion in their formulae. The anion oxygen to silver distances are typical of ionic bonding [2.826(17) Å and 2.782(10) Å for SBN; 2.863(1) Å and 2.945(15) Å for SBP]. SBN, however, has half the π-stacking than. SBP is therefore more stable and accounts for the faster exchange of nitrate for very dilute perchlorate. Re-intercalation of nitrate requires greater concentration and longer time, where the polymers reassemble around the incoming anion to give quantitative exchange and fresh crystals for continuous exchange cycles.

2.4 Conclusions

A detailed methodology for the efficient separation of perchlorate from water was demonstrated by utilizing a cationic MOF consisting of three-dimensional $[\text{Ag-bipy}]^+$ chains arranged in a T-shaped pattern with nitrate anions counterbalancing the framework. The as-prepared SBN displays outstanding propensity towards the toxicologically important pollutant perchlorate due to the lower hydration energy of perchlorate relative to nitrate. The material exerts excellent capture capacity, kinetics, selectivity, regenerability and cyclability. The regeneration method actually takes advantage of the metastability of MOFs by reassembling back into the regenerated form simply using heat and excess nitrate. It is possible that other problematic elements that also occur in their oxo-anion form in water may be able to be trapped in this manner, such as chromium-6, arsenite, selenite/selenate or actinates. Overall, this discovery is a significant advance in the methods available for perchlorate trapping and water purification.

2.5 References

(1) Yang, Y.; Gao, N.; Chu, W.; Zhang, Y.; Ma, Y. Adsorption of Perchlorate from Aqueous Solution by the Calcination Product of Mg/(Al–Fe) Hydrotalcite-like Compounds. *J. Hazard. Mater.* **2012**, *209–210*, 318–325.

(2) Srinivasan, A.; Viraraghavan, T. Perchlorate: Health Effects and Technologies for Its Removal from Water Resources. *Int. J. Environ. Res. Public. Health* **2009**, *6* (4), 1418–1442.

(3) Dasgupta, P. K.; Martinelango, P. K.; Jackson, W. A.; Anderson, T. A.; Tian, K.; Tock, R. W.; Rajagopalan, S. The Origin of Naturally Occurring Perchlorate: The Role of Atmospheric Processes. *Environ. Sci. Technol.* **2005**, *39* (6), 1569–1575.

(4) Urbansky, E. T.; Schock, M. R. Issues in Managing the Risks Associated with Perchlorate in Drinking Water. *J. Environ. Manage.* **1999**, *56* (2), 79–95.

(5) Praharaj, S.; Nath, S.; Panigrahi, S.; Ghosh, S. K.; Basu, S.; Pande, S.; Jana, S.; Pal, T. Layer-by-Layer Deposition of Bimetallic Nanoshells on Functionalized Polystyrene Beads. *Inorg. Chem.* **2006**, *45* (4), 1439–1441.

(6) Mark, R.; Findley, W. N. Thermal Expansion Instability and Creep in Amine-Cured Epoxy Resins. *Polym. Eng. Sci.* **1978**, *18* (1), 6–15.

(7) Gu, B.; Brown, G. M.; Chiang, C.-C. Treatment of Perchlorate-Contaminated Groundwater Using Highly Selective, Regenerable Ion-Exchange Technologies. *Environ. Sci. Technol.* **2007**, *41* (17), 6277–6282.

(8) Gu, B.; Brown, G. M.; Maya, L.; Lance, M. J.; Moyer, B. A. Regeneration of Perchlorate (ClO_4^-)-Loaded Anion Exchange Resins by a Novel Tetrachloroferrate ($FeCl_4^-$) Displacement Technique. *Environ. Sci. Technol.* **2001**, *35* (16), 3363–3368.

(9) Dambies, L. Existing and Prospective Sorption Technologies for the Removal of Arsenic in Water. *Sep. Sci. Technol.* **2005**, *39* (3), 603–627.

(10) Neagu, V.; Bunia, I.; Plesca, I. Ionic Polymers VI. Chemical Stability of Strong Base Anion Exchangers in Aggressive Media. *Polym. Degrad. Stab.* **2000**, *70* (3), 463–468.

(11) Song, W.; Xu, X.; Tan, X.; Wang, Y.; Ling, J.; Gao, B.; Yue, Q. Column Adsorption of Perchlorate by Amine-Crosslinked Biopolymer Based Resin and Its Biological, Chemical Regeneration Properties. *Carbohydr. Polym.* **2015**, *115*, 432–438.
(12) *Layered Double Hydroxides: Present and Future*; Rives, V., Ed.; Nova Science Publishers: Huntington, N.Y, 2001.

(13) Kim, J. Y.; Komarneni, S.; Parette, R.; Cannon, F.; Katsuki, H. Perchlorate Uptake by Synthetic Layered Double Hydroxides and Organo-Clay Minerals. *Appl. Clay Sci.* **2011**, *51* (1–2), 158–164.

(14) Goh, K.-H.; Lim, T.-T.; Dong, Z. Application of Layered Double Hydroxides for Removal of Oxyanions: A Review. *Water Res.* **2008**, *42* (6–7), 1343–1368.

(15) Sumida, K.; Rogow, D. L.; Mason, J. A.; McDonald, T. M.; Bloch, E. D.; Herm, Z. R.; Bae, T.-H.; Long, J. R. Carbon Dioxide Capture in Metal–Organic Frameworks. *Chem. Rev.* **2012**, *112* (2), 724–781.

(16) Wang, B.; Côté, A. P.; Furukawa, H.; O'Keeffe, M.; Yaghi, O. M. Colossal Cages in Zeolitic Imidazolate Frameworks as Selective Carbon Dioxide Reservoirs. *Nature* **2008**, *453* (7192), 207–211.

(17) Long, J. R.; Yaghi, O. M. The Pervasive Chemistry of Metal–organic Frameworks. *Chem. Soc. Rev.* **2009**, *38* (5), 1213.

(18) Custelcean, R.; Moyer, B. A. Anion Separation with Metal–Organic Frameworks. *Eur. J. Inorg. Chem.* **2007**, *2007* (10), 1321–1340.

(19) Oliver, S. R. J. Cationic Inorganic Materials for Anionic Pollutant Trapping and Catalysis. *Chem. Soc. Rev.* **2009**, *38* (7), 1868.

(20) Zhao, X.; Bu, X.; Wu, T.; Zheng, S.-T.; Wang, L.; Feng, P. Selective Anion Exchange with Nanogated Isoreticular Positive Metal-Organic Frameworks. *Nat. Commun.* **2013**, *4*.

(21) Custelcean, R.; Haverlock, T. J.; Moyer, B. A. Anion Separation by Selective Crystallization of Metal−Organic Frameworks. *Inorg. Chem.* **2006**, *45* (16), 6446–6452.

(22) Rajbanshi, A.; Moyer, B. A.; Custelcean, R. Sulfate Separation from Aqueous Alkaline Solutions by Selective Crystallization of Alkali Metal Coordination Capsules. *Cryst. Growth Des.* **2011**, *11* (7), 2702–2706.

(23) Yang, T.; Wang, J.; Wang, J.-G.; Wang, S.; Xiao, H.-P. Three Silver(I) Coordination Polymers Assembled from 2-Sulfoterephthalic Acid and N-Donor Ligands: Syntheses, Crystal Structures, and Luminescence Properties. *Transit. Met. Chem.* **2013**, *38* (8), 865–871.
(24) Li, C.-P.; Chen, J.; Guo, W.; Du, M. Anion-Directed Assembly and Crystal Transformation of Ag(I) Coordination Polymers with a Versatile Tripyridyltriazole Ligand 3,4-Bis(2-Pyridyl)-5-(4-Pyridyl)-1,2,4-Triazole. *J. Solid State Chem.* **2015**, *223*, 95–103.

(25) Du, M.; Zhao, X.-J.; Guo, J.-H.; Batten, S. R. Direction of Topological Isomers of Silver(i) Coordination Polymers Induced by Solvent, and Selective Anion-Exchange of a Class of PtS-Type Host Frameworks. *Chem. Commun.* **2005**, No. 38, 4836.

(26) Fei, H.; Bresler, M. R.; Oliver, S. R. J. A New Paradigm for Anion Trapping in High Capacity and Selectivity: Crystal-to-Crystal Transformation of Cationic Materials. *J. Am. Chem. Soc.* **2011**, *133* (29), 11110–11113.

(27) Yaghi, O. M.; Hailian, L. T-Shaped Molecular Building Units in the Porous Structure of Ag (4, 4’-Bpy)⊙ NO3. *Journal of the American Chemical Society* **1996**, No. 118.1, 295–296.

(28) US EPA, O. Basic Information about Nitrate in Drinking Water http://water.epa.gov/drink/contaminants/basicinformation/nitrate.cfm (accessed Oct 31, 2015).

(29) Crawford, N. M.; Glass, A. D. . Molecular and Physiological Aspects of Nitrate Uptake in Plants. *Trends Plant Sci.* **1998**, *3* (10), 389–395.

(30) Fei, H.; Paw U, L.; Rogow, D. L.; Bresler, M. R.; Abdollahian, Y. A.; Oliver, S. R. Synthesis, Characterization, and Catalytic Application of a Cationic Metal−Organic Framework: Ag2 (4, 4′-Bipy) 2 (O3SCH2CH2SO3). *Chem. Mater.* **2010**, *22* (6), 2027–2032.

(31) Wang, L.-S.; Zhang, J.-F.; Yang, S.-P. *Catena* -Poly[[Silver(I)-μ-4,4′-Bipyridine-κ ^{2} *N* : *N* ′] Perchlorate]. *Acta Crystallogr. Sect. E Struct. Rep. Online* **2004**, *60* (10), m1484–m1486.

(32) Zhang, J.; Kang, Y.; Wen, Y.-H.; Li, Z.-J.; Qin, Y.-Y.; Cheng, J.-K.; Yao, Y.-G. Poly [[Dicopper (I)-Tri-μ-4, 4′-Bipyridyl] Diperchlorate Dihydrate]. *Acta Crystallogr. Sect. E Struct. Rep. Online* **2004**, *60* (4), m504–m505.

(33) Cui, X.; Khlobystov, A. N.; Chen, X.; Marsh, D. H.; Blake, A. J.; Lewis, W.; Champness, N. R.; Roberts, C. J.; Schröder, M. Dynamic Equilibria in Solvent-

Mediated Anion, Cation and Ligand Exchange in Transition-Metal Coordination Polymers: Solid-State Transfer or Recrystallisation? *Chem. - Eur. J.* **2009**, *15* (35), 8861–8873.

(34) Wang, Y.; Gao, H. Compositional and Structural Control on Anion Sorption Capability of Layered Double Hydroxides (LDHs). *J. Colloid Interface Sci.* **2006**, *301* (1), 19–26.

(35) Allen, F. H. The Cambridge Structural Database: A Quarter of a Million Crystal Structures and Rising. *Acta Crystallogr. B* **2002**, *58* (3), 380–388.

Chapter 3

Anion Exchange Dynamics in the Capture of Perchlorate from Water by a Cationic Ag-based MOF

Abstract

We report a detailed study of the host-guest interaction for a cationic metal-organic framework that can reversibly capture perchlorate. The structural transformation and flexibility of silver 4,4'-bipyridine nitrate (SBN) upon formation of silver 4,4'-bipyridine perchlorate (SBP) was evaluated by monitoring the anion exchange dynamics using a combination of powder X-ray diffraction (PXRD) with multinuclear ^{13}C, ^{15}N and ^{109}Ag solid-state nuclear magnetic resonance (NMR) spectra at different time intervals of the anion exchange. The structural transformation from SBN to SBP is complete within 70 minutes and was determined to take place by a solvent-mediated process. This pathway is confirmed by the morphological changes of the two crystalline materials observed by scanning electron microscopy (SEM). This key understanding may lead to application of this material towards perchlorate capture.

3.1 Introduction

Porous structures possessing weakly bound charge-balancing ions are essential for the development of new separation technologies and the removal of pollutant ions from aqueous environments. Recently, MOFs have been under intense investigation due to their ability to exchange their intrapore or interlayer ions with other ionic species in solution. Their structural integrity is not compromised, which make these materials excellent candidates for the separation of pollutants.[1] The adsorptive separation of pollutant species in the gas phase, such as carbon dioxide or methane, is driven by the reversible dynamic behavior of the network, often referred to as "breathing". This action results in a change of interaction strength between the guest molecules and host framework due to framework displacement accompanied by a change in the unit cell volume.[2] There has been much less effort into understanding the structural flexibility and dynamic transformations that solid MOFs exhibit during adsorption and/or ion exchange. The mechanism by which such ion exchange processes take place has been proposed to be either by a solid state or a solvent-mediated transformation. In the case of a solid state transition, the ion exchange proceeds through the diffusion of free ions within the channels of the coordination polymer crystals. In contrast, the solvent-mediated process involves the dissolution of the initial coordination polymer followed by the formation and crystallization of a new coordination polymer from the solution phase.[3]

The structural transformations that coordination polymers undergo during ion exchange processes can be monitored by single crystal or powder X-ray diffraction (PXRD) of the MOF in combination with analytical measurements of the solution and solid towards incoming and outgoing guests. If possible, single crystal X-ray crystallographic methods are preferred for the exact structural determination of the new MOF phase upon adsorption. This methodology, however, provides limited structural information regarding the dynamic behavior of the framework during exchange. In contrast, magic-angle spinning (MAS) NMR spectroscopy provides structural information about the local environment of various nuclei in solids, including the metal nodes, the organic linkers and the guests of the MOFs.[4] Hence, NMR spectroscopy could be used in conjunction with XRD methods as a complementary technique for analyzing the exchange dynamics of MOF materials.[5] NMR is well suited to probe the structural flexibility and reversible dynamic behavior of a framework undergoing ion exchange. Jiang *et al*. reported the structural flexibility of a $Cu(bipy)_2(H_2O)_2(BF_4)$ (bipy = 4,4'-bipyridine) structure by chemisorption of probe molecules that could induce reversible structural changes. The transitions could be monitored by ^{11}B MAS NMR as a result of the change in polarization of the probe molecule and its interaction with the Cu(II) sites.[6]

In our previous work,[7] we reported the successful capture of aqueous perchlorate by <u>S</u>ilver 4,4'-<u>B</u>ipyridine <u>N</u>itrate (SBN)[8] to yield a <u>S</u>ilver 4,4'-<u>B</u>ipyridine <u>P</u>erchlorate (SBP) MOF.[9] We showed that SBN effectively exchanged guest NO_3^- ions for ClO_4^- ions at a record capacity of 354 mg/g within 90 minutes. The material also selectively captured this pollutant in the presence of 50-fold molar SO_4^{2-} and CO_3^{2-}, suggesting this methodology could be applied to treat perchlorate pollution at underground plume sites. In addition, SBN displayed excellent reusability: 96 % of SBP could be regenerated back to SBN over multiple cycles while maintaining uptake capacity. Anion exchange by metal bipyridine and pyrazine coordination polymers was evaluated by Schröder and coworkers utilizing several anions such as BF_4^- and PF_6^-.[10] The uptake was determined to be a solvent-mediated process driven by the relative solubilities of the complex pairs as well as the relative hydration energy of the anions undergoing exchange.

Herein, we report a study of the host-guest interaction of an Ag-bipy coordinated polymer during NO_3^- and ClO_4^- anion exchange dynamics. The structural transformation is followed by analysis of the $[Ag\text{-}bipy]^+$ material at different time intervals using PXRD to assess the presence of two structural phases corresponding to SBN and SBP. The structural transformation during exchange is further investigated by recording multinuclear ^{13}C, ^{15}N and ^{109}Ag cross-polarization (CP) MAS NMR spectra. ^{13}C [1.13 % natural abundance (nat. ab.), nuclear spin I = 1/2] NMR is used to (semi)-quantify the SBN to SBP ratio during the anion exchange. ^{15}N (0.37 % nat. ab., I = 1/2) NMR determines whether NO_3^- is present and probes the bonding between the nitrogen of bipy and silver *via* the scalar J coupling interaction and is further confirmed by ^{109}Ag (48.18 % nat. ab., I = 1/2) NMR. In addition, this exchange is further investigated by inspecting the morphological changes of the crystalline materials by SEM.

3.2 Experimental Section

3.2.1 Synthesis

In short, a mixture of $AgNO_3$ ($AgNO_3$, Fisher, 99 %, 0.1 g, 0.59 mmol), 4,4'-bipyridine (Acros Organics, 98 %, 0.1 g, 0.64 mmol) and deionized water (10 mL) was stirred at room temperature for 3 days in a sealed beaker. Pale grey crystals were isolated after filtration and rinsed with water (10 mL) and acetone (5 mL) to yield SBN (0.187 g, 97.6 % based on silver nitrate). Batch anion exchange experiments were carried out under ambient conditions by mildly stirring the ground SBN (80 mg, 0.25 mmol) with 50 mL deionized water and $NaClO_4$ (Fluka Analytical, 98 %, 35 mg, 0.25 mmol). The post-exchange crystalline SBP product was recovered at the different time intervals by vacuum filtration and rinsed with water (10 mL) and acetone (5 mL).

3.2.2 Regeneration

The regeneration of SBN from SBP was carried out by stirring the ground SBP (80 mg, 0.22 mmol) in a 0.1 M $NaNO_3$ solution ($NaNO_3$, Fisher, 99 %) at 70 °C for 24 h. The regeneration of the SBN was studied by recording the PXRD, ^{13}C, ^{15}N, ^{109}Ag CP MAS NMR data and SEM images after treatment of the SBP material with excess nitrate at 70 °C under stirring.

3.2.3 Characterization

PXRD data were measured on a Rigaku Americas Miniflex Plus diffractometer, scanning from 2 to 40 ° (2θ) at a rate of 2 °/min with a 0.04 ° step size under Cu Kα radiation ($\lambda = 1.5418$ Å). Ion Chromatography (IC) analysis was performed to assess the perchlorate concentration using a Dionex ICS-3000 with an IonPac AS20 column and a detection limit of 3 µg/L (ppb). SEM data were collected with a FEI Quanta 3D Dualbeam microscope. Solid-state NMR: experiments were performed at room temperature on a Wide Bore 400 MHz 9.4 T Bruker Avance III HD NMR spectrometer equipped with a 4 mm HXY triple-resonance MAS probe (in double resonance mode) for ^{13}C and ^{15}N and with a 4 mm HX MAS probe for ^{109}Ag. Data acquisition was performed with cross polarization (CP) and SPINAL-64 heteronuclear decoupling.[11] Recycle delays ranging from 30 to 180 s were used and correspond to 1.3 x ^{1}H T_1 (measured by ^{1}H saturation recovery experiments). All other experimental details are given in Table A1. The ^{13}C, ^{15}N and ^{109}Ag chemical shifts were referenced to the CH carbon of adamantane at 29.45 ppm,[12] glycine at 33.4 ppm (corresponding to liquid NH_3 at 0 ppm)[13] and a saturated solution of $AgNO_3$ in D_2O [with 0.24 M of $Fe(NO_3)_3$] at 0 ppm,[14] respectively. All samples were packed in air. Using the Haeberlen convention,[15] the principal components δ_{11}, δ_{22}, δ_{33} of the chemical shift tensors were defined such that $|\delta_{33} - \delta_{iso}| \geq |\delta_{11} - \delta_{iso}| \geq |\delta_{22} - \delta_{iso}|$ where δ_{iso} is the isotropic chemical shift and related to the principal components of the shielding tensor by $\delta_{iso} = (\delta_{11} + \delta_{22} + \delta_{33})/3$. The chemical shift anisotropy δ_{aniso} is defined as $\delta_{aniso} = \delta_{33} - \delta_{iso}$ and the deviation from axial symmetry given by the asymmetry parameter $\eta = (\delta_{22} - \delta_{11})/ \delta_{aniso}$.

3.3 Results and Discussion

The synthesis of SBN can be carried out at room temperature by the initial dissociation of silver nitrate followed by the self-assembly of the cationic polymer chains, charge balanced by nitrate ions. SBN can undergo quantitative anion exchange upon exposure to ClO_4^- in solution to yield SBP with a 99 % conversion as determined by monitoring the concentration of ClO_4^- in solution from ion chromatography (IC). The PXRD data confirms the identity of the two crystalline phases as they match the theoretical patterns based on the single crystal solution (Figure 3.3).[8,9]

Both SBN and SBP structures consist of Ag(I) chelated by the nitrogens of two different (μ-2)-4,4'-bipyridine units that result in extended polymeric chains. The polymeric chains align parallel into a non π-stacked layer where the rings are coplanar with the plane of the page. The two structures differ in the arrangement of their subsequent layers. In the case of SBN, the cationic layers are rotated by 90°, forming a criss-cross or T-shaped pattern in which half the pyridine rings π-stack in a staggered manner with a distance of 3.55(1) Å from the next layer (Figure 3.1). In addition, half of the Ag(I) centers are dimerized and cross linked to the next layer by the formation of Ag-Ag bonds with a distance of 2.97(1) Å. In contrast, the cationic layers of SBP are eclipsed, resulting in π-stacking of all the pyridine rings and a shorter interlayer distance of 3.47(2) Å (Figure 3.1). The Ag(I) centers have a long contact distance of 3.60(1) Å, which is well above the covalent range. These longer Ag-Ag distances allow for the spherical ClO_4^- anions to be more spread out between the polymeric interlayers. The anion to Ag(I) distance is therefore greater for SBP than for SBN but closer contact of the anions to the bipyridine ***C***HC^{IV} in SBP (Table 1).

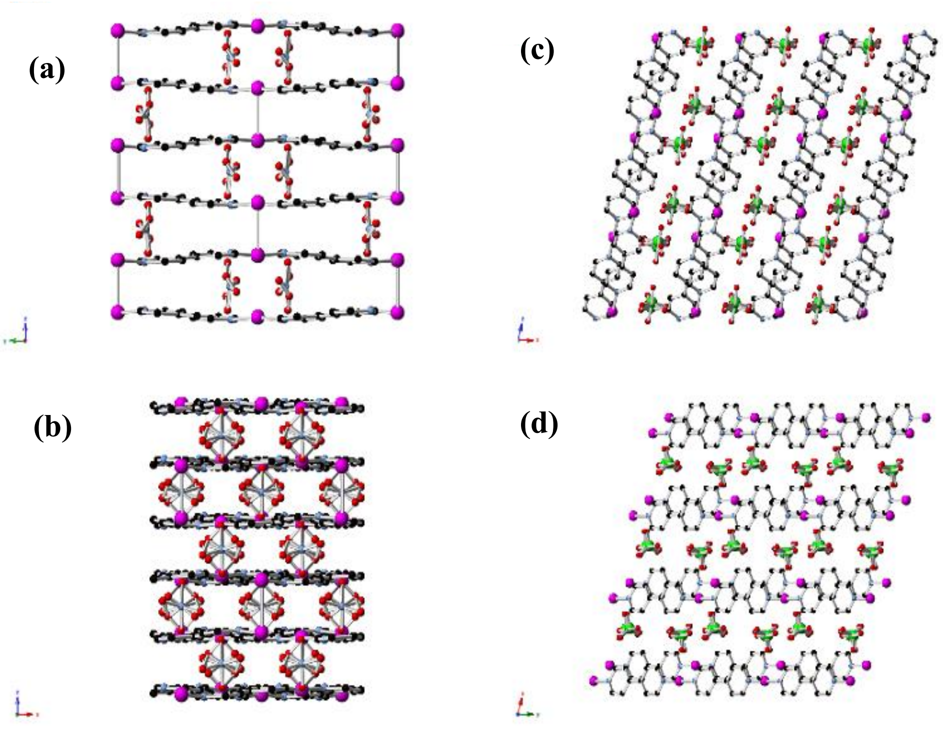

Figure 3.1 (a) Crystallographic view of SBN in the "a" plane and (b) "b" plane. (c) Crystallographic view of SBP in the "a" plane and (d) "c" plane. The nitrate oxygens are disordered between two sites (Ag, magenta; N, blue; O, red; C, black; Cl, green).

Table 3.1 Structural Properties of SBN and SBP

Distance	SBN	SBP
Ag(I)–Ag(I) / Å	2.97(1)	3.60(1)
Anion O–Ag(I) / Å	2.826(17), 2.782(10)	2.945(15), 2.863(10)
Anion O–***C***HC^{IV} / Å	3.374(10)	3.352(10)
π-stacking / Å	3.55(1)	3.47(2)
	Bond angle	
N–Ag(I)–N / °	173.73(1)	174.76(1)

Based on the above structural considerations, it is clear that the two coordination polymers are structurally different in the arrangement of the cationic layers as well as the location of the anions. Such structural differences suggest that the anion exchange may proceed by a solvent-mediated process involving the initial dissolution of the SBN T-shaped polymers followed by the crystallization of eclipsed SBP polymers from the perchlorate solution (Figure 3.2).[7] In order to support this hypothesis, the anion exchange was monitored versus time by both PXRD (Figure 3.3) and multinuclear MAS NMR (Figure 3.3). After 10 minutes of exposure to ClO_4^-, the intensity of the low angle (002) peak decreases and a new set of peaks [e.g. 22° (2θ), corresponding to the (211) plane of the SBP crystalline phase] begin to appear, indicating initiation of the process.

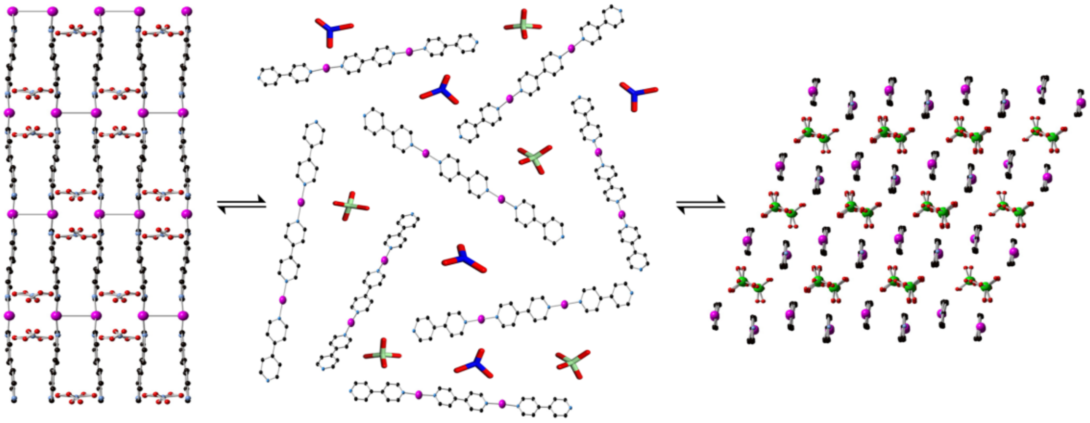

Figure 3.2 Perchlorate capture by SBN undergoing a solvent-mediated anion exchange to form SBP.

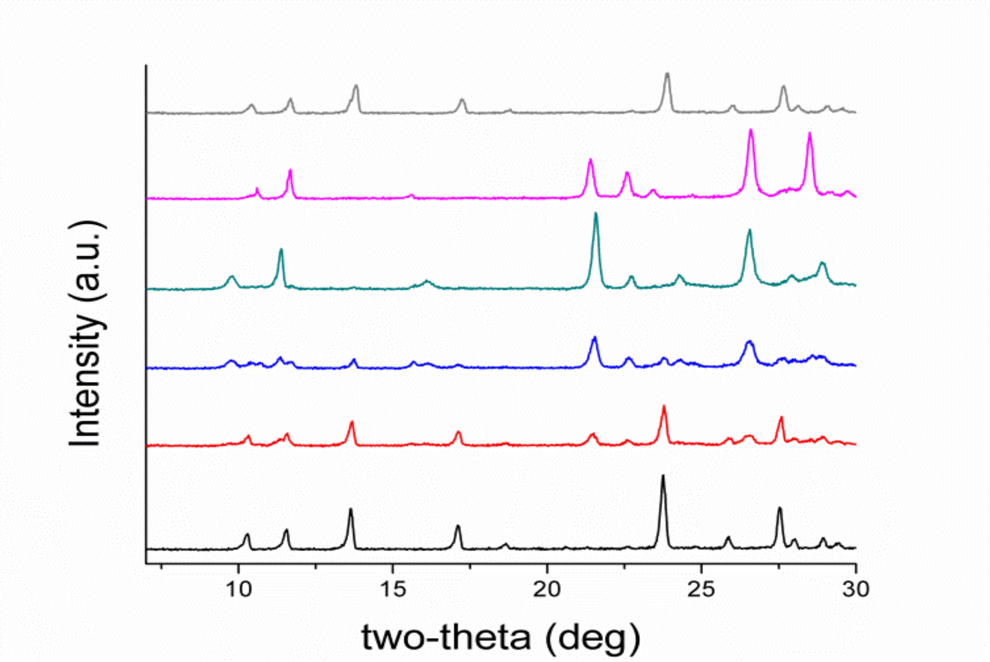

Figure 3.3 PXRD patterns of the SBN/SBP anion exchange: SBN pre-exchange (black), after 10 min (red), 25 min (blue), 40 min (green), complete exchange to SBP after 70 min (purple), and regeneration to SBN (grey).

After 25 minutes, the PXRD pattern is an approximately equal mixture of both the SBN and SBP crystal phases, indicating that the anions have been partially exchanged. The relative amounts of both phases were verified by measuring the residual concentration of perchlorate in the anion exchange solution at different time intervals with ion chromatography (Figure 3.4). The predominance of the SBP phase is observed after 40 minutes, where the low angle peaks corresponding to (001) and (100) of SBP are now higher intensity relative to the peaks of SBN. After 70 minutes, the anion exchange is complete and the PXRD pattern is pure phase SBP (see below for recovery to SBN). In addition, a shift in the (001) and (100) phases to a higher 2-theta indicates that the d-spacing decreased due to the smaller unit cell of SBP.

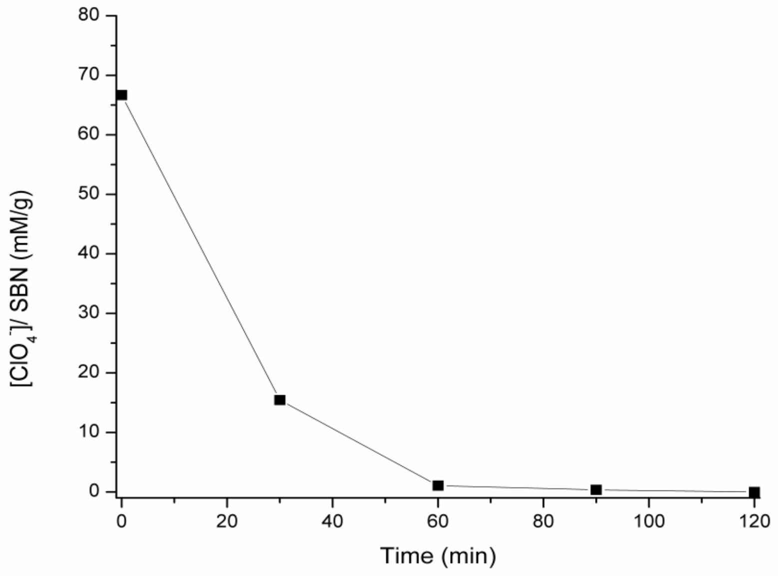

Figure 3.4 Perchlorate uptake per gram of SBN material.

The ^{13}C CP MAS NMR spectra of SBN and SBP (black and purple spectra, Figure 3.6a) show three different isotropic resonances δ_{iso} at 153.3, 144.1 and 123.5 - 121.7 ppm for the individual carbons in the asymmetric unit and correspond to the ***C***HN, C^{IV} and ***C***HC^{IV} carbons in the 4,4'-bipyridine ligand, respectively. As the NO_3^- – ClO_4^- anion exchange progressed by dissolution of SBN and subsequent capture of the ClO_4^- by the crystallization of SBP, a downfield shift of around 1.8 ppm is clearly observed in the signal of the ***C***HC^{IV} carbon (Figure 3.5). Comparison of the ***C***HC^{IV} signal intensities at 121.6 and 122.8 ppm for SBN and SBP, respectively, enables a semi-quantitative analysis of the rates of exchanges to be monitored (note that while CP MAS NMR experiments are not quantitative, integration is performed on the same ***C***HC^{IV} carbon; therefore a SBN/SBP ratio could be approximately estimated). After 10 and 25 minutes, approximately 20 and 56 % of SBN have been transformed into SBP, respectively. Partial degree of exchange at these time intervals agrees well with the PXRD data (red and blue patterns, Figure 3.6).

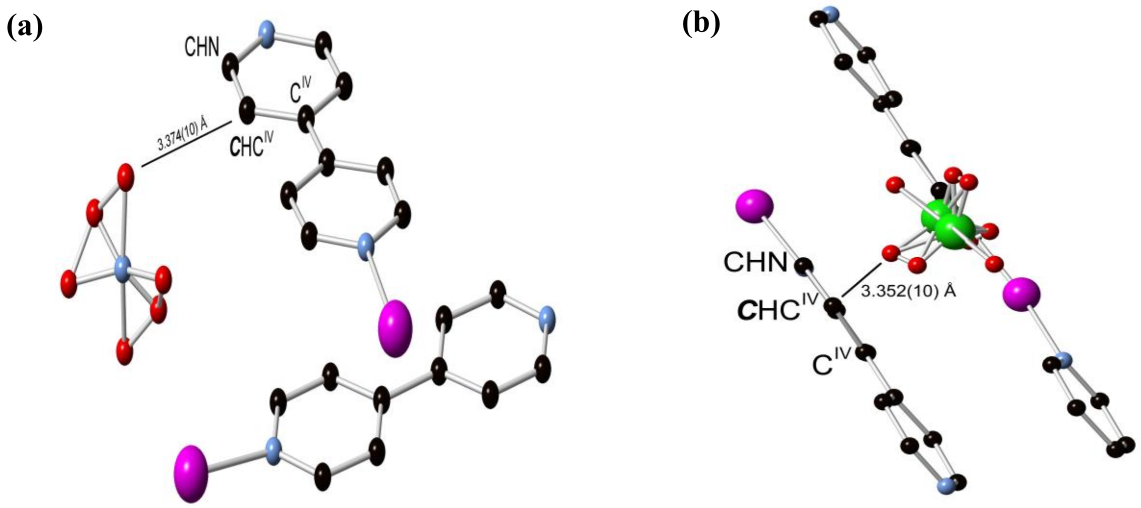

Figure 3.5 Structure view of Ag-bipy polymers showing anion oxygen to CH*C*^{IV} carbon proximity in: (a) SBN; and (b) SBP.

This shift difference between the ***C***HC^{IV} carbon in SBN and SBP is probably due to the higher degree of carbon deshielding caused by the perchlorate anions. As stated above, the cationic layers of SBP have a shorter π-stacking distance relative to SBN due to the fully eclipsed arrangement of the Ag-bipy chains. This shorter distance causes the spherical ClO_4^- anions to be more tightly packed between the aromatic rings and in turn a longer Ag-O distance compared to the flat nitrate anions which reside in closer contact to the Ag centres. Consequently, the ClO_4^- oxygens are in closer proximity to ***C***HC^{IV} carbon, resulting in a higher degree of deshielding as reflected by the observed chemical shift. Close inspection of the C^{IV} carbon signal at 145 ppm in SBP (purple spectrum, Figure 3.6a) reveals a poorly resolved doublet. The doublet may arise from residual ^{13}C – $^{35/37}Cl$ heteronuclear dipolar interaction that is not fully averaged out to zero by MAS[16] due to the strong quadrupolar moments of both $^{35/37}Cl$ nuclei. No multiplicity resulting from ^{13}C – ^{14}N coupling is observed for the same carbon in SBN. This observation is probably due to the lower quadrupolar moment of ^{14}N (2.0×10^{-30} m^2) vs. ^{35}Cl (-8.2×10^{-30} m^2) and ^{37}Cl (-6.4×10^{-30} m^2), as well as the weaker interaction between the NO_3^- and aromatic rings in SBN than between the ClO_4^- and those in SBP.

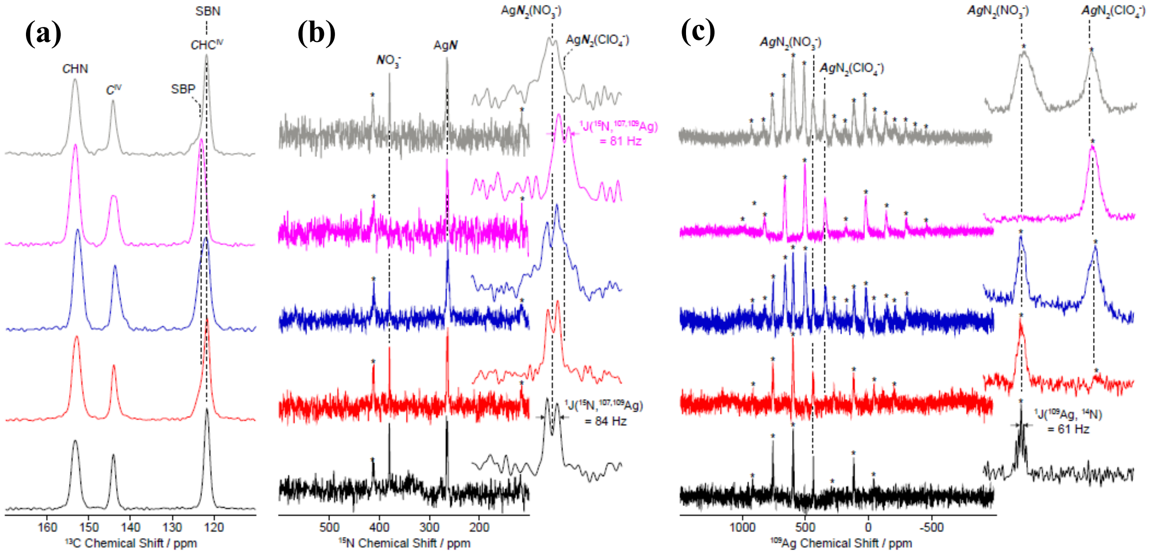

Figure 3.6 (a) ^{13}C, (b) ^{15}N and (c) ^{109}Ag CP MAS NMR of the SBN/SBP anion exchange of SBN pre-exchange (black), after 10 min (red), 25 min (blue), complete exchange to SBP (purple) and regeneration back to SBN (grey). Spectral assignments are given in the figure. In (b), the insets show magnified views of the 280−250 ppm isotropic region of the AgN resonances. In (c), the insets show magnified views of the first left spinning sidebands in the 650-450 ppm region. Spinning sidebands are marked with asterisks (*)

The ^{15}N CP MAS NMR spectrum of SBN (Figure 3b, black) reveals two isotropic resonances δ_{iso} at 379.3 and 263.9 ppm and are assigned to the NO_3^- anions and the nitrogen of the bipy ligand, respectively. A doublet of 84 Hz is observed for the former resonance and results from the indirect scalar $^{1}J(^{15}N, ^{107,109}Ag)$ coupling arising from coordination of the nitrogen atoms of bipy to the silver atoms, as expected from the crystal structure (Figure 3.1). Similar scalar coupling constants were obtained in a series of linear or almost linear two-coordinate $[Ag(NH_3)_2]^+$ ions.[17]

The ^{109}Ag CP MAS NMR[18] spectrum of SBN (purple, Figure 3.6c) shows a series of intense spinning sidebands spanning over approximately 1000 ppm, in agreement with the large chemical shift anisotropy of ^{109}Ag of δ_{aniso}= -774 ppm. Note that the relatively low signal to noise ratio of this ^{109}Ag spectrum arises from the very low magnetic moment of this nucleus. A single isotropic resonance appears at δ_{iso} = 438.5 ppm and is consistent with a single silver atom environment in SBN. This resonance is a quintet with a spacing of 61 Hz, corresponding to the indirect scalar coupling between ^{109}Ag and ^{14}N (99.63 % nat. ab., I = 1). The approximate 1:2:3:2:1 relative intensity of the quintet is expected for coupling to two equivalent I = 1 nuclei and the crystal structure of SBN presenting a silver atom nitrogen-bonded by two bipy ligands. Note that the $^{1}J(^{15}N, ^{107,109}Ag) : ^{1}J(^{109}Ag, ^{14}N)$ ratio is 1.38, close to the expected $^{15}N : ^{14}N$ magnetic moment ratio of 1.40. Additionally, the spinning sideband manifold yields an axially symmetric chemical shift tensor (i.e. $\eta = 0$). This observation agrees well with the almost linear environment[15] of the N–Ag(I)–N moieties in the bipy–Ag–bipy polymers (173.73°, Table 3.1).

As SBN is converted into SBP by addition of ClO_4^-, the relative ratio of the NO_3^- anions and the bipy ligand signals at 379.3 and 263.9 ppm in the ^{15}N CP MAS

NMR spectra decreases, until a single nitrogen environment is detected upon total exchange to SBP. The corresponding ^{15}N spectrum (purple, Figure 3b) shows a doublet with $^{1}J(^{15}N, ^{107,109}Ag)$ = 81 Hz centred at δ_{iso} = 261.4 ppm. This signal is due to the nitrogen atoms of bipy that are bonded to Ag. No resonance could be detected at 379.3 ppm in SBP, consistent with the complete NO_3^- - ClO_4^- anion exchange as seen by PXRD. The very small difference in chemical shift between the nitrogen atoms of bipy in SBN and SBP likely arises from the greater deshielding of the bipy nitrogen in SBN by the NO_3^- that is in closer proximity to the silver atom. The ^{15}N CP MAS NMR spectra for SBN and SBP are therefore consistent with the ^{13}C CP MAS NMR spectra in the arrangement of the Ag-bipy cationic layers upon exchange of NO_3^- for ClO_4^- perchlorate anions.

Upon SBN/SBP anion exchange, the ^{109}Ag CP MAS NMR spectra (Figure 3.6c) reveal the appearance of an additional isotropic resonance at approximately δ_{iso} = 341 ppm. Its intensity increases with ClO_4^- content and is attributed to the $[Ag\text{-}bipy]^+$ moiety in SBP. Upon total exchange, the ^{109}Ag signal of SBN completely disappears, in agreement with the PXRD, ^{13}C and ^{15}N data discussed above. Note that no $^{1}J(^{109}Ag, ^{14}N)$ scalar coupling could be clearly detected in the ^{109}Ag CP MAS NMR spectrum of SBP, probably resulting from slightly broader NMR lines and disorder. An axially symmetric ^{109}Ag chemical shift tensor with δ_{aniso} = -776 ppm and η= 0 is also obtained, the later value in agreement with the linear N – Ag(I) – N angle in SBP (Table 1).

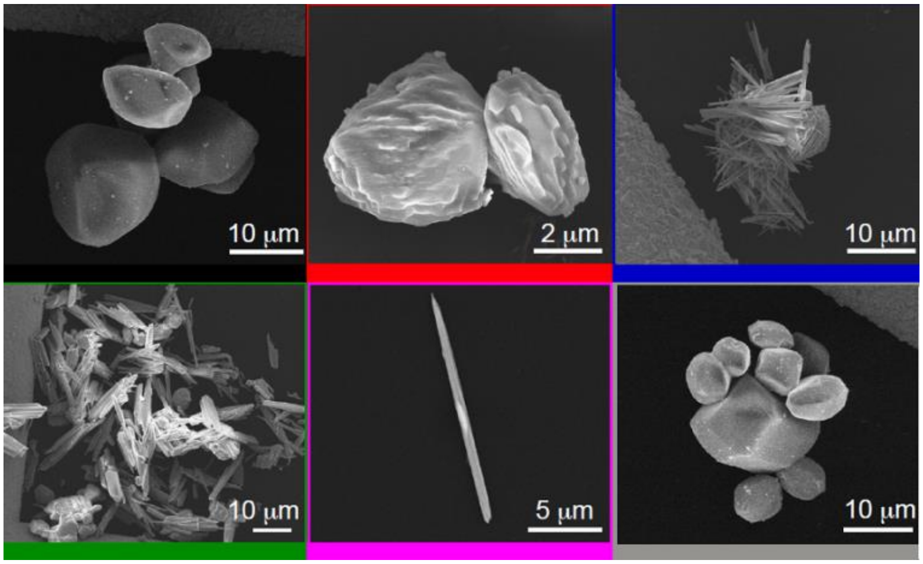

Figure 3.7 SEM images of SBN pre-exchange (black, top left) and the solid after 10 min (red), 25 min (blue), 40 min (green), complete exchange to SBP (purple), and the first regeneration to SBN (grey).

The change in morphology of the SBN crystals during anion exchange with ClO_4^- was investigated by performing batch tests experiments, stopping the reaction at various time intervals to analyse the resulting crystals by SEM (Figure 3.7). Initially, the synthesis of SBN yields smooth block-shaped crystals with an average width of 4 to 10 µm (black, top left, Figure 3.7). Upon 10 min of exposure of the SBN crystals to the ClO_4^- aqueous solution, the smooth block shaped crystals began to display indentations at the surface (red, Figure 3.7). These indentations show that the new SBP phase is beginning to take form on the SBN crystals, similar to that reported by Schröder and coworkers for $[Ag(4,4\text{-bipy})^+][BF_4^-]$ to $[Ag(4,4\text{-bipy})^+][NO_3^-]$.[10] After 25 min, small needles corresponding to the SBP crystal phase are observed in addition to SBN blocks with indentations (blue, Figure 3.7). After 40 min, the crystals have lost their block-shaped morphology and consist primarily of bundles of needles that appear to be nucleated from the SBN block crystals (green, Figure 3.7). The anion exchange is complete after 70 minutes and only long SBP needles could be identified (purple, Figure 3.7), with average length 12 to 15 µm and width 2 to 4 µm.

The gradual change in morphology of the SBN block crystals to SBP needles upon exposure to ClO_4^- solution confirms that the structural transformation between the two coordination polymers occurs by a solvent-mediated process, consistent with the PXRD patterns and MAS NMR spectra described above. The self-propagating growth of a new crystal phase from a parent phase has been proposed to facilitate the exchange of anions in the inside core of $[Ag(4,4\text{-bipy})^+][BF_4^-]$ crystals undergoing the structural transformation to $[Ag(4,4\text{-bipy})^+][NO_3]$.[3]

The reversibility of the anion exchange was demonstrated in our previous work and seven cycles of perchlorate uptake were monitored by PXRD.[7] The metastability of the $[Ag\text{-bipy}]^+$ solids allow for the reversible solvent-mediated transformation that can be controlled by the concentration of the incoming anions and temperature. The lower solubility of SBP as well as its higher stability due to the greater degree of π-stacking account for the rapid SBN to SBP transition. In contrast, the re-intercalation of nitrate is a less favoured process due to the larger hydration energy of nitrate. Additionally, SBN has a lower stability due to the partial π-stacking.

The regeneration of the SBN was further studied by recording the PXRD, ^{13}C, ^{15}N, ^{109}Ag CP MAS NMR data and SEM images after treatment of the SBP material with excess nitrate at 70 °C under stirring (grey spectra, Figures 3-4). The heat promotes the dissolution of the SBP polymers, while the excess nitrate shifts the dynamic equilibrium of the exchange to return to block shaped crystals with morphology identical to the as-synthesized SBN material (*cf*. black and grey SEMs, Figure 3.7). The corresponding PXRD, ^{13}C and ^{109}Ag NMR data showed that although SBN has been mostly regenerated, approximately 10 % of SBP is still present (as evidenced by integration of the NMR spectra and PXRD peaks).

3.4 Conclusions

This work shows by multiple complementary solid state methods that ClO_4^- uptake by S̲ilver 4,4'-B̲ipyridine N̲itrate (SBN) [Ag-bipy$^+$][NO_3^-] occurs via a solvent-mediated process to yield S̲ilver 4,4'-B̲ipyridine P̲erchlorate (SBP). The structural features of the silver coordination polymers in terms of π-stacking and electrostatics concur with the dynamics of the anion exchange process. All three characterization methods show that the two crystalline phases are present throughout the anion exchange process. This study provides evidence of the structural flexibility displayed by the interaction of cationic [Ag-bipy$^+$] MOFs with different adsorbates upon anion exchange. Such understanding of structural dynamics is crucial for the rational design of these and related MOFs toward the selective capture of environmental pollutant oxyanions such as perchlorate, chromate and arsenate. Reusability over many cycles is also crucial for the cost-effective deployment of these materials. The formation of new crystals on each exchange cycle circumvents the degradation issues of current ion exchange solids such as resins and LDHs that force them to be single-use.

3.5 References

(1) Custelcean, R.; Haverlock, T. J.; Moyer, B. A. Anion Separation by Selective Crystallization of Metal−Organic Frameworks. *Inorg. Chem.* **2006**, *45* (16), 6446–6452.

(2) Schneemann, A.; Bon, V.; Schwedler, I.; Senkovska, I.; Kaskel, S.; Fischer, R. A. Flexible Metal–organic Frameworks. *Chem Soc Rev* **2014**, *43* (16), 6062–6096.

(3) Thompson, C.; Champness, N. R.; Khlobystov, A. N.; Roberts, C. J.; Schroder, M.; Tendler, S. J. B.; Wilkinson, M. J. Using Microscopic Techniques to Reveal the Mechanism of Anion Exchange in Crystalline Co-Ordination Polymers. *J. Microsc.* **2004**, *214* (3), 261–271.

(4) Laws, D. D.; Bitter, H.-M. L.; Jerschow, A. Solid-State NMR Spectroscopic Methods in Chemistry. *Angew. Chem. Int. Ed.* **2002**, *41* (17), 3096–3129.

(5) Hoffmann, H.; Debowski, M.; Müller, P.; Paasch, S.; Senkovska, I.; Kaskel, S.; Brunner, E. Solid-State NMR Spectroscopy of Metal–Organic Framework Compounds (MOFs). *Materials* **2012**, *5* (12), 2537–2572.

(6) Jiang, Y.; Huang, J.; Kasumaj, B.; Jeschke, G.; Hunger, M.; Mallat, T.; Baiker, A. Adsorption−Desorption Induced Structural Changes of Cu-MOF Evidenced by Solid State NMR and EPR Spectroscopy. *J. Am. Chem. Soc.* **2009**, *131* (6), 2058–2059.

(7) Colinas, I. R.; Silva, R. C.; Oliver, S. R. J. Reversible, Selective Trapping of Perchlorate from Water in Record Capacity by a Cationic Metal–Organic Framework. *Environ. Sci. Technol.* **2016**, *50* (4), 1949–1954.

(8) Yaghi, O. M.; Hailian, L. T-Shaped Molecular Building Units in the Porous Structure of Ag (4, 4’-Bpy)⊙ NO3. *Journal of the American Chemical Society* **1996**, No. 118.1, 295–296.

(9) Wang, L.-S.; Zhang, J.-F.; Yang, S.-P. *Catena* -Poly[[Silver(I)-μ-4,4′-Bipyridine-κ ^{2} *N* : *N* ′] Perchlorate]. *Acta Crystallogr. Sect. E Struct. Rep. Online* **2004**, *60* (10), m1484–m1486.

(10) Cui, X.; Khlobystov, A. N.; Chen, X.; Marsh, D. H.; Blake, A. J.; Lewis, W.; Champness, N. R.; Roberts, C. J.; Schröder, M. Dynamic Equilibria in Solvent-Mediated Anion, Cation and Ligand Exchange in Transition-Metal Coordination Polymers: Solid-State Transfer or Recrystallisation? *Chem. - Eur. J.* **2009**, *15* (35), 8861–8873.

(11) Fung, B. M.; Khitrin, A. K.; Ermolaev, K. An Improved Broadband Decoupling Sequence for Liquid Crystals and Solids. *J. Magn. Reson.* **2000**, *142* (1), 97–101.

(12) Morcombe, C. R.; Zilm, K. W. Chemical Shift Referencing in MAS Solid State NMR. *J. Magn. Reson.* **2003**, *162* (2), 479–486.

(13) Bertani, P.; Raya, J.; Bechinger, B. 15N Chemical Shift Referencing in Solid State NMR. *Solid State Nucl. Magn. Reson.* **2014**, *61–62*, 15–18.

(14) Plischke, J. K.; Benesi, A. J.; Vannice, M. A. Solid-State Silver-109 NMR Characterization of Silver Dispersed on Oxide Supports. *J. Phys. Chem.* **1992**, *96* (9), 3799–3806.

(15) Mehring, M. *Principles of High Resolution NMR in Solids*, 2nd. ed.; Springer Verlag: Berlin, 1983.

(16) Hexem, J. G.; Frey, M. H.; Opella, S. J. Influence of Nitrogen-14 on Carbon-13 NMR Spectra of Solids. *J. Am. Chem. Soc.* **1981**, *103* (1), 224–226.

(17) Bowmaker, G. A.; Harris, R. K.; Assadollahzadeh, B.; Apperley, D. C.; Hodgkinson, P.; Amornsakchai, P. Solid-State109Ag CP/MAS NMR Spectroscopy of Some Diammine Silver(I) Complexes. *Magn. Reson. Chem.* **2004**, *42* (9), 819–826.

(18) Merwin, L.; Sebald, A. The First Examples of 109Ag CP MAS Spectroscopy. *J. Magn. Reson. 1969* **1992**, *97* (3), 628–631.

Chapter 4

Synthesis and characterization of two structurally diverse Zn-based coordination polymers with excellent antibacterial activity

Abstract

The synthesis, antibacterial properties and mechanism of two Zn-based coordination polymers (CPs) is reported. The first, $[\mathrm{Zn(bipy)(OH_2)_4}^{2+}]_{1.5}[\mathrm{ClO_4}^{-}]_3\bullet\mathrm{(bipy)_3(H_2O)}$, consists of a one-dimensional (1D) structure with two crystallographically independent octahedral zinc centers trans-coordinated by two 4,4'-bipy units and water groups. The second, $[\mathrm{Zn_{1.5}(CH_3CO_2)_2(bipy)_2}^{+}][\mathrm{ClO_4}^{-}]\bullet\mathrm{H_2O}$, is a two-dimensional (2D) layered structure with the same polymers but bridged together into a layer by acetate and 4,4’-bipy. Both compounds exhibit sustained release of Zn^{2+} ions upon their gradual degradation in aqueous solution, which results in highly effective antibacterial activity towards *Escherichia coli* and particularly towards *Staphylococcus epidermidis* cells. This activity was evaluated in solution by broth dilution assays to determine minimal inhibition concentrations (MICs) as well as in the solid phase by agar diffusion tests to quantify the zones of inhibition (ZOI), and were in close agreement. Further, the biocidal mechanisms of the coordination

polymers were investigated *in vivo* by fluorescence microscopy utilizing CellRox Green and propidium iodide as reactive oxygen species (ROS) and membrane disruption indicators, respectively. Both CPs show superior antibacterial activity compared to two standards, zinc acetate and zinc oxide, which is concluded to be due to both gradual and localized release of Zn^{2+} ions as well as electrostatic attraction to the bacterial cell surface afforded by their unique structures. This unique Zn^{2+} release profile and interaction with bacterial surfaces affords marked antibacterial activity and suggests that manipulation of the Zn^{2+} structures could lead to significant advancements in antimicrobial materials.

4.1 Introduction

Increasing antibiotic resistance of pathogens has become a serious threat to public health. The spread of these resistant pathogens is occurring at a faster rate than the discovery of new antibacterial agents, contributing to the recent rise of untreatable infections.[1] It is estimated that more than two million people in the United States are infected with resistant bacteria annually, with over 23,000 deaths as a direct result.[2] Given that both intrinsic and acquired bacterial resistances are mediated by genetic pathways such as mutations in chromosomal genes in response to exposure of the cell to an antibacterial agent, new strategies to develop materials with effective, broad-spectrum antibacterial activity are needed in order to mitigate genetic bacterial resistance.[3]

An effective approach to control the spread of antibiotic resistant bacteria is to consider a material that exhibits this broad-spectrum biocidal activity both in liquid environments, and on solid surfaces. Infectious bacteria are most commonly found in a sessile state in the form of a biofilm, rather than in a planktonic or free-swimming form. This biofilm is responsible for adhesion of bacteria to surfaces and plays a significant role in the transmission of antibiotic-resistant infections.[4] Hence, the fabrication of new materials that can be used for prophylactic purposes, such as surface treatment of surgical tools and implanted medical devices, as well as more common surfaces such as door handles, light switches, and countertops could prove to be an effective strategy to prevent the growth of biofilms and, in turn, the spread of antibiotic resistant infections.

The antimicrobial use of metals such as silver (Ag), gold (Au), cobalt (Co), copper (Cu) and zinc (Zn) has been widely studied and applied for centuries.[5-8] Recently, the field of nanotechnology has incorporated these metals into nanostructured systems for improved dosage forms and therapeutic effects.[9,10] Unlike conventional antibiotics, the antibacterial activity of nanomaterials is broad-spectrum, and includes physical damage to bacterial cells. These mechanisms typically involve the release of toxic metal ions and formation of reactive oxygen species (ROS). The affinity of these metal ions for biomolecules as well as their ability to generate ROS result in a variety of toxic effects, including altered membrane permeability, loss of proton motive force, leakage of cellular contents, and arrest of DNA replication.[11] Among these metal containing nanomaterials, silver is the most widely used bioactive metal due to the interaction of silver ions with multiple cellular targets, conferring its broad spectrum activity against bacterial cells.[12-15] The main drawback of Ag compounds and nanostructures however, are their relatively high cost and the limited solubility of Ag^+ in the presence of chloride ions [$K_{sp}(AgCl) = 1.77 \times 10^{-10}$]. Cl^- ions are a common species in bacterial habitats and inside bacterial cells, causing precipitation of Ag^+ and adversely affecting nanoparticle aggregation and dissolution kinetics.[16,17]

In contrast, zinc is a low cost, endogenous transition metal whose chloride complex has a strong thermodynamic propensity for hydration.[18,19] Zinc has been incorporated in various compounds for a wide range of applications such as antimicrobial agents and treatment of Alzheimer's disease.[20-22] In an effort to understand the toxicity of zinc ions towards bacteria, Paton *et al.* performed both *in vivo* and *in vitro* analyses with *Streptococcus pneumoniae*.[23] The authors revealed that extracellular Zn(II) inhibits the acquisition of Mn(II) by gram-positive bacterial cells by competitive binding via the solute-binding protein PsaA. Their studies demonstrated that this extracellular cation competition can occur for several pathogenic and non-pathogenic bacteria, resulting in oxidative stress due to starvation of essential Mn(II). The antimicrobial effect of ZnO nanoparticles on gram-negative *E. coli* cells has also been demonstrated in a study by Brayner et *al.*[24] They found that ZnO nanoparticles exerted their biocidal activity by damaging the cell membrane through cellular internalization, the degree of which was governed by the nature of the capping ligand. These studies shed light on the mechanisms of zinc-based structures' bactericidal properties, and demonstrate their efficacy for antimicrobial applications, prompting further investigation to achieve additional improvements.

Although highly effective, ZnO nanoparticles require a passivating agent to prevent their aggregation[25] which can be detrimental[24] to the antibacterial activity. Therefore, a material that provides stoichiometric release of biocidal metal ions without aggregation would be an ideal platform for antibacterial Zn-based materials. Metal-organic frameworks (MOFs), more generally known as coordination polymers (CPs), are an emerging class of materials with wide diversity of topologies and properties which is afforded by the plethora of metal centers and organic linkers used to design them. The structure of a CP is tunable by synthetic factors such as the coordination geometry of the metal center, the nature of the ligand as well as counter anions and synthetic conditions such as temperature, their molar ratios or solvent system.[26] Although these hybrid materials have been traditionally investigated for applications in gas storage,[27] sensing,[28] separation,[29] and drug delivery,[30] they have recently demonstrated interesting antibacterial activity.

The antibacterial properties typically originate from the metals in their cationic form, with the structures acting as metal ion reservoirs. Both the organic linkers and ions residing in the pores, however, may contribute to the antibacterial activity.[11] For instance, the biocidal activity of a Zn-based MOF was previously demonstrated to result from the additive effect of Zn^{2+} and azelate moiety which acted as a bioactive linker for the Zn^{2+} nodes.[31] This MOF demonstrated successful inhibition of *S. aureus* and *S. epidermidis* growth by its progressive release of Zn^{2+}

ions and azelaic acid. The biocidal mechanism of each of these moieties however, was not thoroughly addressed, leaving the exact roles of these two bactericidal species unsolved. Herein, we report the hydrothermal synthesis of two zinc-based CPs, $[Zn(bipy)(OH_2)_4{}^{2+}]_{1.5}[ClO_4{}^{-}]_3\cdot(bipy)_3(H_2O)$ (which we denote SLUG-39, for University of California, Santa Cruz, Structure, No. 39) and $[Zn_{1.5}(C_2H_3O_2)_2(bipy)_2{}^{+}][ClO_4{}^{-}]\cdot H_2O$ (SLUG-40). Both consist of Zn^{2+} ions as the metal nodes connected by 4,4'-bipyridine linkers, SLUG-39 forms a one-dimensional (1D) structure with two crystallographically independent octahedral zinc centers trans-coordinated by two 4,4'-bipy units and water groups, while SLUG-40 is a two-dimensional (2D) layered structure with the same polymers but bridged together into a layer by acetate and 4,4'-bipy. We detail their synthesis, characterization, and provide an in-depth evaluation of their biocidal activity against gram-negative (*E. coli*) and gram-positive bacteria (*S. epidermidis*).

4.2 Experimental Section

4.2.1 Reagents

Zinc nitrate hexahydrate [$Zn(NO_3)_2\cdot 6H_2O$, Fisher, 99.5%], zinc acetate dihydrate [$Zn(CH_3CO_2)_2\cdot 2H_2O$, Mallinckrodt chemicals, 98%], sodium perchlorate monohydrate [$NaClO_4\cdot H_2O$, Fluka, 98%], 4,4'-bipyridine [$C_{10}H_8N_2$, Acros, 98%] and Miller Luria broth (Fisher) were all used as-received. Water was supplied by a Barnstead Nanopure water system (18.3 MΩ•cm).

4.2.2 Synthesis of SLUG-39

A mixture of $Zn(NO_3)_2{\cdot}6H_2O$ (1.4 mmol), $NaClO_4{\cdot}H_2O$ (1.4 mmol) and 4,4'-bipyridine (2.8 mmol) was stirred mildly for 1 h in 10 mL of H_2O, then sealed in a 15 mL Teflon-lined stainless steel autoclave and heated at 150 °C for 20 h under autogenous pressure. Large light-pink needles were isolated under vacuum filtration and subsequently rinsed with deionized water and acetone (yield: 0.34 g, 60.9% based on 4,4'-bipy). Elemental analysis (Galbraith Laboratories, Inc.): C, 44.27% (44.11% theoretical); H: 3.88% (4.08% theoretical); N: 10.28% (10.29% theoretical). FT-IR (cm^{-1}): 1615, 1600, 1536 (m, νC=N), 1490, 1418 (m, νC=C), 1095 (s, νClO_4^-), 812 (m, νC-H), 509 (m, νZn-O), 476 (m, νZn-N).

4.2.3 Synthesis of SLUG-40

A mixture of $Zn(CH_3CO_2)_2{\cdot}2H_2O$ (1.4 mmol), $NaClO_4{\cdot}H_2O$ (1.4 mmol) and 4,4'-bipyridine (2.8 mmol) was stirred mildly for 1 h in 10 mL of H_2O, then sealed in a 15 mL Teflon-lined stainless steel autoclave and heated to 150 °C for 20 h under autogenous pressure. Yellow tan flake crystals were isolated under vacuum filtration and subsequently rinsed with deionized water and acetone [yield: 0.46 g, 70.8% based on $Zn(OAc)_2$]. Elemental analysis (Galbraith Laboratories, Inc.): C, 43.72% (44.62% theoretical); H: 3.70% (3.75% theoretical); N: 8.68% (8.43% theoretical). FT-IR (cm^{-1}): 1605, 1581(m, νC=N), 1408 (m, νC-O-), 1064 (s, νClO_4^-), 812 (m, νC-H), 510(m, νZn-O), 479 (m, νZn-N).

4.2.4 Characterization

Single crystal data for SLUG-39 and SLUG-40 were recorded using a Bruker APEX II CCD area detector X-ray diffractometer with graphite monochromated Mo-Kα radiation (λ = 0.71073 Å). The structures were solved by direct methods and expanded routinely. The models were refined by full-matrix least-squares analysis of F_2 against all reflections. All non-hydrogen atoms were refined with anisotropic thermal displacement parameters. Hydrogen atom positions were calculated geometrically and refined isotropically using the riding model. TwinRotMat function within ***PLATON*** program indeed suggested a twin law for SLUG-39 crystal data. This structure was re-refined against an hklf5 file. PXRD for both structures was measured on a Rigaku Americas Miniflex Plus diffractometer, scanning from 2 to 40° (2θ) at a rate of 2°/min with a 0.04° step size under Cu-Kα radiation (λ = 1.5418 Å). Thermogravimetric analysis (TGA) was performed on a TA Instruments TGA Q500 by heating from 25 to 600 °C under N_2 purge with a gradient of 5 °C/min. Elemental analysis (CHN) was performed on a EAI CE-440 elemental analyzer. A PerkinElmer Spectrum-One FT-IR spectrometer was used to obtain the IR spectra of the compounds.

4.2.5 Quantification of Zn^{2+} Release

Samples of SLUG-39 and SLUG-40 were ground and immersed in distilled water at 37 °C at a concentration of 100 ppm. Aliquots of the supernatant solution were initially taken every 20 min, and then every 24 h for the first 4 d. The Zn^{2+} concentration was determined by Inductively Coupled Plasma-Optical Emission Spectroscopy (ICP-OES) using a Perkin-Elmer Optima 7000 DV ICP-OES instrument.

4.2.6 Growth Inhibition Assay

Antibacterial properties of as-synthesized SLUG-39 and SLUG-40 were evaluated against Escherichia coli (ATCC# 25922) and Staphylococcus epidermidis (ATCC# 12228) using similar methodology as previously reported by Rojas-Andrade *et al*.[12] All experiments were performed with fresh bacteria grown by first spreading frozen liquid culture on a Luria broth (LB) agar plate and incubating at 37 °C for 24 h. A single colony was isolated and used to inoculate 3 mL of LB. The bacterial culture was incubated for 18 h at 37 °C under constant shaking at 250 rpm. A 1 mL aliquot of this bacterial culture was then placed in a 1.5 mL microcentrifuge tube and centrifuged at 5000 rpm for 5 min. The obtained pellet was subsequently re-suspended in 1 mL of sterile nanopure water and this process was repeated an additional two times. Enough of the final re-suspended pellet was added to 5 mL of Nanopure water to adjust its absorbance to 0.100 at 600 nm, referred to as the optical density (OD600). Minimum inhibitory concentrations (MIC) were obtained by performing broth dilution experiments in triplicates. For these experiments, a 96-well plate was utilized, each well filled with 30 μL of sterile LB, 10 μL of the 0.1 OD600 bacterial suspension, varying amounts (100, 90, 80, 70, 60, 50 and 40 μL) of the antimicrobial material and enough Nanopure water to bring the final volume to 200 μL. The final concentration of the antimicrobial agents was determined based on total zinc content. Once the wells were inoculated and all components added, the 96-well plate was immediately placed in a Molecular Devices VERSAmax microplate reader and the optical density for each well was measured at 600 nm every 5 min over the 24 h incubation period, with 10 s mixing periods between reads at 37 °C.

4.2.7 Agar Diffusion Tests

The bacterial inoculums were prepared in a similar fashion as above, with the final suspension adjusted to 0.100 optical density. A 100 μL aliquot of this suspension was then placed on the surface of each LB agar plate and evenly spread using silica glass beads. The antibacterial agents were then placed on top of the agar plates in the form of a circular pellet consisting of 70% KBr and 30% sample and evaluated based on their total zinc content using a pure KBr pellet as a control. The zone of inhibition (ZOI) diameter for each sample was measured with a vernier caliper after a 24 h incubation period at 37 °C, which was also performed in triplicate.

4.2.8 Fluorescence Microscopy

The suspensions of *Escherichia coli* and *Staphylococcus epidermidis* used for imaging were prepared by rinsing overnight liquid cell cultures with nanopure water as described above, excluding the final dilution to 0.100 optical density. The rinsed suspension was then incubated with 5 µM CellROX Green and 10 µM propidium iodide for 30 min in the dark. These dye-incubated cells were then centrifuged and re-suspended in 100 µL of antimicrobial materials, from which a 2 µL drop was taken and placed onto a microscope cover slip (0.17 mm thickness) for fluorescence imaging. A Solamere Spinning disk confocal microscope equipped with a Nikon TE2000 inverted stand, a CSU-X1 spinning disk and a Hamamatsu Image EMX2 camera using Micro-manager software was utilized to obtain all images. A 60x Nikon Plan Apo was utilized as the objective lens. A 488 nm laser with a 500-550 nm band-pass emission filter, and a 561 nm laser with a 573-613 nm band pass filter were used as the excitation sources for CellROX Green and propidium iodide, respectively. Bacterial suspensions were imaged at 1 frame per second for a total of 10 min with 100 ms exposure time for each laser.

4.3 Results and Discussion

4.3.1 Structural Properties of SLUG-39

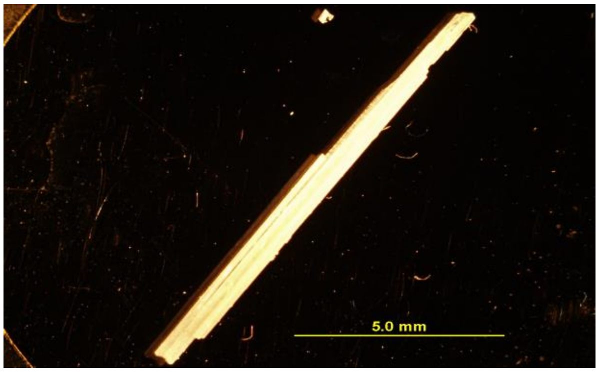

Figure 4.1 Optical micrograph of SLUG-39 crystals.

Large white needle crystals of SLUG-39 were obtained by the hydrothermal reaction of zinc nitrate in the presence of 4,4-bipy and perchlorate ions at 150 °C (Figure 4.1). The crystal structure of SLUG-39 was authenticated by single crystal X-ray diffraction and both the smallest repeat unit and extended structure are shown in Figures 4.2 and 4.3a, respectively. PXRD of the as-synthesized SLUG-39 confirms the material is single phase and matches the theoretical pattern based on the single-crystal solution (Figure 4.4). This coordination polymer crystallizes in a triclinic form with a space group P-1 (Table 1). The two crystallographically independent Zn^{2+} centers have an octahedral coordination environment, with four terminal water molecules in a square-planar arrangement. Two trans nitrogens from two μ-2 bridging 4,4'-bipy units complete the coordination sphere, forming a cationic secondary building unit counterbalanced by two perchlorate groups. The two Zn^{2+} centers and 4,4'-bipy linkers form chains (Figure 4.3a), which are separated by perchlorate anions and perpendicular π-stacked pairs of 4,4'-bipy. The 4,4'-bipy pairs are found in two different conformations, both exhibiting π-stacking (3.420 to 3.750 Å). Several moderate classical hydrogen bonding interactions consolidated the extended lattice of SLUG-39. Some notable interactions are, O(coordinated H_2O)-H---N(bpy), with O---N, 2.723(8), 2.714(8), 2.740(8) Å; O(coordinated H_2O)-H---O(ClO_4), with O---O, 2.808(8) and 2.914(13) Å; O(lattice H_2O)-H---O(coordinated water), with O---O, 2.726(9) and 2.877(11) Å.

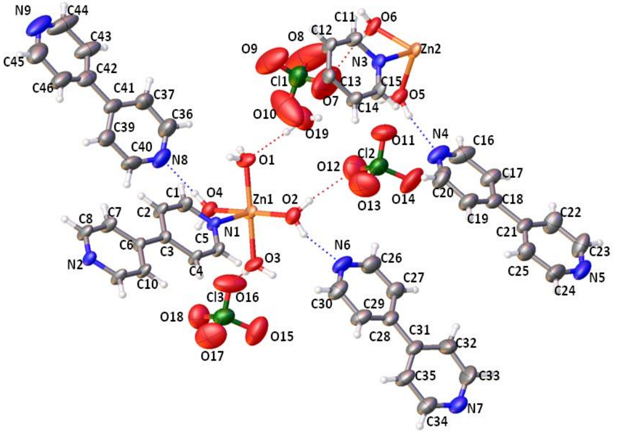

Figure 4.2 ORTEP diagram and atomic labeling of SLUG-39. Thermal ellipsoids are shown at 50% probability.

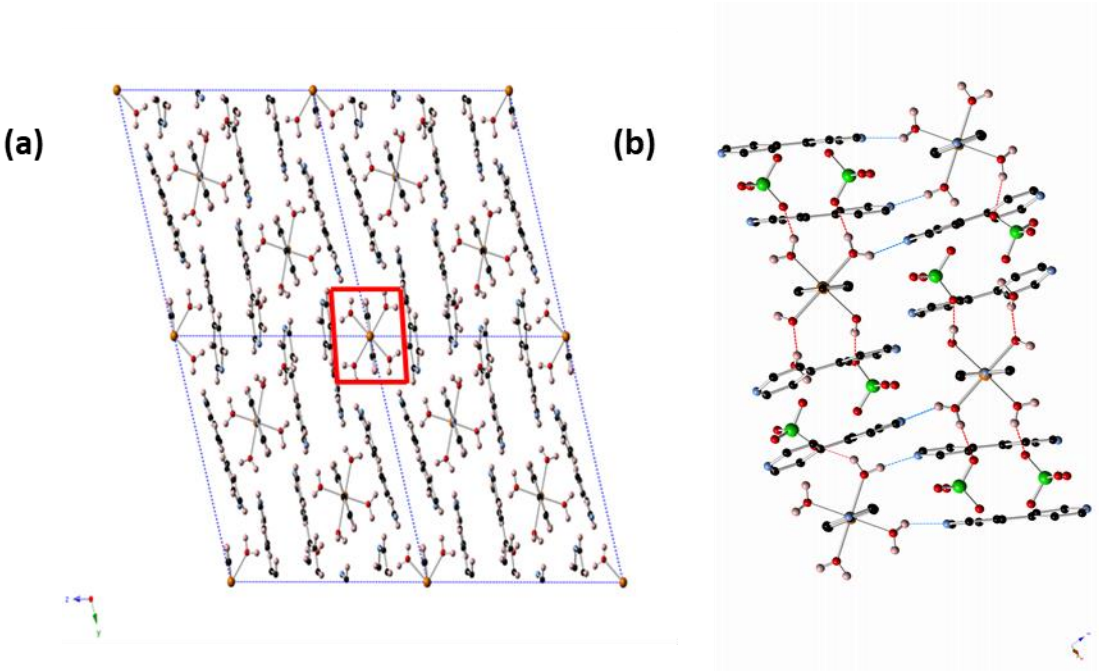

Figure 4.3 (a) Extended structure of SLUG-39 showing the water-terminated polymeric chains end-on (one example is outlined in red) that propagate along the *x* direction; free perchlorate and water molecules are omitted for clarity. (b) Extended structure of SLUG-39 depicting the hydrogen bonding interaction (dashed blue lines) between the terminal waters of the chains and the free waters and neighboring free 4,4'-bipy molecules. (Zn: orange; N: blue; O: red; C: black; H: white).

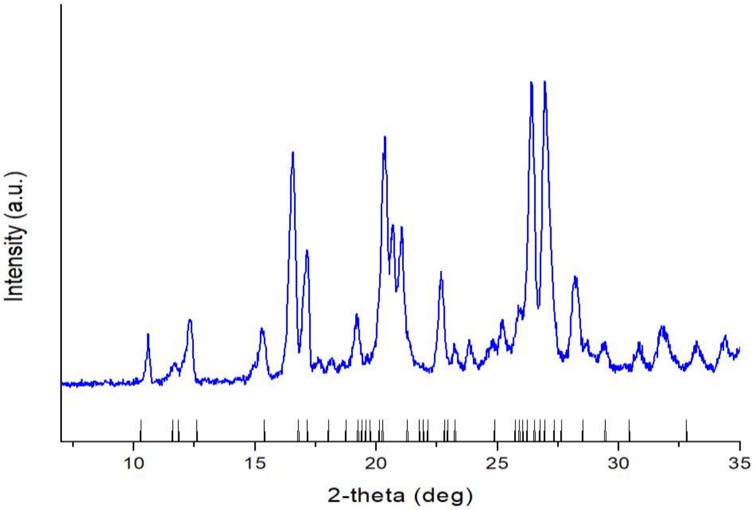

Figure 4.4 PXRD of as-synthesized SLUG-39. The theoretical peaks based on the single crystal structure solution are shown as bars at the bottom.

Three perchlorate molecules counterbalance the cationic chains by electrostatic interactions that result in long Zn-O distances of 4.223(1) and 4.555(7) Å. The perchlorates also provide additional stability *via* hydrogen bonding interactions with three Zn-coordinated water groups (Figure 4.3b). Other coordination polymers with coplanar 4,4'-bipy units include $Co(NCS)_2(H_2O)_2(4,4'\text{-bipy})\cdot 4,4'\text{-bipy}$[32] and $Zn(4,4'\text{-bipy})_2(H_2O)_2SiF_6$.[33] Finally, a crystallographically identified non-coordinated water resides between the perchlorate groups, further stabilizing the structure by hydrogen bonding to a coordinated water group [O···H-O distance 1.917(1) Å]. Thermogravimetric analysis (Figure 4.5) confirms the presence of occluded water in the structure by the initial mass loss of 1.5% around 30 °C, followed by a ~ 9.0% (8.8% theoretical) mass loss corrresponing to the coordinated water groups around 120 °C. The next event corresponds to a two-step decomposition of the 4,4'-bipy groups, in which an initial 1.5 molar equivalents decompose at ~ 210 °C representing an 18.5% mass loss (19.1% theoretical). Finally, the decomposition of the 3.0 molar equivalents of interlamellar 4,4'-bipy units occurs at ~ 300 °C, accounting for a 39% mass loss (38.2% theoretical).[32]

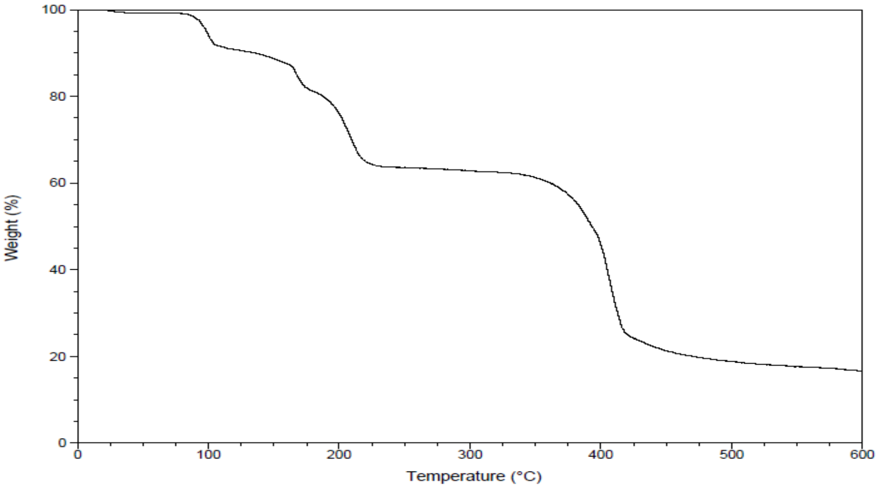

Figure 4.5 Thermogravimetric analysis of SLUG-39 from 25 to 600 °C.

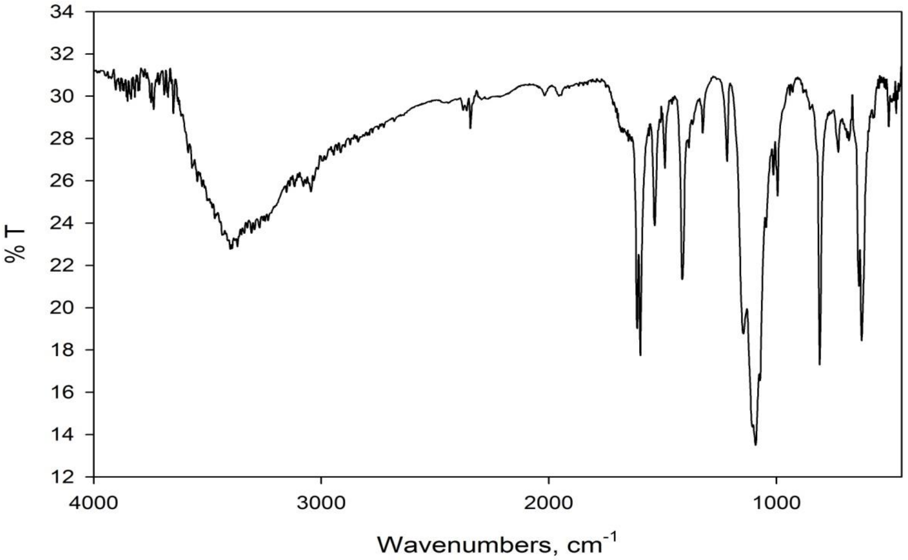

Figure 4.6 FTIR spectrum of as-synthesized SLUG-39.

The IR spectrum confirms the presence of both the polymeric and free interchain 4,4'-bipy units in the structure (Figure 4.6). We attribute the aromatic C=N stretches at 1605 and 1535 cm^{-1} to the linking units and the additional stretch at 1617 cm^{-1} to the uncoordinated units.[34] The presence of perchlorate is verified by the characteristic stretch at 1095 cm^{-1} and the coordination of zinc can be seen by the low frequency stretch at 476 cm^{-1} due to the Zn-N bond.[26]

4.3.2 Structural Properties of SLUG-40

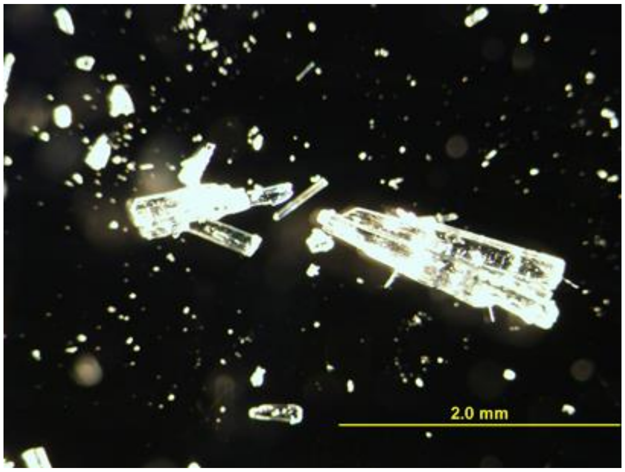

Figure 4.7 Optical micrograph of SLUG-40 crystals.

Small tan flake crystals of SLUG-40 were obtained by the hydrothermal reaction of zinc acetate in the presence of 4,4'-bipy and perchlorate at 150 °C (Figure 4.7). In contrast to SLUG-39, SLUG-40 is a two-dimensional cationic MOF due to the acetate of the zinc reagent rather than nitrate. There are two unique Zn centers. Zn(1) has a trigonal bipyramidal geometry axially coordinated by two 4,4'-bipy units, resulting in an infinite polymeric chain with alternating Zn and 4,4'-bipy units in the crystallographic *b*-direction (Figure 4.8a). Zn(1) is coordinated along [10-1] by an additional μ-2 4,4’-bipy that further bridges two Zn(1) centers of neighboring polymers, as well as two η-2 bridging acetates that connect Zn(1) to Zn(2). In contrast, Zn(2) is octahedral, coordinated by two 4,4'-bipy units, giving rise to infinite connectivity along the *b*-direction (Figure 4.9). The other four coordination sites of Zn(2) correspond to the aforementioned bridging acetates that connect two Zn(1) centers along [10-1] (Figure 4.8b). The four acetate groups allows for Zn(2) to bridge two Zn(1) centers, giving rise to a layer of repeated Zn(1)-Zn(2)-Zn(1) trimer units (red box, Figure 4.8b). These three polymers are thus parallel and the neighboring 4,4'-bipy units are π-stacked with distances of 3.525(1) and 3.787(1) Å along [10-1]. The perchlorate anions reside in the channels and counterbalance the cationic chains [Zn-O distances 5.341(1) and 5.469(1) Å]. PXRD of the as-synthesized SLUG-40 confirms the material is single phase and matches the theoretical pattern based on the single-crystal solution (Figure 4.10). No classical hydrogen bonding interactions have been noted for SLUG-40 structure.

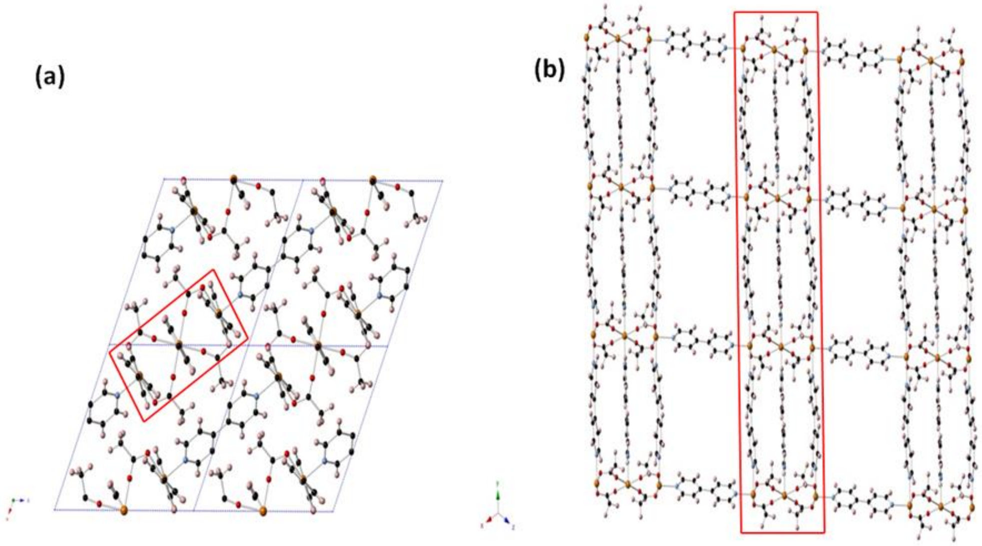

Figure 4.8 (a) Extended structure of SLUG-40 showing polymeric chains along the y-axis with perchlorate and water molecules omitted for clarity; (b) Extended view of one layer of the SLUG-40 framework. The red outline highlights one set of three parallel, acetate-bridged polymers.

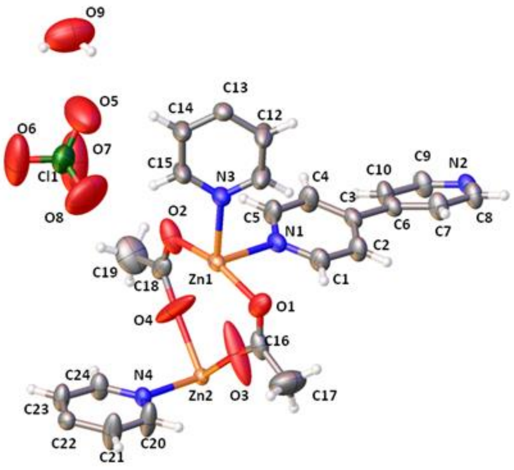

Figure 4.9 ORTEP diagram and atomic labeling of SLUG-40. Thermal ellipsoids are shown at 50% probability.

The IR data confirms the two coordination environments around the two zinc centres. The C-O$^-$ stretch at 1408 cm^{-1} corresponds to the acetate bridging ligand and the low frequency stretches at 510 and 409 cm^{-1} correspond to Zn-O and Zn-N, respectively (Figure 4.11).[26] In addition, the C=N stretches at 1605 and 1581 cm^{-1} are attributed to the 4,4'-bipy units. The perchlorate anions counter-balancing the cationic structure are confirmed by the characteristic singlet stretch at 1061 cm^{-1}. Thermogravimetric analysis (Figure 4.12) reveals an initial mass loss of ~ 2.5% at 85 °C, corresponding to the occluded water (2.5% theoretical). The acetate bridging groups are lost around 200 °C, with ~ 19.2% mass loss (18.4% theoretical). Finally, a two-step occurs where 0.5 molar equivalents of the 4,4'-bipy units are evolved at ~ 220 °C, accounting for a 14.2 % mass loss (12.1 % theoretical). Finally, 1.5 molar equivalents of the 4,4’-bipy units decompose at ~ 320 °C with 34.3% mass loss (36.2% theoretical).

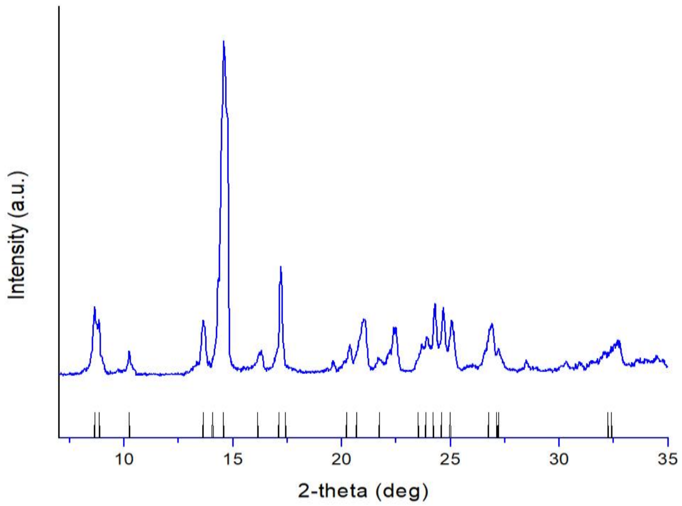

Figure 4.10 PXRD of as-synthesized SLUG-40. The theoretical peaks based on the single crystal structure solution are shown as bars at the bottom.

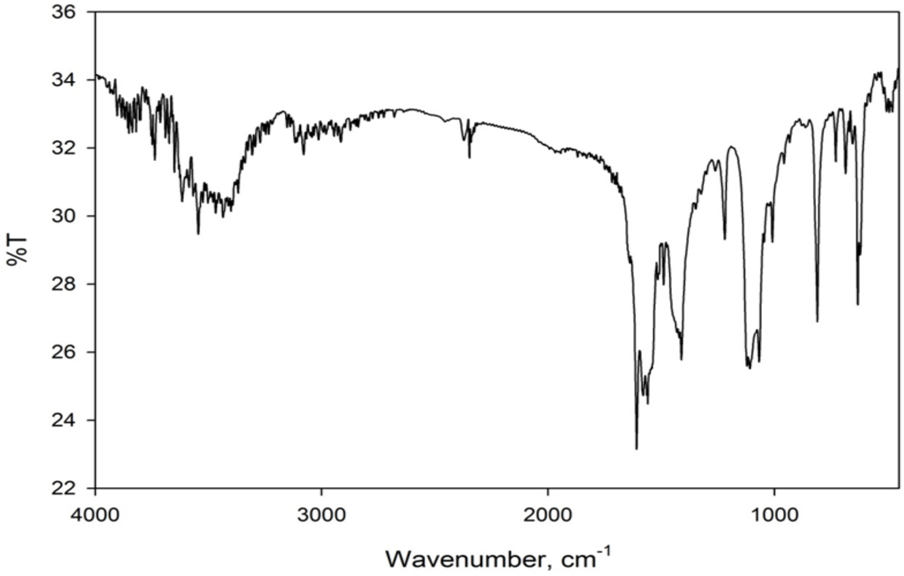

Figure 4.11 FTIR spectrum of as-synthesized SLUG-40.

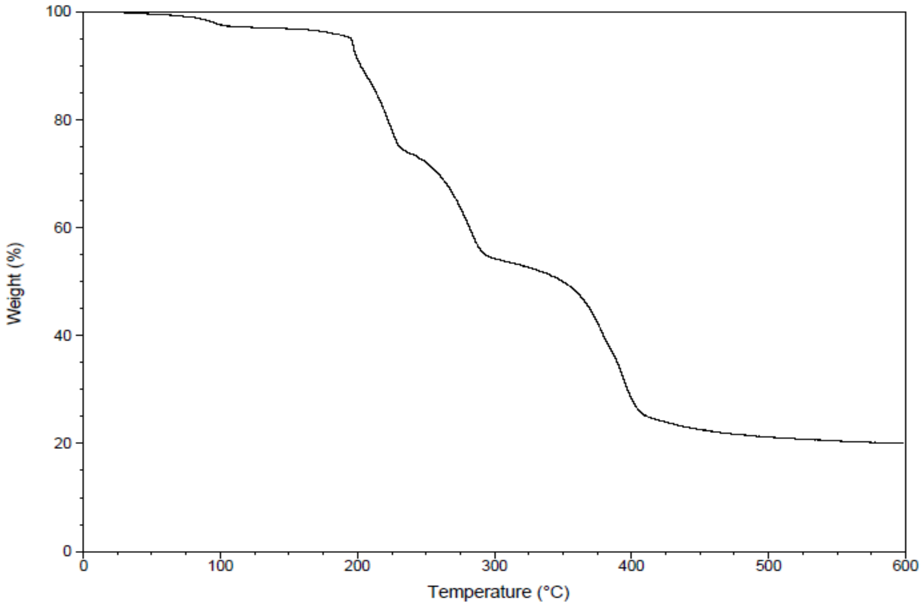

Figure 4.12 Thermogravimetric profile of SLUG-40.

Table 4.1 Crystal data and structure refinement of SLUG-39 and SLUG-40

	SLUG-39	**SLUG-40**
empirical formula	$C_{45}H_{50}Cl_3N_9O_{19}Zn_{1.5}$	$C_{24}H_{24}ClN_4O_9Zn_{1.5}$
formula weight (g/mol)	1225.34	645.98
wavelength (Å)	0.71073 Mo-Kα	0.71073 Mo-Kα
crystal system	triclinic	triclinic
space group	P-1	P-1
unit cell dimensions	a = 11.3146(6) Å b = 15.217(9) Å c = 17.158(10) Å α =106.412(7) ° β = 98.879(6) ° γ = 105.061(6) °	*a* = 11.3806(104) Å *b* = 11.4717(10) Å *c* = 11.9184(104) Å α =105.855(1) ° *β* =108.975 (1) ° γ = 101.196(1) °
volume ($Å^3$)	2652 (2)	1345.2(2)
Z, calculated density (g/cm^3)	2, 1.535	2, 1.595
absorption coefficient (mm^{-1})	0.926	1.518
crystal size (mm)	0.06 x 0.18 x 0.20	0.15 x 0.20 x 0.25
color of crystal	white	tan
θ range for data collection (deg)	2.5 - 25.0	2.8 - 24.7
index ranges	-12≤ h ≤13, -18≤ k ≤17, -20≤ l ≤ 20	-13 ≤ h ≤ 13, -13≤ k ≤ 13, -13 ≤ l ≤ 13
completeness to θ	89.7 % (θ = 25.097)	98.0% (θ = 24.709)
collected/unique reflections	12113/8480 [R(int) = 0.034]	9444/4493 [R(int) = 0.017]
absorption correction	semi-empirical	semi-empirical
max. and min. transmission	0.7452 and 0.6652	0.7451 and 0.6511
refinement method	full-matrix least-squares on F^2	full-matrix least-squares on F^2
data / restraints / parameters	2101 / 0 / 163	2037 / 0 / 163
goodness of fit on F^2	1.303	1.040
R indices (all data)	R_1 = 0.0677, wR_2 = 0.2064	R_1 = 0.060, wR_2 = 0.1408
Largest diff. peak and hole	0.80 and -0.85 ($e/Å^{-3}$)	1.71 and -1.54 ($e/Å^{-3}$)

4.3.3 Zn^{2+} Release Profiles

One advantage of a material that can release Zn^{2+} ions upon contact with fluids compared to the other bioactive metal ions such as Ag^+ is the high solubility of the Zn^{2+} in the presence of common ions such as chlorides. This greater solubility maintains elevated concentrations of biocidal ions in the environment and allows these ions to make contact with bacterial cells more efficiently. In order to evaluate the ability of both SLUG-39 and SLUG-40 to release ions upon contact with relevant fluids, the degradation of both coordination polymers was investigated in aqueous media at 37 °C. This degradation is expressed as the % Zn^{2+} released compared to the total Zn present in the coordination polymer solid.

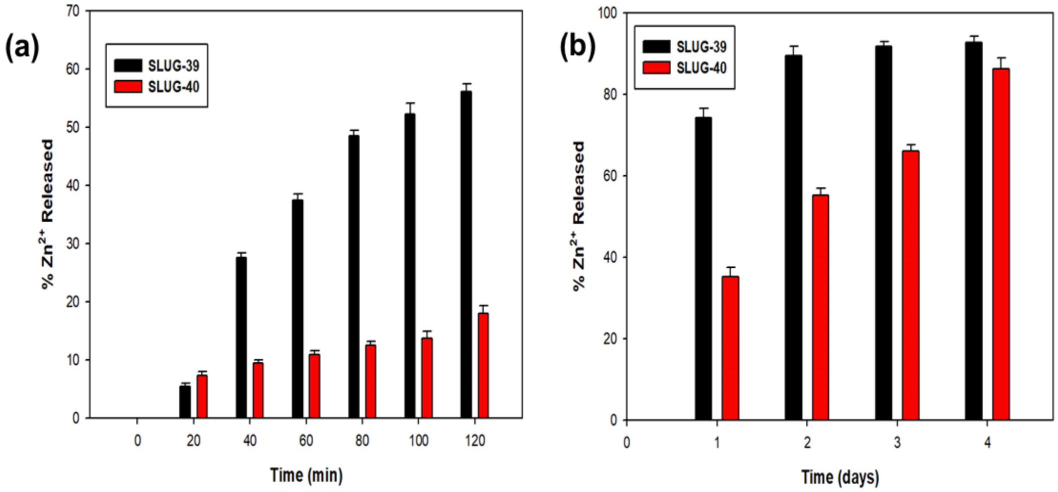

Figure 4.13 Zinc ion release profiles of SLUG-39 and SLUG 40 in distilled water at 37 °C over (a) 120 min and (b) 4 d time intervals.

Careful inspection of the release of Zn^{2+} ions was performed by taking aliquots of the supernatant solution in both 20 min and 1 d intervals and subsequently determining their respective concentrations by ICP-OES. In the first 2 h (Figure 4.13a), SLUG-39 exhibits a significantly greater Zn^{2+} release rate than SLUG-40, with approximately 50 % of Zn^{2+} ions released into solution. The faster release of ions can be attributed to the lower stability of the one-dimensional coordination polymer, held together primarily by hydrogen bonding and weaker π-stacking interactions. Conversely, SLUG-40 exhibits a more sustained release of ions, releasing only *ca*. 15% of the Zn^{2+} ions in the first 2 h. The slower release of Zn^{2+} ions from SLUG-40 stems from its higher dimensionality layered structure, in which the zinc polymers are found as trimeric units, compared to the discrete polymers coordinated by four terminal water groups in SLUG-39. Interestingly, the long-term release of ions for both coordination polymers equalizes after 4 d at ~ 83 % release (Figure 4.13b). Hence, both SLUG-39 and SLUG-40 can serve as reservoirs of Zn^{2+} ions and have ion release profiles that are suitable for different applications. SLUG-39, which exhibits relatively fast ion release, may be suitable for hospital fixtures or surgical devices that require rapid sterilization upon contact, while SLUG-40 with its slower ion release may be applicable in medical implants and cosmetic products.

4.3.4 Antibacterial Assays

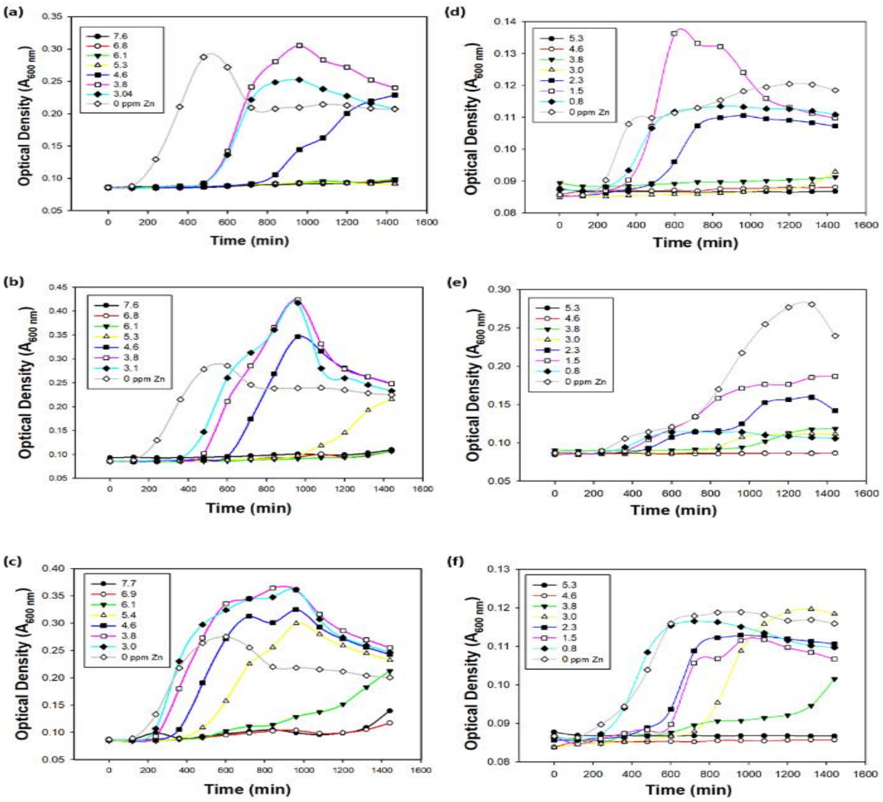

Figure 4.14 Growth curves of E. Coli (a-c) and S. Epidermidis (d-f) in the presence of SLUG-39 (a,d), SLUG-40 (b,e), and $Zn(OAc)_2$ (c,f) at varying concentrations.

The antibacterial properties of the as-synthesized coordination polymers were evaluated against both gram-positive (*Staphylococcus epidermidis*) and gram-negative (*Escherichia coli*) strains. Initially, the biocidal activity of SLUG-39, SLUG-40 and relevant controls was quantified by monitoring the growth of bacterial cultures in liquid media over a 24 h period in the presence of varying concentrations of each biocidal species. Growth curves for both *E. coli* and *S. epidermidis* grown in the presence of each zinc CP as well as with zinc acetate are shown in Figure 4.14. Further, 4,4'-bipy and sodium perchlorate were also investigated to determine their contribution to the biocidal activity of the coordination polymers, but interestingly, no inhibitory effect was observed from these components (Figure 4.15).

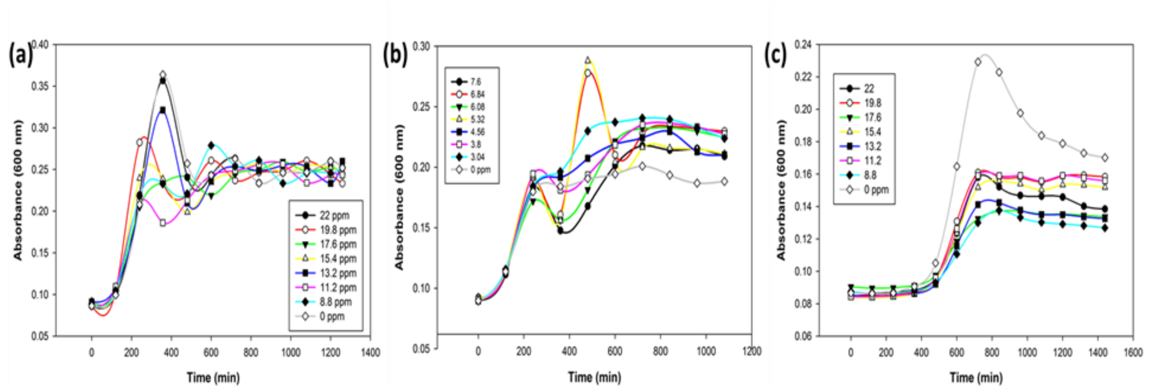

Figure 4.15 Bacterial growth curves of *E. coli* displaying no inhibition in the presence of: (a) 4,4'-bipy; (b) $NaClO_4$; (c) Bacterial growth curves of *S. epidermidis* displaying no inhibition in the presence of 4,4'-bipy.

Due to the difference in zinc composition of the two coordination polymers, their concentrations were normalized to their overall zinc content, allowing for the determination of the minimum inhibitory concentration (MIC) in terms of zinc concentration (Table 2). The MIC represents the concentration at which no bacterial growth is observed during the incubation period, as indicated by the lack of optical density at 600 nm above the baseline value. Based on these growth curves, it is evident that both SLUG-39 and SLUG-40 exhibited an enhanced inhibitory effect on the growth of *E. coli* and *S. epidermidis* with respect to the zinc acetate control. In the case of *E. coli*, SLUG-39 and SLUG-40 displayed an MIC of 5.3 and 6.1 ppm, respectively, markedly lower than $Zn(OAc)_2$ which only showed complete inhibition above 7.7 ppm. Interestingly, MIC values were found to be lower against *S. epidermidis*, with SLUG-39, SLUG-40, and $Zn(OAc)_2$ demonstrating MICs of 3.8, 4.6 and 4.6 ppm, respectively. Further, the lag-phase (T_L) durations were determined from the bacterial growth curves to obtain more insight from the growth kinetics. This value represents a measure of the work required for a bacterial colony to adapt to its environment, and it is defined as the as the time between inoculation and initiation of the log phase. As seen on Figure 4.16, the lag-phase durations of the both SLUG-39 and SLUG-40 are noticeably longer than that of zinc acetate due to the bacterial cells requiring longer periods of time to achieve optimal conditions for replication.

Table 4.2 MIC values of SLUG-39, SLUG-40 and the $Zn(OAc)_2$

Compound	***E. coli*** MIC (ppm)*	***S. epidermidis*** MIC (ppm)*
SLUG-39	5.3	3.8
SLUG-40	6.1	4.6
$Zn(OAc)_2$	6.9	4.6

*Concentration in terms of overall zinc content.

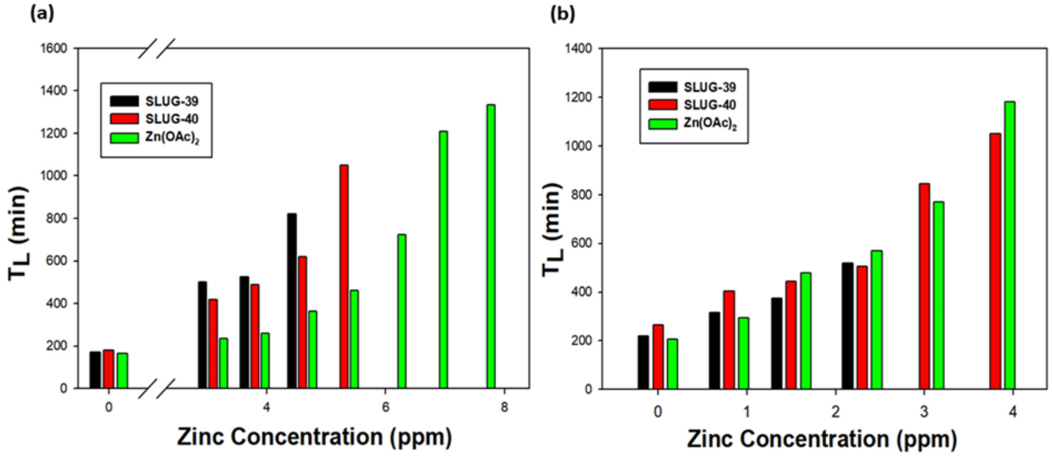

Figure 4.16 Bar chart summarizing lag phase durations (T_L) of: (a) *E. coli* and (b) *S. epidermidis*; at varying concentrations of SLUG-39, SLUG-40, and $Zn(OAc)_2$ normalized by their zinc content.

These results are in agreement with previous findings[20,35,36] and suggests *Staphylococcus* species are more susceptible to zinc toxicity, contrary to the traditionally accepted activity based on differences between gram-positive and gram-negative cell wall structures. Indeed, gram-positive cell walls consist of a much thicker layer of peptidoglycan than gram-negative cell walls, typically affording enhanced protection from environmental stressors compared to gram-negative.[37] Due to the unique chemistry of the Zn^{2+} ion however, the constituents of gram-positive cell walls—teichioic acids (TA) and lipoteichioic acids (LTA), which makeup a significant fraction of the overall mass—are more susceptible to damage by this species. Zn^{2+} ions are known to catalyze the hydrolysis of esters,[38,39] phosphodiesters[40] and amides,[41] all of which are structurally significant functional groups in both TA/LTA and peptidoglycan biomolecules. Therefore, the enhanced activity towards *S. epidermidis* can reasonably be attributed to the membrane damage caused by Zn^{2+} species resulting from the degradation of the CP. This damage may occur as a result of the catalytic hydrolysis of phosphodiester and amide bonds that make up the backbones of TA/LTA molecules, which may crosslink with peptidoglycan units. Gram-negative *E. coli* cells on the other hand, have an extra (outer) membrane which contain molecules of lipopolysaccharide (LPS) that acts as a hydrophobic barrier against Zn^{2+} ions. This barrier cannot be readily disrupted by Zn^{2+} ions, as these molecules lack ester and phosphodiester linkages between the subunits of their structure and instead have glycosidic bonds, for which Zn^{2+} species are ineffective at cleaving.[42] In fact, it has been shown that divalent cations act to electrostatically crosslink LPS molecules, transforming the outer-membrane into a low-permeability barrier which could serve to protect the cell.[43]

In addition, the Zn^{2+} ions can exert their toxicity by competition for essential extracellular cations, i.e. Mn^{2+}, which may lead to oxidative stress.[23,44] Although all three samples are sources of Zn^{2+}, the two CPs still demonstrated lower MICs than zinc acetate (6.9 ppm), a standard free form of Zn^{2+} ions. This result indicates that the coordination polymers have additional structural properties that attribute them a higher antibacterial activity. This greater activity can be due to both their gradual Zn^{2+} release as well as their Zn^{2+} coordination structure. Upon contact with water, the CPs take on a net positive charge that is likely attracted to the net negatively-charged bacterial cell surfaces, affording localized release of Zn^{2+} ions. Bipyridine ligands have been previously incorporated into complexes as well as studied on their own for their biocidal activity. Their observed activity was concluded to arise from both its metal coordinating behavior as well as its ability to make cells aggregate.[45-47] Hence, the 4,4'-bipy units may synergistically add to the biocidal activity by facilitating the aggregation of cells around the CPs, further localizing and concentrating Zn^{2+} ions around bacterial cells. In fact, it has been reported that the antimicrobial effect of Zn^{2+} ions on *E. coli* is dependent on the concentration as well as the contact duration, which plays a significant role in the biocidal activity, as is the case with our two CPs.[21]

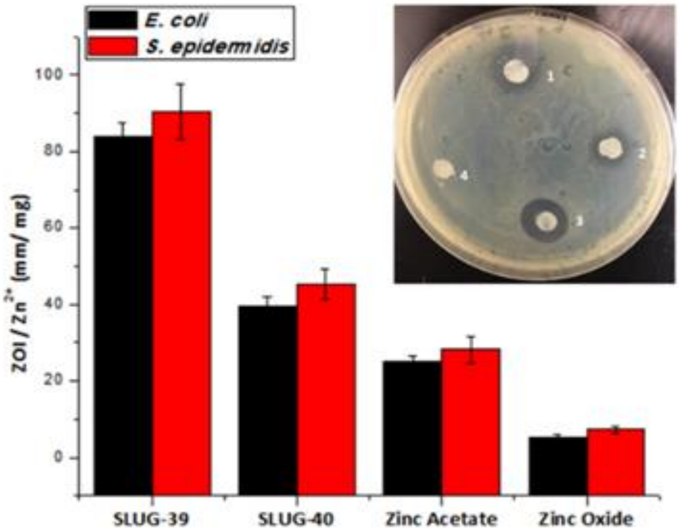

Figure 4.17 Bar chart of normalized zones of inhibition (ZOI) of *E. coli* and *S. epidermidis*, and photograph of a typical agar plate with *E. coli* lawn displaying ZOIs upon treatment with: (1) SLUG-39; (2) SLUG-40; (3) $Zn(OAc)_2$; (4) ZnO.

The antibacterial activity of the coordination polymers was also investigated in their solid form by performing agar diffusion tests and determining the resultant zones of inhibitions. In order to accurately compare the activity of each of the antibacterial agents, the diameters of inhibition zones were normalized to total zinc content of the structure (Figure 4.17). Similar results were obtained for *E. coli* and *S. epidermidis*, with SLUG-39 exhibiting the largest ZOI, followed by SLUG-40. Both demonstrated superior activity to $Zn(OAc)_2$ and especially ZnO. Further, *S. epidermidis* exhibited a higher susceptibility to the biocidal effects of Zn antibacterial agents than *E. coli*, in agreement with the broth dilution assays.

The superior activity from the CPs compared to zinc acetate and ZnO is likely due to a combination of gradual and sustained release of Zn^{2+} ions from the slow degradation of these crystalline materials as well as their mobility through the agar media. Upon degradation, SLUG-39 forms long chains which likely have a much higher mobility through the pores of the agar than the 2-D layers of SLUG-40 accounting for the observed differences in ZOI. Unlike the highly soluble zinc acetate salt that leads to immediate dissolution and sequestering of Zn^{2+} ions by the functional groups of the agar substrate, the gradual release from the CPs provides a more localized and concentrated form of biocidal Zn^{2+} ions. This localization likely enhances internalization into bacterial cells, leading to enhanced disruption of membrane structure and cation homeostasis.[48,49] ZnO was observed to exhibit the lowest inhibition for both bacterial strains due to its low solubility in aqueous environments. In addition, the activity of the individual components of the CPs as well as a KBr control were investigated. Of these, only the 4,4'-bipy ligand exhibited a zone of inhibition (Figure 4.18), which was relatively minimal compared with the other samples. This result suggests the linker alone does not contribute significantly to the biocidal activity, which is also in agreement with the broth dilution experiments.

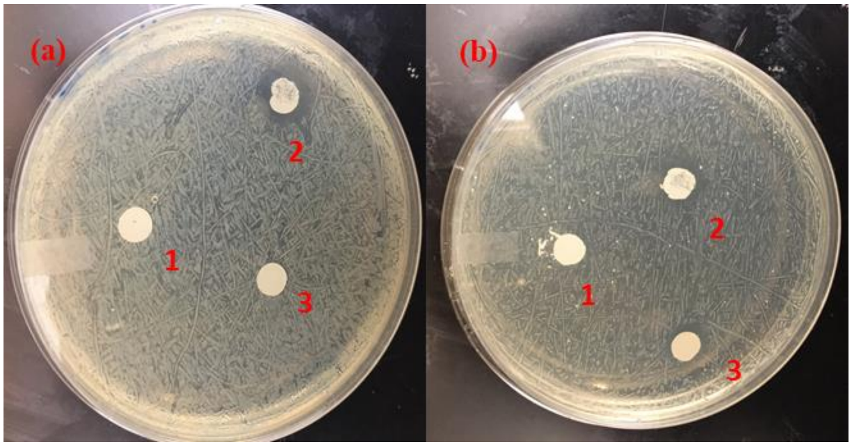

Figure 4.18 Agar diffusion test of: (a) *E. coli*; (b) *S. epidermidis*, treated with: (1) KBr; (2) 4,4'-bipy; (3) $NaClO_4$.

4.3.5 Fluorescence Microscopy

The mechanism of the biocidal activity that SLUG-39 and SLUG-40 demonstrate against *S. epidermidis* was further investigated *in vivo* utilizing fluorescence microscopy, with CellRox Green and propidium iodide. CellRox Green indicates the formation of hydroxyl radicals and superoxide anions which result from oxidative stress undergone by the cell emitting fluorescence at 520 nm. Propidium iodide is used to evaluate cell membrane integrity, as indicated by the fluorescence emission at 636 nm upon intercalation of DNA in the event of entry into bacterial cells due to membrane damage. Bacterial cells were suspended in freshly-prepared solutions of the coordination polymers or zinc acetate at a concentration of 15.2 ppm by zinc content, as well as pure water as a control. The cells resuspended in water demonstrated a minimal relative fluorescent cell count of both dyes over a period of 10 min (Figure 4.19).

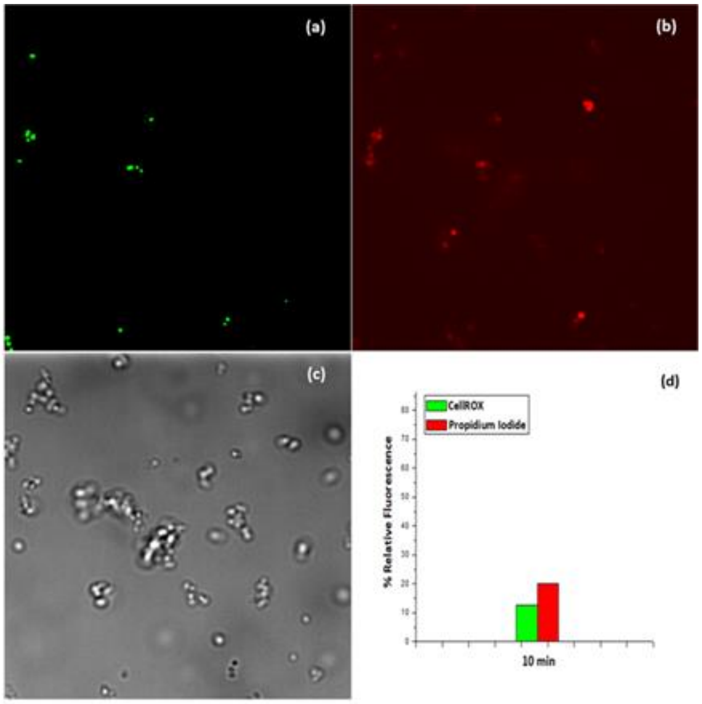

Figure 4.19 Fluorescence microscopy images of *S. epidermidis* incubated with 5 µM CellROX Green and 10 µM propidium iodide in water after 10 min: (a) 488 nm excitation, 500-550 emission; (b) 561 nm excitation, 573–613 nm emission; (c) Bright-field channel; (d) Relative fluorescence from CellROX Green and propidium iodide.

Interestingly, however, treatment of *S. epidermidis* with SLUG-39, SLUG-40, and zinc acetate resulted in a pronounced increase in fluorescent cells, with a gradual change from green to red fluorescence observed over 10 minutes (Figure 4.20). The cells treated with zinc acetate initially exhibited the highest CellRox fluorescence cell count, with 3 and 6 times more green cells observed than SLUG-39 and SLUG-40, respectively (Figure 4.21a). This greater count indicates that a high level of oxidative stress was being caused in affected cells, likely due to the fast release of Zn^{2+} ions causing elevated ROS generation. This fast release likely results in a relatively high concentration of intercellular Zn^{2+}, causing rapid disruption of metabolic activity through extracellular cation competition, subsequently causing this oxidative stress. After three minutes of exposure, however, both CPs demonstrated a much more comparable number of green fluorescent cells. This observation correlates well with their zinc-release profiles and suggests the oxidative stress is directly related to free Zn^{2+}.

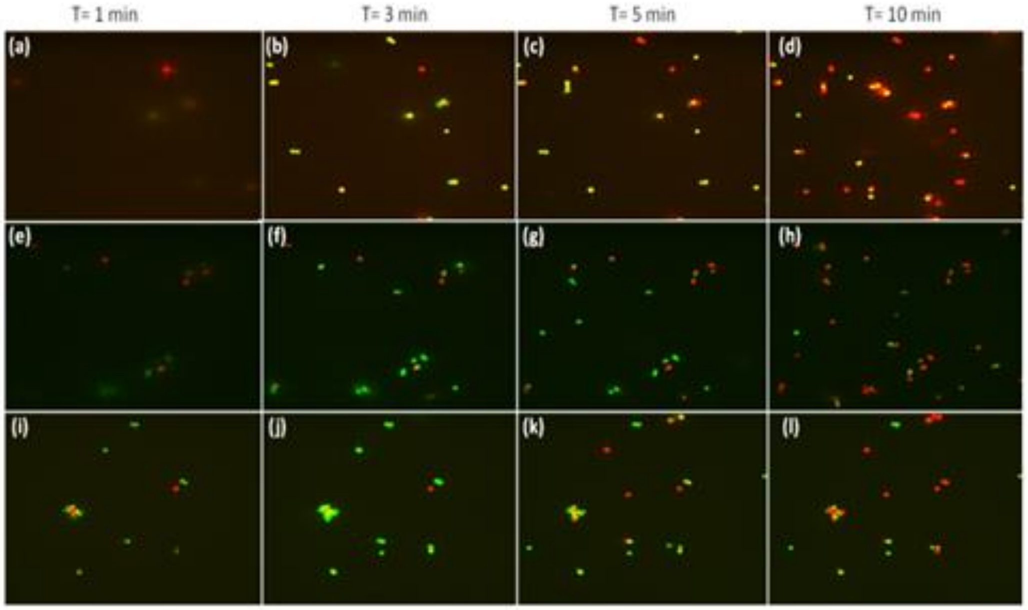

Figure 4.20 Fluorescence micrographs of *S. epidermidis* incubated with 5 µM CellROX Green and 10 µM propidium iodide and treated with: (a-d) SLUG-39; (e-h) SLUG-40; (i-l) $Zn(OAc)_2$ over a 10-minute period.

As the contact time increases, the cells begin experiencing membrane damage as seen by the gradual increase in the number of red fluorescing cells (Figure 4.21b). After the first minute, all samples have a similar percentage of red fluorescent cells. SLUG-39, however, observes the highest count of these cells at every time point proceeding, with both CPs observing higher counts than zinc acetate after 10 min. This higher count can be explained by the ability of the CP to wrap around and generally localize themselves to bacterial cell surfaces, with both the 4,4'-bipy units and the localized release of Zn^{2+} ions contributing to the enhanced membrane damage activity. SLUG-39, having both 4,4'-bipy and Zn^{2+} moieties that are easily released, optimally enhances interactions of CP units with bacterial cells and facilitates Zn^{2+} toxicity, respectively.

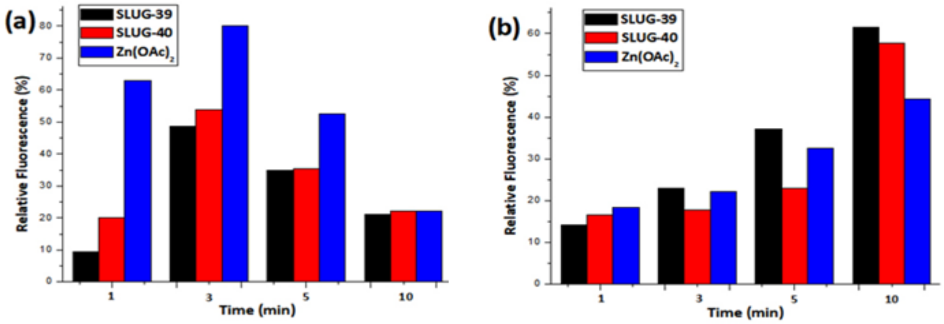

Figure 4.21 Relative fluorescence of *S. epidermidis* cells in the presence of SLUG-39 (black), SLUG-40 (red) and $Zn(OAc)_2$ (black), incubated with: (a) CellROX; (b) propidium iodide.

4.4 Conclusions

Two crystalline CP materials have demonstrated enhanced antibacterial activities in both liquid and solid growth media compared with typical Zn sources. *In vivo* studies utilizing fluorescence microscopy suggest that both materials induce cell death by oxidative stress and membrane damage resulting from Zn^{2+} toxicity. The enhanced biocidal properties of these CPs are likely due to gradual and localized release of Zn^{2+} ions, likely resulting from enhanced electrostatic interactions with bacterial cell surfaces afforded by their unique coordination structure. This study demonstrates how careful manipulation of zinc-based extended structures could provide low cost, Earth abundant and highly bioactive materials that are promising candidates for controlling bacterial growth in many situations such as in healthcare, cosmetic and food environments.

4.5 References

(1) Ling, L. L.; Schneider, T.; Peoples, A. J.; Spoering, A. L.; Engels, I.; Conlon, B. P.; Mueller, A.; Schäberle, T. F.; Hughes, D. E.; Epstein, S.; Jones, M.; Lazarides, L.; Steadman, V. A.; Cohen, D. R.; Felix, C. R.; Fetterman, K. A.; Millett, W. P.; Nitti, A. G.; Zullo, A. M.; Chen, C.; Lewis, K. A New Antibiotic Kills Pathogens without Detectable Resistance. *Nature* **2015**, *517* (7535), 455–459.

(2) *Antimicrobial Resistance: Global Report on Surveillance*; World Health Organization, Ed.; World Health Organization: Geneva, Switzerland, 2014.

(3) Blair, J. M. A.; Webber, M. A.; Baylay, A. J.; Ogbolu, D. O.; Piddock, L. J. V. Molecular Mechanisms of Antibiotic Resistance. *Nat. Rev. Microbiol.* **2014**, *13* (1), 42–51.

(4) Wu, C.; Labrie, J.; Tremblay, Y. D. N.; Haine, D.; Mourez, M.; Jacques, M. Zinc as an Agent for the Prevention of Biofilm Formation by Pathogenic Bacteria. *J. Appl. Microbiol.* **2013**, *115* (1), 30–40.

(5) Feng, Q.; Wu, J.; Chen, G.-Q.; Cui, F.-Z.; N. Kim, T.; O. Kim, J. *A Mechanistic Study of the Antibacterial Effect of Silver Ions OnEscherichia Coli AndStaphylococcus Aureus*; 2000; Vol. 52.

(6) Uruş, S.; Serindağ, O.; Diğrak, M. Synthesis, Characterization, and Antimicrobial Activities of Cu(I), Ag(I), Au(I), and Co(II) Complexes with [CH3N(CH2PPh2)2]. *Heteroat. Chem.* **2005**, *16* (6), 484–491.

(7) Patel, K. M.; Patel, K. N.; Patel, N. H.; Patel, M. N. SYNTHESIS, CHARACTERIZATION, AND ANTIMICROBIAL ACTIVITIES OF SOME TRANSITION METAL COMPLEXES WITH A TRIDENTATE DIBASIC SCHIFF BASE AND BIDENTATE 2,2′-BIPYRIDYLAMINE. *Synth. React. Inorg. Met.-Org. Chem.* **2001**, *31* (2), 239–246.

(8) Golcu, A.; Tumer, M.; Demirelli, H.; Wheatley, R. A. Cd(II) and Cu(II) Complexes of Polydentate Schiff Base Ligands: Synthesis, Characterization, Properties and Biological Activity. *Inorganica Chim. Acta* **2005**, *358* (6), 1785–1797.

(9) Dizaj, S. M.; Lotfipour, F.; Barzegar-Jalali, M.; Zarrintan, M. H.; Adibkia, K. Antimicrobial Activity of the Metals and Metal Oxide Nanoparticles. *Mater. Sci. Eng. C* **2014**, *44*, 278–284.

(10) Huh, A. J.; Kwon, Y. J. "Nanoantibiotics": A New Paradigm for Treating Infectious Diseases Using Nanomaterials in the Antibiotics Resistant Era. *J. Controlled Release* **2011**, *156* (2), 128–145.

(11) Wyszogrodzka, G.; Marszałek, B.; Gil, B.; Dorożyński, P. Metal-Organic Frameworks: Mechanisms of Antibacterial Action and Potential Applications. *Drug Discov. Today* **2016**, *21* (6), 1009–1018.

(12) Rojas-Andrade, M.; Cho, A. T.; Hu, P.; Lee, S. J.; Deming, C. P.; Sweeney, S. W.; Saltikov, C.; Chen, S. Enhanced Antimicrobial Activity with Faceted Silver Nanostructures. *J. Mater. Sci.* **2015**, *50* (7), 2849–2858.

(13) Morones, J. R.; Elechiguerra, J. L.; Camacho, A.; Holt, K.; Kouri, J. B.; Ramírez, J. T.; Yacaman, M. J. The Bactericidal Effect of Silver Nanoparticles. *Nanotechnology* **2005**, *16* (10), 2346–2353.

(14) Li, W.-R.; Xie, X.-B.; Shi, Q.-S.; Zeng, H.-Y.; OU-Yang, Y.-S.; Chen, Y.-B. Antibacterial Activity and Mechanism of Silver Nanoparticles on Escherichia Coli. *Appl. Microbiol. Biotechnol.* **2010**, *85* (4), 1115–1122.

(15) Lu, Z.; Rong, K.; Li, J.; Yang, H.; Chen, R. Size-Dependent Antibacterial Activities of Silver Nanoparticles against Oral Anaerobic Pathogenic Bacteria. *J. Mater. Sci. Mater. Med.* **2013**, *24* (6), 1465–1471.

(16) Li, X.; Lenhart, J. J.; Walker, H. W. Dissolution-Accompanied Aggregation Kinetics of Silver Nanoparticles. *Langmuir* **2010**, *26* (22), 16690–16698.

(17) Huynh, K. A.; Chen, K. L. Aggregation Kinetics of Citrate and Polyvinylpyrrolidone Coated Silver Nanoparticles in Monovalent and Divalent Electrolyte Solutions. *Environ. Sci. Technol.* **2011**, *45* (13), 5564–5571.

(18) Pappalardo, R.; Marcos, E. Recovering the Concept of the Hydrated Ion for Modeling Ionic Solutions: A Monte Carlo Study of Zn2+ in Water. *J. Phys. Chem* **1993**, *97*, 4500–4504.

(19) Rudolph, W. W.; Pye, C. C. Zinc(II) Hydration in Aqueous Solution. A Raman Spectroscopic Investigation and an Ab-Initio Molecular Orbital Study. *Phys. Chem. Chem. Phys.* **1999**, *1* (19), 4583–4593.

(20) Masoudiasl, A.; Montazerozohori, M.; Naghiha, R.; Assoud, A.; McArdle, P.; Safi Shalamzari, M. Synthesis, X-Ray Crystal Structures and Thermal Analyses of Some New Antimicrobial Zinc Complexes: New Configurations and Nano-Size Structures. *Mater. Sci. Eng. C* **2016**, *61*, 809–823.

(21) Abdel Aziz, A. A.; Badr, I. H. A.; El-Sayed, I. S. A. Synthesis, Spectroscopic, Photoluminescence Properties and Biological Evaluation of Novel Zn(II) and Al(III) Complexes of NOON Tetradentate Schiff Bases. *Spectrochim. Acta. A. Mol. Biomol. Spectrosc.* **2012**, *97*, 388–396.

(22) Constantinidis, J. Treatment of Alzheimer's Disease by Zinc Compounds. *Drug Dev. Res.* **1992**, *27* (1), 1–14.

(23) McDevitt, C. A.; Ogunniyi, A. D.; Valkov, E.; Lawrence, M. C.; Kobe, B.; McEwan, A. G.; Paton, J. C. A Molecular Mechanism for Bacterial Susceptibility to Zinc. *PLoS Pathog.* **2011**, *7* (11), e1002357.

(24) Brayner, R.; Ferrari-Iliou, R.; Brivois, N.; Djediat, S.; Benedetti, M. F.; Fiévet, F. Toxicological Impact Studies Based on *Escherichia Coli* Bacteria in Ultrafine ZnO Nanoparticles Colloidal Medium. *Nano Lett.* **2006**, *6* (4), 866–870.
(25) Bian, S.-W.; Mudunkotuwa, I. A.; Rupasinghe, T.; Grassian, V. H. Aggregation and Dissolution of 4 Nm ZnO Nanoparticles in Aqueous Environments: Influence of PH, Ionic Strength, Size, and Adsorption of Humic Acid. *Langmuir* **2011**, *27* (10), 6059–6068.

(26) Xu, G.-C.; Zhang, L.; Zhang, Y.-H.; Guo, J.-X.; Shi, M.-Q.; Jia, D.-Z. Syntheses, Crystal Structures and Luminescent Properties of Four Zn(Ii) Coordination Polymers with Pyrazolone Derivatives and 4,4′-Bipyridine. *CrystEngComm* **2013**, *15* (15), 2873.

(27) Sumida, K.; Rogow, D. L.; Mason, J. A.; McDonald, T. M.; Bloch, E. D.; Herm, Z. R.; Bae, T.-H.; Long, J. R. Carbon Dioxide Capture in Metal–Organic Frameworks. *Chem. Rev.* **2012**, *112* (2), 724–781.

(28) Karmakar, A.; Joarder, B.; Mallick, A.; Samanta, P.; Desai, A. V.; Basu, S.; Ghosh, S. K. Aqueous Phase Sensing of Cyanide Ions Using a Hydrolytically Stable Metal–organic Framework. *Chem Commun* **2017**, *53* (7), 1253–1256.

(29) Custelcean, R.; Moyer, B. A. Anion Separation with Metal–Organic Frameworks. *Eur. J. Inorg. Chem.* **2007**, *2007* (10), 1321–1340.

(30) Long, J. R.; Yaghi, O. M. The Pervasive Chemistry of Metal–organic Frameworks. *Chem. Soc. Rev.* **2009**, *38* (5), 1213.

(31) Tamames-Tabar, C.; Imbuluzqueta, E.; Guillou, N.; Serre, C.; Miller, S. R.; Elkaïm, E.; Horcajada, P.; Blanco-Prieto, M. J. A Zn Azelate MOF: Combining Antibacterial Effect. *CrystEngComm* **2015**, *17* (2), 456–462.

(32) Lu, J.; Paliwala, T.; Lim, S. C.; Yu, C.; Niu, T.; Jacobson, A. J. Coordination Polymers of Co(NCS) $_2$ with Pyrazine and 4,4‘-Bipyridine: Syntheses and Structures. *Inorg. Chem.* **1997**, *36* (5), 923–929.

(33) Gable, R. W.; Hoskins, B. F.; Robson, R. A New Type of Interpenetration Involving Enmeshed Independent Square Grid Sheets. The Structure of Diaquabis-(4,4′-Bipyridine)Zinc Hexafluorosilicate. *J Chem Soc Chem Commun* **1990**, No. 23, 1677–1678.

(34) Fei, H.; Bresler, M. R.; Oliver, S. R. J. A New Paradigm for Anion Trapping in High Capacity and Selectivity: Crystal-to-Crystal Transformation of Cationic Materials. *J. Am. Chem. Soc.* **2011**, *133* (29), 11110–11113.

(35) Atmaca, S.; Gül, K. The Effect of Zinc on Microbial Growth. *Turk. J. Med. Sci.* **1998**, No. 28, 595–597.
(36) Aarestrup, F. M.; Hasman, H. Susceptibility of Different Bacterial Species Isolated from Food Animals to Copper Sulphate, Zinc Chloride and Antimicrobial Substances Used for Disinfection. *Vet. Microbiol.* **2004**, *100* (1–2), 83–89.

(37) Silhavy, T. J.; Kahne, D.; Walker, S. The Bacterial Cell Envelope. *Cold Spring Harb. Perspect. Biol.* **2010**, *2* (5), a000414–a000414.

(38) Chin, J. Developing Artificial Hydrolytic Metalloenzymes by a Unified Mechanistic Approach. *Acc. Chem. Res.* **1991**, *24* (5), 145–152.

(39) Carrillo, R. M.; Neo, A. G.; López-García, L.; Marcaccini, S.; Marcos, C. F. Zinc Catalysed Ester Solvolysis. Application to the Synthesis of Tartronic Acid Derivatives. *Green Chem* **2006**, *8* (9), 787–789.

(40) Mikkola, S.; Zagorowska, I.; Lönnberg, H. Zn^{2+} Promoted Hydrolysis of RNA. *Nucleosides Nucleotides* **1999**, *18* (6–7), 1267–1268.

(41) Przystas, T. J.; Fife, T. H. The Metal-Ion-Promoted Water- and Hydroxide-Ion-Catalysed Hydrolysis of Amides. *J. Chem. Soc. Perkin Trans. 2* **1990**, No. 3, 393.

(42) Leavell, M. D.; Leary, J. A. Stabilization and Linkage Analysis of Metal-Ligated Sialic Acid Containing Oligosaccharides. *J. Am. Soc. Mass Spectrom.* **2001**, *12* (5), 528–536.

(43) Chatterjee, A. K.; Ross, H.; Sanderson, K. E. Leakage of Periplasmic Enzymes from Lipopolysaccharide-Defective Mutants of *Salmonella Typhimurium*. *Can. J. Microbiol.* **1976**, *22* (10), 1549–1560.

(44) Coelho Abrantes, M.; Lopes, M. de F.; Kok, J. Impact of Manganese, Copper and Zinc Ions on the Transcriptome of the Nosocomial Pathogen Enterococcus Faecalis V583. *PLoS ONE* **2011**, *6* (10), e26519.

(45) Rotaru, A.; Ungureanu, M.; Danac, R.; Poeata, A.; Druta, I. Activité antimicrobienne in vitro de nouveaux sels diquaternaires dérivés de la 4,4’-bipyridine. *Ann. Pharm. Fr.* **2004**, *62* (6), 428–430.

(46) Kaushal, R.; Kumar, N.; Awasthi, P.; Nehra, K. Syntheses, Characterization, and Antibacterial Study of Titanium Complexes. *Turk. J. Chem.* **2013**, *37*, 936–945.

(47) Grenier, M. C.; Davis, R. W.; Wilson-Henjum, K. L.; LaDow, J. E.; Black, J. W.; Caran, K. L.; Seifert, K.; Minbiole, K. P. C. The Antibacterial Activity of 4,4′-Bipyridinium Amphiphiles with Conventional, Bicephalic and Gemini Architectures. *Bioorg. Med. Chem. Lett.* **2012**, *22* (12), 4055–4058.

(48) Wątły, J.; Potocki, S.; Rowińska-Żyrek, M. Zinc Homeostasis at the Bacteria/Host Interface-From Coordination Chemistry to Nutritional Immunity. *Chem. - Eur. J.* **2016**, *22* (45), 15992–16010.

(49) Pasquet, J.; Chevalier, Y.; Pelletier, J.; Couval, E.; Bouvier, D.; Bolzinger, M.-A. The Contribution of Zinc Ions to the Antimicrobial Activity of Zinc Oxide. *Colloids Surf. Physicochem. Eng. Asp.* **2014**, *457*, 263–274.

Chapter 5

Conclusions and Future Work

5.1 Conclusions

The work presented in this thesis contributes to the progress of the application of cationic metal-organic frameworks (MOFs) in the fields of environmental remediation and biomedicine. This class of crystalline materials display a superior performance in the capture of perchlorate, an emerging groundwater pollutant, compared to that of the conventional organic resins and extensively studied LDHs. Further, the careful manipulation of the extended structures of MOFs composed by bioactive metals such as Ag, Zn, and Cu may render a material that can control bacterial growth in many situations including healthcare, cosmetic and food environments.

The cationic MOF SBN [Ag(4,4’-bipy)(NO_3)] demonstrated a high propensity towards perchlorate, which allowed for the design of an efficient perchlorate trapping methodology. The favorable anion exchange reaction is driven due to the weakly bound nitrate anions counterbalancing the $[Ag(I)\text{-bipy}]^+$ chains of SBN, as well as the lower hydration energy of perchlorate. The exchange is completed within 90 minutes at a capacity of 354 mg ClO_4^-/g SBN, representing a 99% removal and resulting in the formation of a new crystal structure, SBP [Ag(4,4’-bipy)(ClO_4^-)]. The perchlorate uptake capacity and kinetics of SBN was superior than that of the conventional anion exchange resins Amberlite IRA-400 (249 mg/g) and Purolite A530E (104 mg/g), as well as the calcined layered double hydroxides Hydrotalcite (28 mg/g). Unlike these conventional exchangers that are typically used for one cycle, the regeneration method of SBN actually takes advantage of the metastability of MOFs by reassembling back into the regenerated form simply using heat and excess nitrate to revert the anion exchange and result in fresh crystals. In addition, SBN exhibits highly selective perchlorate capture in the presence of multiple-fold excess of potentially competing common anions including sulfate, nitrate, and chloride. Hence, this methodology presents a significant advance in the methods available for perchlorate trapping and water purification.

A detailed study of the host-guest interaction during the anion exchange between SBN and SBP was successfully done by closely investigating the structural transformation and flexibility of the $[Ag(I)\text{-bipy}]^+$ polymeric frameworks. The anion exchange dynamics were monitored by using a combination of powder X-ray diffraction (PXRD) with multinuclear ^{13}C, ^{15}N and ^{109}Ag solid-state NMR spectra at different time intervals of the anion exchange. Further, the reaction pathway was confirmed to occur via a solvent-mediated process by inspecting the morphological changes of the two crystalline materials utilizing scanning electron microscopy (SEM). The study provided crucial insights for the rational design of these and related

MOFs toward the selective capture of environmental pollutant oxo-anions such as perchlorate, chromate and arsenate.

The structures of SLUG-39 $[Zn(bipy)(OH_2)_4^{2+}]_{1.5}[ClO_4^-]_3$•$(bipy)_3(H_2O)$ and SLUG-40 $[Zn_{1.5}(CH_3CO_2)_2(bipy)_2^+][ClO_4^-]$•$H_2O$ are unique extended frameworks that were synthesized under hydrothermal conditions and extensively characterized. SLUG-39 consists of a one-dimensional (1D) structure with two crystallographically independent octahedral zinc centers trans-coordinated by two 4,4'-bipy units and water groups, while SLUG-40 is a two-dimensional (2D) layered structure with the same polymers but bridged together into a layer by acetate and 4,4'-bipy. Both compounds exhibit sustained release of Zn^{2+} ions upon their gradual degradation in aqueous solution, which results in highly effective antibacterial activity towards *Escherichia coli* and particularly towards *Staphylococcus epidermidis* cells. *In vivo* studies utilizing fluorescence microscopy suggest that both materials induce cell death by oxidative stress and membrane damage resulting from Zn^{2+} toxicity and in part 4,4'-bipy toxicity. The enhanced biocidal properties of these CPs are likely due to gradual and localized release of Zn^{2+} ions, likely resulting from enhanced electrostatic interactions with bacterial cell surfaces afforded by their unique coordination structure. This unique Zn^{2+} release profile and interaction with bacterial surfaces affords marked antibacterial activity and suggests that manipulation of the Zn^{2+} structures could lead to significant advancements in antimicrobial materials.

5.2 Future Work

The perchlorate trapping methodology involving the anion exchange of SBN and formation of SBP was demonstrated to effectively outperform conventional anion exchangers including organic resins and LDH materials. However, this methodology is currently at a proof-of-concept stage, and several elements need to be further developed in order implement this perchlorate remediation strategy in an industrial setting. One of the first steps to take in a future direction consists of the large scale synthesis of SBN. The material exhibits an excellent yield and purity at the gram scale, but in order to treat plume sites, the material would need to be produced in kilogram scales. Although the synthesis conditions are relatively straightforward, it would be of great interest to investigate if the synthesis is successful at a larger production scale. Further, it would be of great interest to apply the reported methodology with actual polluted water from plume sites in order to evaluate if the material can exert anion exchange effectively at perchlorate concentrations in the ppb range. The perchlorate capture experiments reported in this thesis were done at concentrations ranging from 5–700 ppm in order to evaluate the saturated adsorption capacities. Moreover, by performing future experiments with water from plume sites, the performance of SBN in the presence of various other pollutants including trichloroethylene (TCE) could be investigated. In fact, our group has recently began working with mock pollutant solutions containing both perchlorate and TCE in order to evaluate the performance of various MOFs at capturing both pollutants. One of the main drawbacks and limitations for the industrial use of SBN and many other coordination polymers is their limited solubility in water of 0.80 mmol/L. Although the perchlorate uptake kinetics of SBN are desirable due to its high propensity for this anion, the regeneration of this MOF would require longer exposure to a 0.1 M sodium nitrate solution, which would result and inevitable lost of material due to its partial dissolution. A potential strategy to mitigate this loss of material could be to increase the concentration of nitrate at the regeneration stage in order to accelerate the reverse anion exchange minimizing the reaction time, consequently reducing the dissolution of the coordination polymers after prolonged periods of time in solution. Finally, once a more effective regeneration strategy is achieved, the ability of SBN to capture oxyanion pollutants via anion exchange will also be explored with other environmentally relevant species including chromate, arsenate, selenate, and pertechnetate.

The biocidal activity of SLUG-39 and SLUG-40 will be evaluated against other ubiquitous bacterial strains that have been problematic in healthcare facilities including *Staphylococcus aureus*, *Pseudomonas aureginosa*, and *Shewanella*. In addition, the biocidal activity of these Zn-based coordination polymers will also be investigated against other microorganisms such as fungal species that have been persistent and cause opportunistic infections as in the case of *Candida albicans*. Once a complete evaluation of the biocidal effects of Zn-based coordination has been established, the activity of other MOFs containing bioactive metals can be evaluated. In particular, the assessment of Cu-based MOFs would be of interest as this metal is known to exhibit both bactericidal and fungicidal properties and has limited antibacterial studies compared to that of Ag-based MOFs. Moreover, the gradual release of copper ions around the cell wall of bacteria could prove to be effective as the solubility of CuCl [K_{sp}= 1.72 x 10^{-7}] is much greater than that of AgCl [K_{sp}(AgCl) = 1.77 x 10^{-11}]. In addition to evaluating other bioactive metals, the choice of ligand can also be tailored for an enhanced antibacterial activity. A potential functionality that could increase the bactericidal activity of a MOF is the presence of quaternary amine groups in the organic linker. The quaternary amine groups are known to induce anchoring to the negatively charged cell wall of bacteria, which would enable a more localized release of metal ions that could disrupt the cation homeostasis. Another future direction in the biocidal evaluation of MOFs could be their incorporation into various polymer matrices in order to slow their degradation and hence their release of ions. The formation of a polymer/MOF composite could pave the way into their evaluation for biofilm inhibition due to the increased in robustness, which could be integrated into the fabrication of new antibacterial coatings. Their potential inhibition of biofilm formation would represent a significant advancement in the healthcare industry, as biofilm are responsible for adhesion of bacteria to surfaces and play a significant role in the transmission of antibiotic-resistant infections.

Appendix

Appendix A. Hydrothermal Synthesis

sample	compound	ratio(n)	F.W.(g/mol)	wt. Used(g)	actual ratio	T ©C	time(days)
Slug-21							
IC001	AgNO3	1.00	169.87	0.25	1.060575734	150	5
	EDSA	1.00	190.18	0.27	1.023098118		
	4,4-Bipy	1.00	156.2	0.22	1.014985915		
	H2O	400.00	18.016	10	400		
Slug-21							
IC002	AgNO3	1.00	169.87	0.25	1.060575734	150	5
	EDSA	1.00	190.18	0.27	1.023098118		
	4,4-Bipy	1.00	156.2	0.22	1.014985915		
	H2O	400.00	18.016	10	400		
Slug-26							
IC003	Cu(NO3)2	1.00	232.59	0.646	1.000759792	150	5
	EDSNa2	3.25	234.16	2.095	3.223737615		
	CTAB	0.03	364.45	0.03	0.029660036		
	H2O	160.00	18.016	7.981	159.62		
Slug-26							
IC004	Cu(NO3)2	1.00	232.59	0.647	1.002308956	150	5
	EDSNa2	3.25	234.16	2.103	3.236047831		
	CTAB	0.03	364.45	0.029	0.028671368		
	H2O	160.00	18.016	7.912	158.24		
Slug-26							
IC005	Cu(NO3)2	1.00	232.59	0.644	0.997661464	150	5
	EDSNa2	3.25	234.16	2.113	3.2514356		
	CTAB	0.03	364.45	0.029	0.028671368		
	H2O	160.00	18.016	7.905	158.1		
Slug-22							
IC006	Cu(ac)	1.00	199.65	0.28	1.010664663	175	4
	EDSA	1.13	190.18	0.302	1.144354191		
	4,4-Bipy	1.00	156.2	0.214	0.987304481		
	H2O	400.00	18.016	9.992	399.68		
Slug-22							
IC007	Cu(ac)	1.00	199.65	0.28	1.010664663	175	4
	EDSA	1.13	190.18	0.302	1.144354191		
	4,4-Bipy	1.00	156.2	0.214	0.987304481		
	H2O	400.00	18.016	9.992	399.68		
Slug-35							
IC008	Co(NO3)2	0.50	291.03	0.1611	0.498638903	150	3
	Zn(NO3)2	0.50	297.48	0.1659	0.502362243		
	EDSNa2	1.00	234.16	0.2618	1.007129484		
	4,4-Bipy	1.00	156.2	0.1734	0.999991805		
	H2O	400.00	18.016	7.95	397.5		
Slug-35							

IC009	Co(NO3)2	0.50	291.03	0.1708	0.528662475	150	3
	Zn(NO3)2	0.50	297.48	0.173	0.523861772		
	EDSNa2	1.00	234.16	0.2603	1.001359071		
	4,4-Bipy	1.00	156.2	0.1736	1.001145198		
	H2O	400.00	18.016	7.93	396.5		
Slug-21							
IC010	AgNO3	1.00	169.87	0.2402	1.019001166	150	5
	EDSA	1.00	190.18	0.2684	1.017035314		
	4,4-Bipy	1.00	156.2	2183	10071.42843		
	H2O	400.00	18.016	9.703	388.12		
Slug-21							
IC011	AgNO3	1.00	169.87	0.2372	1.006274257	150	5
	EDSA	1.00	190.18	0.2689	1.01892994		
	4,4-Bipy	1.00	156.2	0.221	1.019599488		
	H2O	400.00	18.016	9.661	386.44		
Slug-26							
IC012	Cu(NO3)2	1.00	232.59	0.6476	1.003238454	150	5
	EDSNa2	3.25	234.16	2.107	3.242202938		
	CTAB	0.03	364.45	0.0269	0.026595165		
	H2O	160.00	18.016	7.9425	158.85		
Slug-21							
IC013	AgNO3	1.00	169.87	0.2388	1.013061941	150	5
	EDSA	1.00	190.18	0.2673	1.012867136		
	4,4-Bipy	1.00	156.2	0.2172	1.002067913		
	H2O	400.00	18.016	9.983	399.32		
Slug-21							
IC014	AgNO3	1.00	169.87	0.2396	1.016455784	150	5
	EDSA	1.00	190.18	0.2695	1.021203491		
	4,4-Bipy	1.00	156.2	0.2167	0.999761127		
	H2O	400.00	18.016	9.503	380.12		
Slug-26							
IC015	Cu(NO3)2	1.00	232.59	0.6489	1.005252367	150	5
	EDSNa2	3.25	234.16	2.1108	3.24805029		
	CTAB	0.03	364.45	0.0306	0.030253236		
	H2O	160.00	18.016	7.4608	149.216		
Slug-21							
IC016	AgNO3	1.00	169.87	0.2356	0.999486572	150	5
	EDSA	1.00	190.18	0.2617	0.991647324		
	4,4-Bipy	1.00	156.2	0.2151	0.992379411		
	H2O	400.00	18.016	9.823	392.92		
Slug-21							
IC017	AgNO3	1.00	169.87	0.2404	1.019849626	150	5
	EDSA	1.00	190.18	0.2629	0.996194426		
	4,4-Bipy	1.00	156.2	0.2174	1.002990627		
	H2O	400.00	18.016	9.8835	395.34		
Slug-21							
IC018	AgNO3	1.00	169.87	0.2404	1.019849626	150	5
	EDSA	1.00	190.18	0.2629	0.996194426		

	4,4-Bipy	1.00	156.2	0.2174	1.002990627		
	H2O	400.00	18.016	9.8835	395.34		
Slug-21							
IC019	AgNO3	1.00	169.87	0.2337	0.991426197	150	5
	EDSA	1.00	190.18	0.2185	0.827951625		
	Na2CO3	1.00	105.99	1.0195	6.931715067		
	H2O	400.00	18.016	9.96	398.4		
Slug-21							
IC020	AgNO3	1.00	169.87	0.2337	0.991426197	150	5
	EDSA	1.00	190.18	0.2185	0.827951625		
	NaHCO3	1.00	84	1.005	8.621942857		
	H2O	400.00	18.016	9.96	398.4		
Slug-21							
IC021	AgNO3	1.00	169.87	0.2345	0.994820039	150	5
	EDSA	1.00	190.18	0.2653	1.005288632		
	4,4-Bipy	1.00	156.2	0.225	1.038053777		
	H2O	400.00	18.016	9.853	394.12		
Slug-21							
IC022	AgNO3	1.00	169.87	0.2349	0.99651696	150	5
	EDSA	1.00	190.18	0.2631	0.996952277		
	4,4-Bipy	1.00	156.2	0.224	1.033440205		
	H2O	400.00	18.016	9.953	398.12		
Slug-21							
IC023	AgNO3	1.00	169.87	0.2412	1.023243469	150	5
	EDSA	1.00	190.18	0.2625	0.994678725		
	4,4-Bipy	1.00	156.2	0.2172	1.002067913		
	H2O	400.00	18.016	9.7748	390.992		
Slug-21							
IC024	AgNO3	1.00	169.87	0.2488	1.055484971	150	5
	EDSA	1.00	190.18	0.2183	0.827193774		
	4,4-Bipy	1.00	156.2	0.2654	1.2244421		
	H2O	400.00	18.016	9.8514	394.056		
Slug-21							
IC025	AgNO3	1.00	169.87	0.239	1.013910402	150	5
	EDSA	1.00	190.18	0.2683	1.016656389		
	4,4-Bipy	1.00	156.2	0.218	1.005758771		
	H2O	400.00	18.016	10.0056	400.224		
Slug-21							
IC026	AgNO3	1.00	169.87	0.2381	1.010092329	150	5
	EDSA	1.00	190.18	0.217	0.822267746		
	4,4-Bipy	1.00	156.2	0.269	1.24105096		
	H2O	400.00	18.016	9.9762	399.048		
Slug-21							
IC027	AgNO3	1.00	169.87	0.2373	1.006698487	150	5
	EDSA	1.00	190.18	0.2173	0.823404522		
	4,4-Bipy	1.00	156.2	0.2662	1.228132958		
	H2O	400.00	18.016	9.94069	397.6276		
Slug-21							

IC028	AgNO3	1.00	169.87	0.2392	1.014758863	150	5
	EDSA	1.00	190.18	0.2187	0.828709475		
	4,4-Bipy	1.00	156.2	2638	12170.60384		
	H2O	400.00	18.016	9.9566	398.264		
Slug-21							
IC029	AgNO3	1.00	169.87	0.2368	1.004577336	150	5
	EDSA	1.00	190.18	0.2625	0.994678725		
	4,4-Bipy	1.00	156.2	0.2213	1.02098356		
	H2O	400.00	18.016	9.9405	397.62		
Ag-bipy-NO3							
IC030	AgNO3	1.00	169.87	0.11	0.933306646	150	1
	4,4-Bipy	1.00	156.2	0.111	1.02421306	110	4hrs
	H2O	800.00	18.016	9.982	798.56	90	20hrs
Ag-bipy-NO3							
IC031	AgNO3	1.00	169.87	0.102	0.865429799	150	1
	4,4-Bipy	1.00	156.2	0.1	0.922714469	110	4hrs
	H2O	800.00	18.016	10.026	802.08	90	20hrs
Ag-bipy-NO3							
IC032	AgNO3	1.00	169.87	0.2337	1.982852393	150	5
	4,4-Bipy	1.00	156.2	0.2186	2.017053828	slow cool	
	H2O	800.00	18.016	9.9156	793.248		
Ag-bipy-NO3							
IC033	AgNO3	1.00	169.87	0.1019	0.864581339	140	6
	4,4-Bipy	1.00	156.2	0.1039	0.958700333	110	
	H2O	800.00	18.016	9.896	791.68	90	
Ag-bipy-NO3							
IC034	AgNO3	1.00	169.87	0.1017	0.862884417	140	6
	4,4-Bipy	1.00	156.2	0.1037	0.956854904	110	
	H2O	800.00	18.016	9.8864	790.912	90	
Ag-bipy-NO3							
IC035	AgNO3	1.00	169.87	0.1017	0.862884417	140	5
	4,4-Bipy	1.00	156.2	0.1037	0.956854904	110	
	H2O	800.00	18.016	9.8864	790.912	90	
Ag-bipy-NO3							
IC036	AgNO3	1.00	169.87	0.1045	0.886641314	140	5
	4,4-Bipy	1.00	156.2	0.1034	0.954086761	110	
	H2O	800.00	18.016	9.903	792.24	90	
Ag-bipy-NO3							
IC037	AgNO3	1.00	169.87	0.0511	0.86712672	140	5
	4,4-Bipy	1.00	156.2	0.0507	0.935632471	110	
	H2O	1600.00	18.016	5.0347	805.552	90	
Ag-bipy-NO3							
IC038	AgNO3	1.00	169.87	0.1071	0.908701289	140	3
	4,4-Bipy	1.00	156.2	0.1027	0.947627759	110	
	H2O	800.00	18.016	9.8369	786.952	90	
ZBP							
IC074	Zn(NO3)2	1.00	297.48	0.2628	0.636628318	150	1
	NaClO4	1.00	140.46	0.2639	1.353957682		

	4,4-Bipy	1.00	156.2	0.2168	1.000222484		
	H2O	400.00	18.016	10	400		
ZABP							
IC075	Zn(OAc)2	1.00	219.5	0.2546	0.835876738	150	1
	NaClO4	1.00	140.46	0.2639	1.353957682		
	4,4-Bipy	1.00	156.2	0.2168	1.000222484		
	H2O	400.00	18.016	9.9405	397.62		
Mg-MOF							
IC137	Mg(Oac)2	1.00	214.5	0.217	0.729039068	150	1
	NaClO4	1.00	140.46	0.189	0.969677915		
	4,4-Bipy	1.00	156.2	0.223	1.028826633		
	H2O	400.00	18.016	10	400		
Mg-MOF							
IC138	Zn(OAc)2	1.00	219.5	0.217	0.712432255	150	1
	4,4-Bipy	1.00	156.2	0.234	1.079575928		
	H2O	400.00	18.016	9.9405	397.62		
ZBP							
IC140	Zn(NO3)2	1.00	297.48	0.425	1.029554928	150	5
	NaClO4	1.00	140.46	0.21	1.077419906		
	4,4-Bipy	1.00	156.2	0.225	1.038053777		
	H2O	400.00	18.016	9.98	399.2		
ZABP							
IC141	Zn(OAc)2	1.00	219.5	0.316	1.037458952	150	5
	NaClO4	1.00	140.46	0.224	1.1492479		
	4,4-Bipy	1.00	156.2	0.233	1.074962356		
	H2O	400.00	18.016	9.924	396.96		
Mg-MOF							
IC142	Mg(Oac)2	1.00	214.5	0.301	1.011247739	150	5
	NaClO4	1.00	140.46	0.233	1.195423039		
	4,4-Bipy	1.00	156.2	0.227	1.047280922		
	H2O	400.00	18.016	9.939	397.56		
Mg-MOF							
IC143	Mg(OH)2	1.00	58.32	0.122	1.50751166	150	5
	EDSNa2	1.00	234.16	0.329	1.012515203		
	4,4-Bipy	1.00	156.2	0.224	1.033440205		
	H2O	400.00	18.016	9.923	396.92		
Mg-MOF							
IC144	MgCl2	1.00	203.3	0.309	1.095316085	150	5
	4,4-Bipy	1.00	156.2	0.223	1.028826633		
	H2O	400.00	18.016	9.81	392.4		
Mg-MOF							
IC145	Mg(Oac)2	1.00	214.5	0.321	1.07844028	150	5
	EDSNa2	1.00	234.16	0.354	1.089454049		
	4,4-Bipy	1.00	156.2	0.224	1.033440205		
	H2O	400.00	18.016	9.713	388.52		
Mg-MOF							
IC146	Mg(Oac)2	1.00	214.5	0.302	1.014607366	150	5
	NaBO2	1.00	65.8	0.101	1.106149544		

	4,4-Bipy	1.00	156.2	0.221	1.019599488		
	H2O	400.00	18.016	9.766	390.64		
Mg-MOF							
IC147	Mg(Oac)2	1.00	214.5	0.295	0.991089977	150	1
	NaBF4	2.00	109.8	0.163	1.06980255		
	4,4-Bipy	1.00	156.2	0.224	1.033440205		
	H2O	400.00	18.016	9.964	398.56		
ZBB							
IC148	Zn(NO3)2	1.00	297.48	0.429	1.039244857	150	1
	NaBF4	2.00	140.46	0.157	0.805499644		
	4,4-Bipy	1.00	156.2	0.227	1.047280922		
	H2O	400.00	18.016	9.962	398.48		
ZABB							
IC149	Zn(OAc)2	1.00	219.5	0.313	1.027609658	150	1
	NaBF4	2.00	140.46	0.155	0.795238502		
	4,4-Bipy	1.00	156.2	0.223	1.028826633		
	H2O	400.00	18.016	9.966	398.64		
ZBP							
IC150	Zn(NO3)2	1.00	297.48	0.414	1.002907624	150	1
	NaClO4	1.00	140.46	0.415	2.129186957		
	4,4-Bipy	1.00	156.2	0.223	1.028826633		
	H2O	400.00	18.016	9.977	399.08		
ZABP							
IC151	Zn(OAc)2	1.00	219.5	0.315	1.034175854	150	1
	NaClO4	1.00	140.46	0.424	2.175362096		
	4,4-Bipy	1.00	156.2	0.229	1.056508067		
	H2O	400.00	18.016	10	400		
Mg-MOF							
IC152	Mg(Oac)2	1.00	214.5	0.303	1.017966993	150	1
	NaClO4	1.00	140.46	0.413	2.118925815		
	4,4-Bipy	1.00	156.2	0.238	1.098030218		
	H2O	400.00	18.016	9.971	398.84		
Mg-MOF							
IC153	Mg(Oac)2	1.00	214.5	0.314	1.05492289	150	1
	NaBF4	2.00	109.8	0.158	1.036986521		
	4,4-Bipy	1.00	156.2	0.234	1.079575928		
	H2O	400.00	18.016	9.93	397.2		
ZBB							
IC154	Zn(NO3)2	1.00	297.48	0.427	1.034399892	150	1
	NaBF4	2.00	140.46	0.169	0.867066496		
	4,4-Bipy	1.00	156.2	0.223	1.028826633		
	H2O	400.00	18.016	9.891	395.64		
ZABB							
IC155	Zn(OAc)2	1.00	219.5	0.309	1.014477267	150	1
	NaBF4	2.00	140.46	0.155	0.795238502		
	4,4-Bipy	1.00	156.2	0.24	1.107257362		
	H2O	400.00	18.016	9.92	396.8		
SLUG-17							

IC162	$Er(NO_3)_3$	1.00	443.35	0.309	1.004523559	125	2
	UREA	17.00	60.06	0.7084	16.99971282		
	H_2O	800.00	18.016	9.75	780		
SLUG-17							
IC163	$Er(NO_3)_3$	1.00	443.35	0.245	0.995583625	125	2
	UREA	17.00	60.06	0.562	16.85812854		
	H_2O	1000.00	18.016	9.813	981.3		
SLUG-17							
IC164	$Er(NO_3)_3$	1.00	443.35	0.205	0.833039359	125	2
	UREA	17.00	60.06	0.476	14.27841492		
	H_2O	1000.00	18.016	9.842	984.2		
SLUG-17							
IC165	$Er(NO_3)_3$	1.00	443.35	0.305	1.487280027	125	2
	UREA	17.00	60.06	0.702	25.26919481		
	H_2O	1200.00	18.016	9.75	1170		
SLUG-18							
IC166	$Er(NO_3)_3$	1.00	443.35	0.206	0.669682373	150	2
	UREA	17.00	60.06	0.562	13.48650283		
	H_2O	800.00	18.016	9.902	792.16		
SLUG-18							
IC167	$Er(NO_3)_3$	1.00	443.35	0.246	0.999647231	150	2
	UREA	17.00	60.06	0.477	14.30841159		
	H_2O	1000.00	18.016	9.853	985.3		
SLUG-18							
IC168	$Er(NO_3)_3$	1.00	443.35	0.204	0.828975753	150	2
	UREA	17.00	60.06	0.472	14.15842824		
	H_2O	1000.00	18.016	9.9	990		
SLUG-18							
IC169	$Er(NO_3)_3$	1.00	443.35	0.205	0.999647231	150	2
	UREA	17.00	60.06	0.569	20.48172627		
	H_2O	1200.00	18.016	9.882	1185.84		
IC171	$Er(NO_3)_3$	1.00	443.35	0.2085	1.016714379	125	2
	THIOUREA	17.00	76.12	0.6015	17.08348502		
	H_2O	1200.00	18.016	9.88	1185.6		
IC172	$Er(NO_3)_3$	1.00	443.35	0.246	0.999647231	125	2
	THIOUREA	17.00	76.12	0.7161	16.94857803		
	H_2O	1000.00	18.016	9.92	992		
IC173	$Er(NO_3)_3$	1.00	443.35	0.205	0.999647231	150	2
	THIOUREA	17.00	76.12	0.5971	16.95851855		
	H_2O	1200.00	18.016	9.94	1192.8		
IC174	$Er(NO_3)_3$	1.00	443.35	0.2509	1.019558904	150	2

	THIOUREA	17.00	76.12	0.7185	17.00538098		
	H2O	1000.00	18.016	9.96	996		
SLUG-18							
IC175	Er(NO3)3	1.00	443.35	0.21	0.853357393	150	2
	UREA	17.00	60.06	0.559	16.76813853		
	H2O	1000.00	18.016	9.934	993.4		
SLUG-18							
IC176	Er(NO3)3	1.00	443.35	0.213	1.038657855	150	2
	UREA	17.00	60.06	0.474	17.06210589		
	H2O	1200.00	18.016	9.909	1189.08		
IC177	Er(NO3)3	1.00	443.35	0.204	0.994770903	125	2
	THIOUREA	17.00	76.12	0.61	17.32489753		
	H2O	1200.00	18.016	9.745	1169.4		
IC178	Er(NO3)3	1.00	443.35	0.203	0.824912146	125	2
	THIOUREA	17.00	76.12	0.707	16.73320021		
	H2O	1000.00	18.016	9.706	970.6		
IC179	Er(NO3)3	1.00	443.35	0.206	1.004523559	150	2
	THIOUREA	17.00	76.12	0.594	16.87047399		
	H2O	1200.00	18.016	9.838	1180.56		
IC180	Er(NO3)3	1.00	443.35	0.206	0.837102966	150	2
	THIOUREA	17.00	76.12	0.713	16.87520757		
	H2O	1000.00	18.016	9.877	987.7		

Table A1. Acquisition parameters for solid-state NMR experiments[a]

Nuclei	^{13}C	^{15}N	^{109}Ag[b]
Larmor frequency / MHz	100.6	40.5	18.6
Number of scans	32-64	768-1280	1280-10240
MAS / kHz	12	6	3
^1H rf field during pulse / μs	83	83	70
CP contact time / ms	2	5	20
^1H rf field during CP contact / kHz	60	60	37
X rf field during CP contact / kHz	53	42	27
^1H rf field during decoupling / kHz	83	83	70

[a] Recycle delays were 180, 30, 30, 80, 70 s for SBN, 10 min SBN exchange, 25 min SBN exchange, SBP, regenerated SBN, respectively and correspond to 1.3 × T_1; [b] ^{109}Ag CP MAS NMR experiments were set up on $AgSO_3CH_3$ according to a literature procedure.[1]